PLASMA–MATERIAL INTERACTION AND ELECTRODE DEGRADATION IN HIGH VOLTAGE IGNITION DISCHARGES

DISSERTATION

zur Erlangung des Grades
des Doktors der Ingenieurwissenschaften
der Naturwissenschaftlich-Technischen Fakultät III
Chemie, Pharmazie, Bio- und Werkstoffwissenschaften
der Universität des Saarlandes

von

NICOLAS JEANVOINE

Saarbrücken

2009

Tag des Kolloquiums:

Dekan:	Prof. Dr.-Ing. Stefan Diebels
Berichterstatter:	Prof. Dr.-Ing. Frank Mücklich
	Prof. Dr.-Ing. Frank Berger

Plasma seems to have the kinds of properties one would like for life. It's somewhat like liquid water - unpredictable and thus able to behave in an enormously complex fashion. It could probably carry as much information as DNA does. It has at least the potential for organizing itself in interesting ways.

Freeman John Dyson

Contents

Acknowledgments

I would like to express my gratitude to all the persons who supported my work and encouraged me during this Ph.D. thesis:

- Prof. Dr. Frank Mücklich (Saarland University) for the opportunity to work under his supervision in a very interesting research field, his scientific support and personal advice which greatly contributed to the completion of this work;
- Prof. Dr. Frank Berger (TU Ilmenau) for the acceptance of the co-refereeing of this thesis and the interesting discussions about electric arcs;
- All the industrial and academic partners of the project "Elektroerosion" Nr. 03X3500H supported by the German Federal Ministry of Education and Research (BMBF) for the efficient collaboration and the interesting discussions: Dr. Jürgen Oberle, Simone Baus, Dr. Jochen Rager (Robert Bosch GmbH), Dr. Andreas Krätzschmar (Siemens AG), Prof. Dr. David Lupton, Dr. Tanja Eckardt (W.C. Heraeus GmbH), Dr. Bernd Kempf (Umicore AG & Co. KG), Prof. Dr. Frank Berger, Meik Sacher, Dr. Diego Gonzalez (TU Ilmenau), Matthias Ommer, Dr. Ulrich Klotz, Dr. Jörg Fischer-Bühner (Forschungsinstitut für Edelmetalle und Metallchemie), Dr. Thomas Lampke (TU Chemnitz);
- Dr. Flavio Soldera for his continuous support, his constructive suggestions, and for the proofreading and important comments about this thesis;
- Dr. Christian Holzapfel for his help and useful suggestions concerning the microstructure analysis using FIB, SEM and TEM;
- Meik Sacher (TU Ilmenau) for the numerous and valuable discussions about cathode spots and his help with the simulation;
- My colleagues of the research group "Elektroerosion" for their continuous support and fruitful discussions: Christian Selzner, Kim Trinh, Sebastian Suarez, and Dimitrij Ladutkin;
- The students that I supervised and who contributed to different aspects of this work: Laure Thomas (EEIGM), Ghizlane Bamoulid (EEIGM), David McIntosh (Oregon University), Robert Jonsson (EEIGM), Hyo Jeong Moon (AMASE), Aurélien Riquier (Mines de Douai), and Lluís Yedra i Cardona (EEIGM);

- Paula Souza for the proofreading and accurate reviewing of the manuscript;
- All my colleagues and friends of the chair of Functional Materials for the friendly working atmosphere and their support through all these years;
- The German Academic Exchange Program (DAAD) for the scholarship granted to me during the period October 2004 - July 2005;
- My parents Marie-Claude and Alain, my brother Thomas, “mi vida” Mariela, my family, and my friends for their unconditional love, encouragement and faith in me during all these years.

Abstract

Erosion of material caused by electrical discharges takes place in many technical applications. Particularly, in spark plugs, the durability is mainly determined by the electrode erosion caused by ignition discharges. A better understanding of the wear mechanisms will help in developing new electrode materials with enhanced resistance against spark erosion.

In this work, different aspects of the complex interaction between the plasma of the ignition discharge and the electrode are investigated based on experimental observations and simulations.

The discharge mode behavior is quantitatively analyzed with regard to the arc and glow phase fractions for different electrode materials and conditions of pressure and gas. The influence of these parameters on the discharge is discussed. This work especially focuses on the formation of microscopic erosion craters on the electrode surface. Their morphology and microstructure are characterized by means of FIB/SEM dual beam techniques. The depth of modifications and the extent of the molten region are determined. To complete these experimental observations, thermal analysis of the crater formation is performed using analytical models and FEM simulations. Characteristic values of time, power density and current involved in the crater formation are estimated. These values are related to the electrical characteristic of the spark, and the effects of the discharge phases on the electrode surface degradation are discussed.

Kurzfassung

Die Erosion von Materialien, die von einer elektrischen Entladung hervorgerufen wird, tritt in zahlreichen technischen Anwendungen auf. Auch die Lebensdauer einer Zündkerze wird durch die von den Zündentladungen verursachte Erosion an Elektrodenmaterialien maßgeblich bestimmt. Ein besseres Verständnis der Verschleißmechanismen ist von großer Bedeutung, um maßgeschneiderte Werkstoffe mit verbessertem Funkenerosionsverhalten zu entwickeln.

In dieser Arbeit werden verschiedene Aspekte der komplexen Wechselwirkung zwischen dem Plasma der Zündentladung und der Elektrode anhand von experimentellen Beobachtungen und Simulationen erforscht.

Das Entladungsverhalten (Bogen- und Glimmanteil) wird für verschiedene Elektrodenwerkstoffe, Gas-, und Druckbedingungen quantitativ untersucht. Die Morphologie und Mikrostruktur von Erosionskratern werden mit Hilfe von FIB/REM Dual-Beam-Techniken charakterisiert. Die mikrostrukturellen Veränderungen des Materials unterhalb der Oberfläche und insbesondere der Schmelzbadgröße werden bestimmt. Zur Ergänzung der experimentellen Beobachtungen, wird eine thermische Analyse der Kraterbildung mittels analytischen Modellen und FEM-Simulationen durchgeführt. Charakteristische Werte des Kraterbildungsprozesses wie z.B. die Wärmezufuhr, der Strom, und die Wechselwirkungsdauer werden bestimmt und in Bezug auf die verschiedenen Phasen der Zündentladung diskutiert.

Symbols and Abbreviations

List of Symbols

a	Spot or crater radius
B	Magnetic field
C_C	Coil capacitance
C_p	Spark plug capacitance
c_p	Specific heat capacity
d	Interelectrode distance
D	Electron tunneling probability at the metal surface
e	Elementary charge
E''	Sputtering bombarding energy
E'	Space charge electric field
E_0	External electric field
E_a, E_g	Arc and glow electrical energies
E_b	Breakdown electric field
E_{br}	Breakdown electrical energy
E_c	Mean arc erosion rate
E_{cond}	Energy lost in conduction
E_e	Energy lost via electron emission
E_i	Ionization energy
E_{ion}	Energy brought by ion bombardment
E_m	Energy lost via heating and melting
E_m	Energy lost via melting
E_s	Surface electric field strength
E_{vap}	Energy lost via vaporization
F_L	Lorentz force
h	Planck constant
i	Discharge current
i_1, i_2	Primary and secondary side currents
i_a, i_g	Arc and glow phase currents
J	Current density
J_0, J_1	Bessel functions of the first kind of order 0 and 1
J_{bde}	Back-diffusing electron current densities
J_e, J_i	Electron and ion current densities
J_T	Thermionic electron current density
J_{TF}	Thermo-field electron current density
k	Thermal conductivity
k_B	Boltzmann constant
L	Simulated region length
L_1, L_2	Primary and secondary side coil inductances
L_m	Latent heat of melting
M	Atomic weight
m_e	Electron mass
m_i	Positive ion mass
m_n	Atomic mass
N	Fermi-Dirac energy distribution function of electrons
n_e, n_i	Electron and ion number densities
p	External pressure
P_{bde}	Heating power density by back-diffusing electrons
P_e	Cooling power density by electron emission (Nottingham effect)
$P_{electrode}$	Power density dissipated in the bulk electrode
P_i	Heating power density by ion bombardment

p_{ion}	Ion pressure
P_j	Joule heating power density
P_m	Critical melting power density
$P_{r,p}$	Heating power density by radiation from the plasma
$P_{r,s}$	Cooling power density by radiation from the surface
P_{rn}	Heating power density by returning atoms
p_v	Equilibrium vapor pressure
P_{vap}	Cooling power density by vaporization of atoms
Q	Discharge capacitance
Q_0	Pulse energy
q_0	Pulse heat flux
$\dot{q}_{SL}$	Melting power per unit of volume
R	Avalanche head radius
R_1, R_2	primary and secondary side coil resistances
Re	Reynolds number
r_m	Molten pool radius
R_P	spark plug resistance
R_{PC}	resistance of the high voltage cable and the plug connector
s	Electronic current fraction
T	Temperature
T_0	Initial temperature
t_0	Heat pulse duration
t_a, t_g	Arc and glow phase durations
T_b	Boiling temperature
T_e, T_i	Electron and ion temperatures
T_m	Melting temperature
T_p	Plasma temperature
T_s	Surface temperature
T_{spot}	Cathode spot temperature
U_a	Anode voltage drop
u_a, u_g	Arc and glow phase burning voltage
U_b	Breakdown voltage
U_c	Cathode voltage drop
U_i	Mean energy of bombarding ions
U_s	Surface binding energy
V_{down}	Crater depression volume
V_e	Vaporized eroded volume
V_m	Molten volume
V_{up}	Crater rim volume
W	Electron energy
W_a	Electron energy inside the metal surface
W_{ev}	Heat of vaporization
x	Distance from the cathode
Y	Primary sputter yield
Z_i	Mean ion charge
z_m	Molten pool depth
ϕ	Work function
γ	Cathode second emission coefficient
σ	Stefan-Boltzmann constant
ρ	Density
α	Thermal diffusivity
τ	Discharge time constant
$\varnothing$	Diameter
ϕ'	Modified work function
ε_0	Vacuum permittivity
μ_0	Vacuum permeability
σ_{el}	Electrical conductivity
ΔH_{mix}	Heat of mixing
ΔT_m	Melting temperature interval
α_i	Towsend's ionization coefficient
τ_L	Lorentz shear stress
γ_l	Surface tension

τ_M	Marangoni shear stress
Γ_n	Flux of vaporized atoms

List of Abbreviations

CCD	Charge Coupled Device
DC	Direct Current
EBSD	Electron Backscatter Diffraction
EDM	Electrical Discharge Machining
EDX	Energy Dispersive X-ray Spectroscopy
EG	Electrode Gap
fcc	face centered cubic
FDA	Frequency Domain Analysis
FEM	Finite Element Method
FIB	Focused Ion Beam
IBID	Ion Beam Induced Deposition
ipf	inverse pole figure
iq	image quality
LTE	Local Thermodynamic Equilibrium
MeO	Metal Oxide
ML	Multilayer
PVD	Physical Vapor Deposition
PZT	Lead Zirconate Titanate
rms	root-mean-square
SE	Secondary Electrons
SEM	Scanning Electron Microscope
STEM	Scanning Transmission Electron Microscope
TEM	Transmission Electron Microscope
TF	Thermo-Field
WLI	White Light Interferometer

CHAPTER 1

Introduction

Self-sustaining electrical discharges take place in many technical applications. The understanding of the interaction between the plasma of the discharge and the electrode has always been of special interest, motivated by the desire to develop plasma systems with better performances. A common phenomenon occurring in these systems over time is the erosion of the electrode caused by the discharges, also called electro- or plasma-erosion. In some cases, electrode erosion is desired and a better understanding of the wear mechanisms would help in reaching better performances. One can take as examples the electrical discharge machining (EDM) process where an electric arc is used as a cutting tool for machining hard metals, the arc welding process where the arc is used to melt the metals and join two work pieces, or vacuum arc deposition techniques such as cathodic arc deposition where an electric arc is used to vaporize material from a cathode target.

In many other cases, however, electrode erosion is a major problem limiting the performances and lifetime of devices and restraining the choice of material. In high intensity discharge (HID) lamps, the electric arc can cause strong erosion of the tungsten electrodes and deposition of the electrode material on the lamp walls (blackening) with catastrophic consequences for lamp efficacy. In switching devices, from small relays and switches to large circuit breakers, the presence of an arc allows a smooth transition from the circuit current to zero current and thus limits overvoltages. However, this arc can lead to the erosion of the contact material, welding of the contacts and irreversibly critical changes of the contact surface.

In spark plugs, the high voltage creates an electrical discharge or spark between the spark plug electrodes, which ignites the compressed air-fuel mixture. The consequence of these discharges is the erosion of the electrodes, also called spark erosion, which leads to widening of the electrode gap and limits the lifetime of the spark plug. Nowadays, nickel-based and platinum electrodes allow reaching a service life of 60 000 km and 100 000 km, respectively. A better understanding of the wear mechanisms will help in developing new electrode materials with still enhanced resistance against spark erosion.

This work aims to provide new insight into the complex plasma-electrode interaction processes in the particular case of ignition discharges, with the final objective to better describe electrode wear mechanisms. Since anode effects are believed to be less critical with regard to erosion, this work will exclusively focus on cathode effects. The investigation of parameters influencing the discharge behavior and the identification of the phases creating surface modifications are the main focus of this study. For this purpose, a large part of the work will be dedicated to the experimental characterization and the simulation of crater formation caused by the impact of single discharges on the electrode surface.

In Chapter 2, background information about the physics of the ignition discharge and the cathode processes is given. The energy balance and physical model used later for the thermal analysis of crater formation are presented, as well as some spark erosion mechanisms.

Chapter 3 presents the experimental set-up used for the generation and analysis of ignition discharges and the different characterization techniques employed for the analysis of the sparked electrode surfaces.

In Chapter 4, a method allowing quantitative and statistical analysis of the ignition discharge characteristic is presented. The arc and glow fractions are determined for different electrode materials and conditions of pressure and gas. The results are discussed regarding surface morphology and arc-to-glow transition current.

Chapter 5 focuses on the microstructure characterization of craters caused by single ignition discharges using different FIB/SEM dual beam techniques. Multilayered electrode systems are introduced in order to monitor the extent of the molten zone. Crater morphology and molten volume are investigated for different external pressures and related with phases of the discharge. The mechanisms of crater formation and the displacement of molten material are also discussed.

In Chapter 6, the thermal effect of the spark on the electrode, leading to crater formation, is first analyzed using analytical models. In order to consider the most important phenomena taking place at the cathode surface, a FEM simulation is developed. The results of the simulation are compared with the experimental data obtained in Chapter 5, permitting to determine relevant parameters of crater formation, such as time of interaction and power density. These results are carefully analyzed and the effects of the ignition discharge phases on the electrode surface degradation are discussed.

Chapter 7 summarizes the most important conclusions drawn from this work and gives some recommendations for further studies in the field of material erosion caused by electrical discharge.

Appendices A to E give some details about the physical model, procedure, and material properties used for the FEM simulation presented in Chapter 6.

CHAPTER 2

Theoretical Background

This chapter presents background information about the ignition discharge and its interaction with electrodes. Section 2.1 provides a survey of the characteristics and physics of the phases of ignition discharge. Cathode processes such as mechanisms permitting the emission of electrons and the cathode spot theory needed to describe arc-cathode interaction are presented in section 2.2. In section 2.3, the energy balance of the ignition discharge is discussed and the basis of the physical model developed for the thermal analysis presented in Chapter 6 is presented. Finally, in section 2.4, a review is made of the mechanisms describing the erosion caused by electrical discharges on electrodes.

2.1 Ignition Discharge Characteristics

The ignition discharge, or ignition spark, is a gas discharge occurring at moderate or high pressures between two static electrodes. Different physical processes occur during the ignition discharge. These processes aim to supply enough charge carriers in order to maintain the discharge. They depend on the electrical characteristics of the ignition circuit as well as on the conditions between the electrodes, and they determine the modes taken by the discharge. A detailed description of the spark ignition process can be found in the works of Maly [1-3], Herden [4] and Albrecht [5, 6].

The ignition discharge is composed of several phases: the breakdown, the arc discharge and the glow discharge (Figure 2.1). During breakdown, a conductive plasma is formed via electron multiplication across the electrode gap. The voltage applied between the electrodes drops from its initial value (several kV) to very low values (~100 V). In this time, the capacitive and inductive components of the spark plug are discharged. Breakdown is followed by the instationary arc discharge, which exists for roughly 1 µs. During this phase, the capacities of the high-voltage cable and the coil discharge their energy. The third and last phase corresponds to the discharge of energy stored in the ignition coil and can last a couple of milliseconds. This phase will always take the form of a glow discharge. At high pressures and currents above 100 mA, however, an arc discharge can be sustained up to some hundreds of microseconds. In an intermediate current range (50-100 mA), rapid transitions occur

between arc and glow regimes. Once the conditions for a self-sustained discharge are no longer fulfilled, the spark breaks away and the voltage is damped to zero [7]. The following section will go into the physics of the breakdown, arc and glow phases composing the ignition discharge investigated in this work.

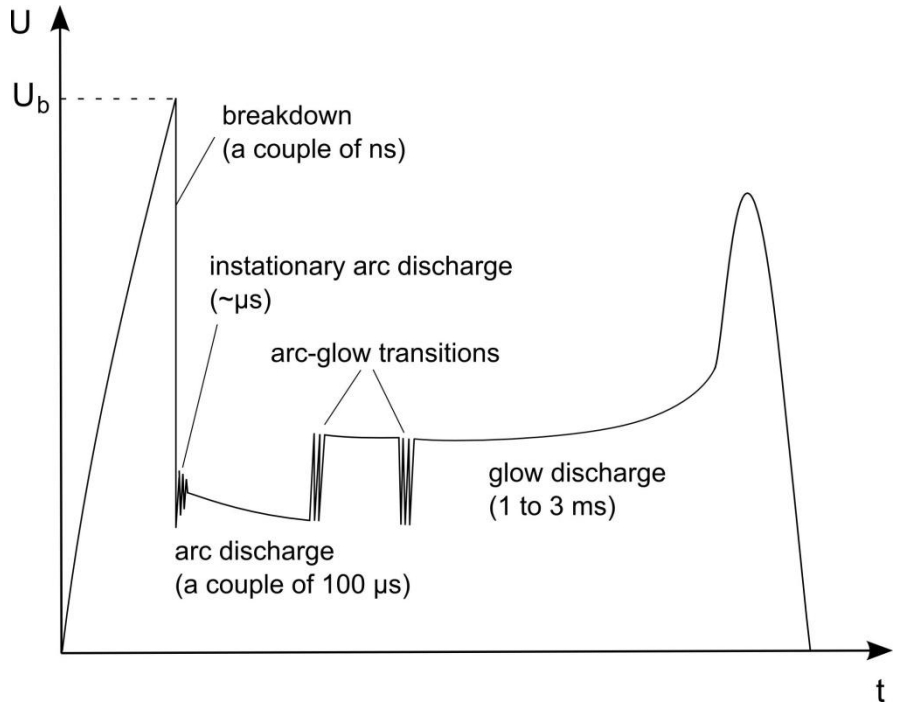

Figure 2.1 Schematic voltage-time characteristic of an ignition discharge. The initial breakdown is followed by a short instationary arc discharge. At high pressures, an arc discharge follows, which finally transforms into a stable glow discharge.

2.1.1 Breakdown Phase

Initially, the gas volume within the electrode gap represents a perfect insulator. The electric breakdown can thus be defined as the transformation of a non-conducting medium into a conductor. The basic primary element of the breakdown process is the electron avalanche. An avalanche begins with a small number of electrons, which appear randomly and accidentally due to ionizing radiations (cosmic rays, UV-light). When a strong enough electric field is applied, the electrons can gain energy and are accelerated towards the anode. The accelerated electrons may ionize the gas molecules by collisions generating additional electrons and ions. The number of electrons and ions increases rapidly. However, as the electrons are absorbed by the anode, additional processes are required to generate enough new starting electrons near or at the cathode. This is accomplished by photons emitted from excited ions, since the impinging electrons not only ionize the gas molecules but excite a multitude of electronic levels as well. As long as the ionizing processes produce less electrons

than required for rendering the discharge self-sustained, this phase is called pre-breakdown. The time of formation of the breakdown depends on gas composition, pressure and field configuration, and may vary from 10^{-9} to several seconds, although it is usually between 10^{-8} and 10^{-4} s [8]. Depending on these parameters, two mechanisms have been developed to explain the formation of breakdown: the Townsend or avalanche multiplication mechanism (section 2.1.1.1) for breakdown at low pressures and the streamer mechanism (section 2.1.1.3) for breakdown in relatively large gaps with atmospheric to high pressures.

2.1.1.1 Townsend Mechanism

The evolution of the Townsend breakdown is best thought as the multiplication of avalanches (Figure 2.2). A starting electron leaving the cathode picks up energy in the applied electric field. Having reached energy somewhat greater than the ionization potential of the gas, the electron ionizes a molecule, thereby losing its energy. The result is the production of two slow electrons. These are again accelerated in the field and ionize two more molecules, thereby producing four electrons, and so forth. The electronic current reaching the anode i is enhanced by a factor $\exp(\alpha_i d)$ in comparison with the current of electrons leaving the cathode i_0:

$$i = i_0 \cdot \exp(\alpha_i d) \tag{2.1}$$

where α_i is the Townsend ionization coefficient and d is the electrode gap. The ionization coefficient α_i corresponds to the number of ionization events produced by an electron in a 1 cm path along the field. In steady state discharge, the total cathode current also equals i, and consists of the electron current i_0 and the current of ions generated in the ionization processes and pulled by the field to the cathode, $i_0[\exp(\alpha_i d)-1]$. As voltage increases further, secondary processes come into play, i.e. the creation of electrons by particles produced as a result of the primary electron impact ionization processes. Secondary processes affect the amplification more strongly if they produce electron emission from the cathode. An emitted electron covers the entire path from cathode to anode and therefore produces more ionization than an electron born halfway. Taking secondary emission into account, the discharge current is given by [9]:

$$i = i_0 \cdot \exp(\alpha_i d)/\{1 - \gamma[\exp(\alpha_i d) - 1]\} \tag{2.2}$$

where γ is the effective secondary emission coefficient for the cathode. The breakdown voltage depends therefore on the cathode material as it is observed experimentally. The secondary emission may be caused by positive ions, photons and metastable atoms produced in the gas as a result of ionization and excitation of gas atoms by electrons. One electron emitted by the cathode produces $\exp(\alpha_i d)$-1 ions which, hitting the cathode, knock out γ electrons each (in the case of electron emission induced by positive ions). The criterion proposed by Townsend [10, 11] for initiating a self-sustaining discharge is given by:

$$\gamma[\exp(\alpha_i d) - 1] \geq 1 \quad \text{or} \quad \alpha_i d \geq \ln(1/\gamma + 1) \tag{2.3}$$

The velocity of the avalanche depends on electric field, gas and pressure, and is generally about 10^7 cm/s [12]. For low $p \cdot d$ values (<200 Torr·cm), the formative time of breakdown corresponds to the travel time of an ion to cross the electrode gap. The breakdown mechanism formulated by Townsend explains a great number of observations and provides a satisfactory quantitative fit for experimental data. It gives a consistent interpretation of Paschen's dependence of the breakdown voltage on $p \cdot d$.

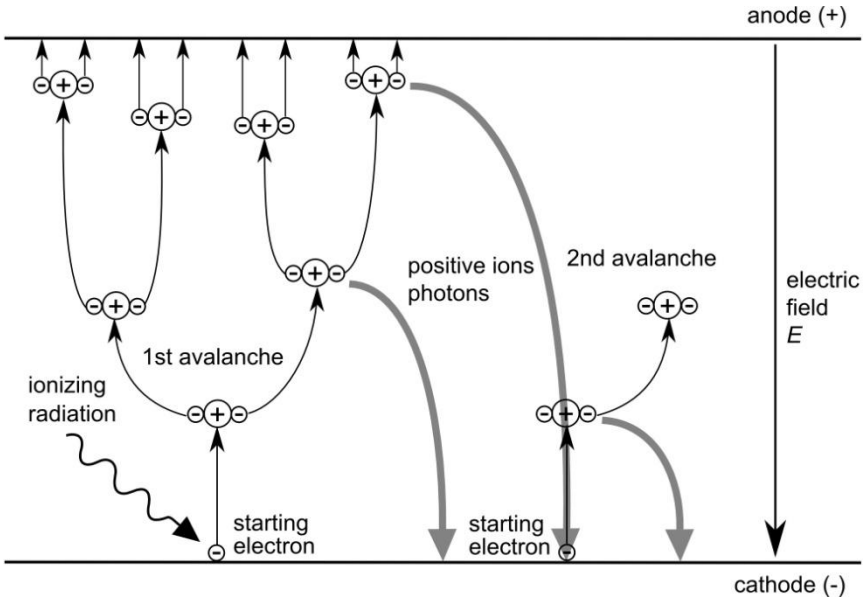

Figure 2.2 Representation of the breakdown mechanism based on the multiplication of avalanches according to Townsend. Electrons accelerated in the electric field ionize molecules, producing electron avalanches. Via secondary emission processes induced by positive ions or photons, new electrons are emitted from the cathode (adapted from [13]).

2.1.1.2 Paschen Law

The breakdown voltage U_b and the corresponding breakdown field E_b depend on the gas, the material of the cathode, the pressure p and the gap width d. At constant temperature, the ionization coefficient can be approximated by:

$$\alpha_i = A \cdot p \cdot exp(-B \cdot p/E_b) \tag{2.4}$$

where A and B are experimentally determined constants of the gas. Substituting equation (2.4) in the Townsend equation (2.3) we obtain that the breakdown voltage depends only on the product of $p \cdot d$:

$$U_b = E_b \cdot d = \frac{B \cdot pd}{\ln\left(\frac{A \cdot pd}{\ln(1 + 1/\gamma)}\right)} \tag{2.5}$$

This equation is known as Paschen's law [14] and permits to calculate U_b in a satisfactory agreement with experiments. It is valid in the $p \cdot d$ range at which the Townsend breakdown mechanism dominates, i.e., at $p \cdot d$ < 200 Torr·cm. The experimental curves $U_b(pd)$ are called Paschen curves and are plotted in Figure 2.3 for various gases. These curves present a minimum. At low $p \cdot d$ values, few gas molecules are available and the possibility of collision is limited. Hence, a very strong field is required to achieve the necessary amplification. High $p \cdot d$ values result from high pressure and/or large electrode gap; a large electrode gap d reduces the electric field, while high pressure p decreases the mean free path of the electrons and lowers their acceleration. In both cases, the ionization coefficient decreases.

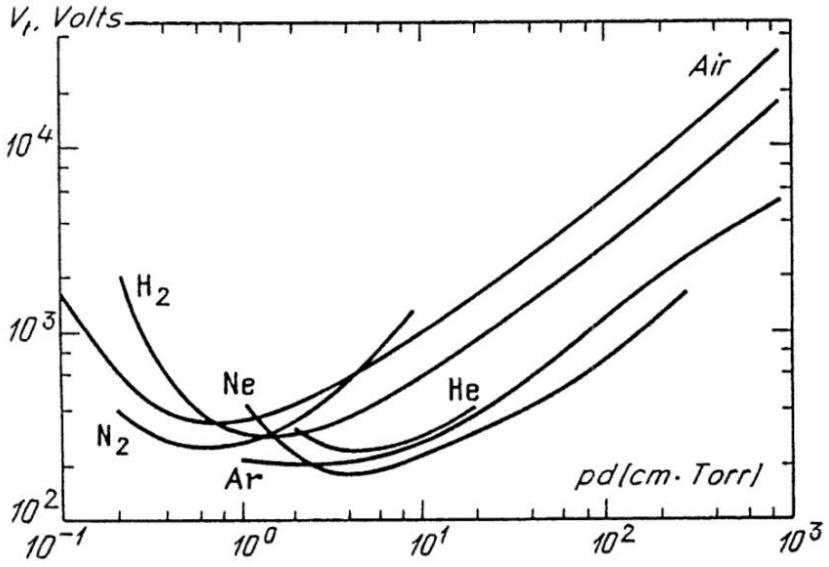

Figure 2.3 Breakdown voltages as a function of $p \cdot d$ (Paschen curves) for various gases over a wide range of $p \cdot d$ values [8].

2.1.1.3 Concept of Streamers

At high $p \cdot d$ and high overvoltages, the breakdown develops much faster than predicted by the multiplication of avalanches described by Townsend. Secondary electron emission due to ion impact can be ignored because the duration of breakdown is insufficient for ions to cross the gap. The current-conducting channel is formed in the time of flight of an electron from the cathode to the anode, or even faster. There is not enough time for the repetition of avalanches through cathode emission. The independence of the breakdown voltage from the cathode material, under these conditions, is evidence against the participation of cathode processes in the breakdown mechanisms. Therefore, the Townsend mechanism is no longer suitable at high $p \cdot d$ and high overvoltages.

Meek, Loeb and Raether [12, 15, 16] developed the fundamentals of a new theory of spark breakdown. This theory is based on the growth of a thin ionized channel (streamer) between the electrodes. The streamer follows the positively charged trail left by the intensive primary avalanche. Electrons of numerous secondary avalanches are pulled into the trail by the field. These avalanches are initiated by new electrons created by photons close to this trail. Photons are emitted by atoms that the primary and secondary avalanches have excited.

In an avalanche with high amplification $\exp(\alpha_i x)$, considerable space charges are generated due to the difference between drift velocities of electrons and ions in the field. Space charges form a sort of dipole: all the electrons are at the head of the avalanche while most of the positive ions remain behind. Because of their larger mass, ions and excited atoms remain practically fixed during the time of flight of the avalanche to the anode. Space charges produce their own electric field E', that adds up vectorially with the external electric field E_0, and distorts it in the vicinity of the avalanche. The fields E' and E_0 in front of the avalanche head combine to give a field E stronger than E_0, while the resulting field inside the avalanche is weaker than E_0 because E' and E_0 are in opposite directions (Figure 2.4). The field also develops a radial component and the diameter of the negative avalanche head grows with the distance due to diffusion processes. The increase of the electric field in front of the avalanche enhances the ionization process and the emission of photons. New starting electrons are created, which generate numerous secondary avalanches.

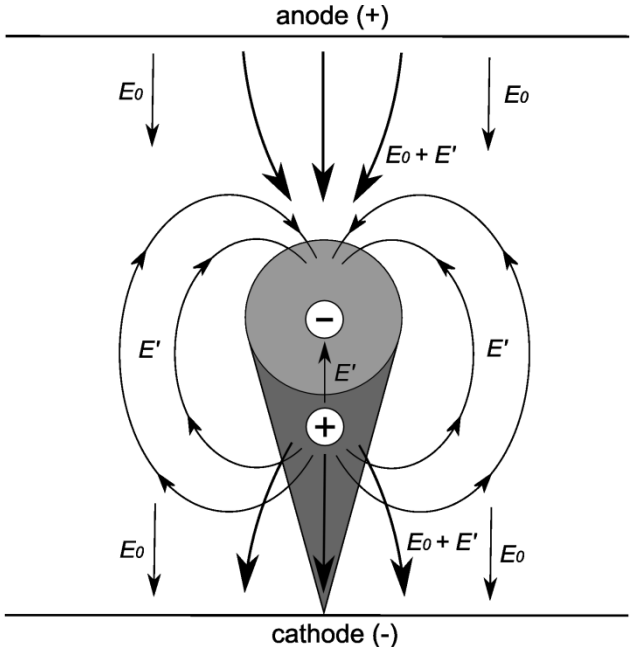

Figure 2.4 Electric fields in a gap containing an avalanche with space charges. For the avalanche to transform into a streamer, the space charge field *E'* must be on the order of the external field E_0.

For an avalanche to transform into a streamer, the space-charged field *E'* must increase to a level on the order of the applied field E_0. This criterion can take the form:

$$E' = eR^2 \exp[\alpha_i(E_0)x] \approx E_0 \tag{2.6}$$

where α is the ionization coefficient, *x* is the distance from the cathode to the anode and *R* is the avalanche head radius. We obtain the Meek breakdown conditions, where *d* is the electrode gap and n_e is the critical number of electrons:

$$\alpha_i(E_0)d \approx 18 - 20, \quad n_e = \exp(\alpha_i d) \sim 10^8\text{-}10^9\ \text{cm}^{-3} \tag{2.7}$$

If gaps are not too wide and overvoltages are not too high, the transformation occurs when the avalanche reaches the anode. The streamer is now initiated at the anode surface, in the region of maximum space charge, and propagates to the cathode. Such streamers are known as cathode-directed or positive (Figure 2.5 left). In wide gaps and at high overvoltages, the number of charges in the primary avalanche increases more rapidly and the avalanche transforms into a streamer before it reaches the anode. In this case, the streamer grows towards both electrodes. However, if the streamer is formed not far from the cathode, it mostly grows towards the anode and the streamer is said to be anode-directed or negative (Figure 2.5 right).

For cathode-directed streamers, electrons produced by photons initiate secondary avalanches, which are pulled into the trail due to the direction of the resulting field.

Secondary-avalanche electrons intermix with primary-avalanche ions and form a quasi-neutral plasma. Secondary-avalanche ions enhance the positive charge at the cathode end of the streamer, attracting the electrons of the next generation of secondary avalanches, and so forth (Figure 2.5 left). For an anode-directed streamer, the electrons drift in the same direction as the front of the plasma streamer. Secondary avalanches are produced in the front of the negatively charged streamer head facing the anode. The front electrons of the head, moving rapidly in the strong total field $E'+E_0$, join the ionic trails of the secondary avalanches and form the streamer (Figure 2.5 right).

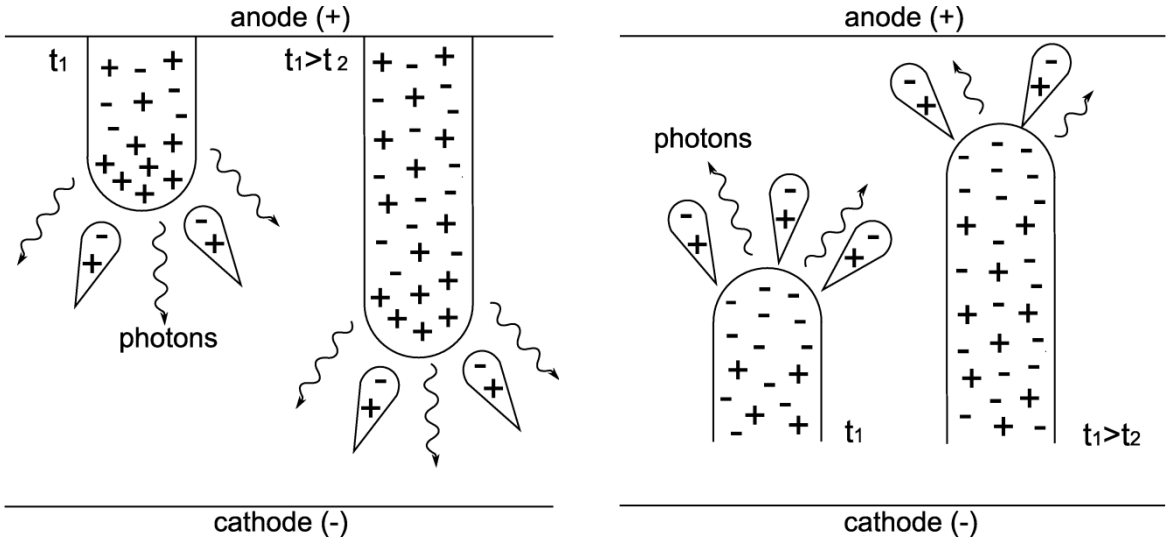

Figure 2.5 Cathode directed streamer (left) and anode directed streamer (right) at two consecutive moments with photoemission and secondary avalanches in front of the streamer head (adapted from [8]).

The growth velocity of the streamer increases as its length and the applied external field increase. The measured velocities are about 10^8 cm/s, while the drift velocities in the external field are about 10^7 cm/s. The streamer channel diameter is comparable with the avalanche head diameter at the stage of maximal expansion, i.e. 10^{-2}-10^{-1} cm [8]. The transition from Townsend to streamer mechanism is smooth and occurs in a range of $p \cdot d$ between 200 and 4000 Torr·cm. In the case of the discharge of an ignition coil with high overvoltages, the ionization coefficient is greater. Therefore, the transition may happen at much lower values of $p \cdot d$ and the streamer mechanism is assumed to dominate in most cases of ignition discharges in spark plugs [13] as well as in our experiments.

2.1.1.4 Breakdown parameters

As soon as the streamer is formed between the electrodes, typically with currents in excess of 10 mA, there is no inherent current-limiting process in the gap. The current rises rapidly to values of more than 100 A until any further increase becomes limited by the impedance of the discharge and the external circuit close to the gap. At this stage, the voltage drops within few nanoseconds to very low values (~100 V). During the breakdown, the charge carrier density in the conductive channel increases to values of ~10^{19} e/cm^{-3} and the plasma can reach temperatures up to 60 000 K. Due to the extremely rapid temperature increase, the pressure in the plasma rises almost instantaneously to several hundreds of bars. The plasma, initially with a diameter <50 µm, expands at supersonic speeds and cools down. Because these processes are very fast, the cathode cannot absorb heat from the plasma via conduction, and therefore remains cold [1]. The end of the breakdown may be taken as the time when the ignition voltage drops below 10 % of its initial value [13]. If a sufficiently high current flow is provided, it may also correspond to the point at which a hot spot is formed on the cathode surface and the discharge turns into an arc.

2.1.2 Breakdown to Arc Transition

The easiest way to initiate an arc is to connect the electrodes to a suitable power supply capable of providing sufficiently high current, bring the electrodes into contact and then separate them. At the point of contact, the temperature may reach the melting point T_m of the metal. Because the contact spot has melted and the electrodes continue to part, a molten metal bridge is formed between them. As the bridge is drawn further it becomes unstable and will rupture and vaporize, releasing metal vapor into the electrode gap. If the temperature of the cathode region is close to the boiling point, thermal ionization will take place in the hot metal gas. The arc will form immediately in the region of the initial molten metal bridge [17].

In spark plugs, however, there is a static gap between the electrodes, and the arc discharge must be preceded by a breakdown. In this case, the power supply and the external circuit must allow the sustainment of the arc discharge. When breakdown occurs and the instationary arc starts, currents are in excess of 100 A and are only limited by the external electrical impedance of the ignition circuit [1].

For discharges in gases at sub-atmospheric pressures and low overvoltages, the breakdown-to-arc transition takes place via one or more transient glow phases. According to Kekez [18], a first diffuse glow discharge forms and tends to expand to cover the whole

electrode surface. Then, the glow contracts and a transition to a second filamentary glow occurs, leading to the formation of the cathode spot. The voltage collapse begins with the second filamentary phase. Chalmers reported similar observations of the formation of a high current transient glow discharge in nitrogen at low overvoltages. In this case, the condition for the transition from a transient glow to an arc is that a certain quantity of energy is dissipated in the gap during the glow phase [19]. The duration of this transient glow is strongly dependent upon the circuit resistance, and decreases as the gas pressure in the gap increases [20].

At high overvoltages or pressures above atmospheric pressure, the critical charge carrier number in the initial avalanche, of approximately 10^8, is reached in a mid-gap position and the breakdown develops like a streamer, as described in section 2.1.1.3. In this case, no transient glow discharge takes place and the only visible manifestation of breakdown is the formation of a filamentary discharge. The arrival of the streamer at the cathode surface does not lead directly to arc discharge. A further arc-forming stage in the evolution of the breakdown has to take place before the applied voltage collapses to arc level [21]. The general evolution in air at atmospheric pressures consists of the following sequence: primary streamer, secondary streamer, and transient arc [22]. The time between the impact of the primary streamer and the arc formation depends on the discharge current and pressure. When the pressure increases up to 10 bar, like in spark plugs, the duration of the transition decreases to a few nanoseconds [23].

2.1.3 Arc and Glow Discharges

2.1.3.1 Voltage-Current Characteristic

Any real circuit with a discharge gap has a resistance which sets an absolute limit for the current achievable at a given electromotive force from the power supply. In an ignition circuit, this limit can be set by the resistance of the high-voltage cable, the plug connector or the spark plug. As the current largely determines the type of discharge, the resistance will influence the discharge mode after breakdown. The type of discharge can be approximately read from the voltage-current characteristic plotted in Figure 2.6. After breakdown, the current is sustained by the same avalanche mechanism as in the Townsend breakdown (point D), except that a smaller voltage is required to maintain the necessary ionization. This steady discharge is characterized by a relatively constant voltage drop, a cold cathode and a number of luminous zones. Hence, it is called glow discharge (point E). The glowing region is also

characterized by a fairly constant current density, i.e., as the current increases, the cross-sectional area of the glow increases. When the current increases to the point where electron emission originates from the entire cathode area, further increase in current leads to higher current density. This leads to Joule heating of the cathode, with further increase in electron emission, and the corresponding regime is called abnormal glow (point F). Intense cathode heating and the consequent increase in electron emission finally allows the discharge to be sustained at lower voltages and when i~1 A, the glow discharge transforms into an arc (point G). The arc region is characterized by low voltage and high current together with a highly luminous discharge (point H). This followed the voltage-current curve as the current gradually increases. However, in ignition discharges, and for sufficiently high applied voltage, the discharge can set in its corresponding discharge mode immediately after the breakdown [8].

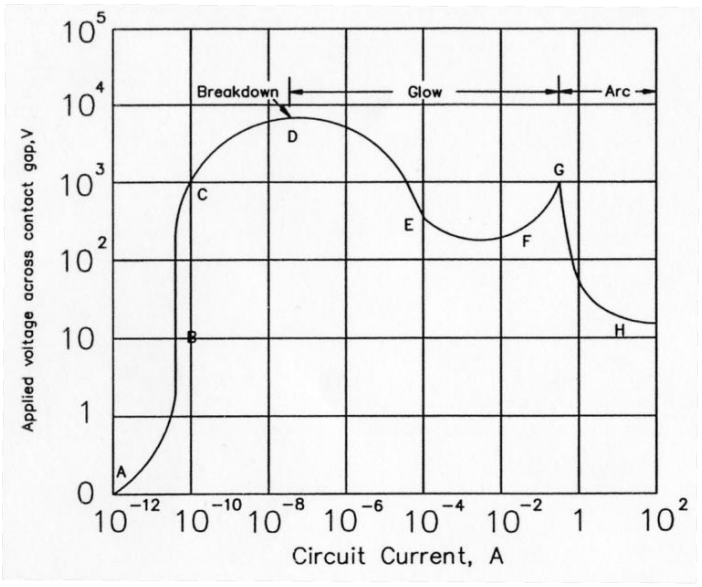

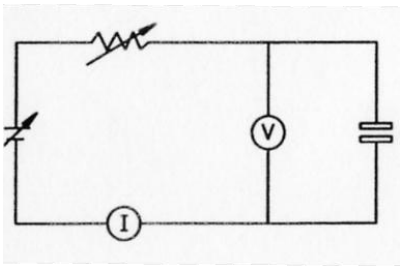

Figure 2.6 Voltage-current characteristic of a gas discharge between two separated electrodes [17].

2.1.3.2 Arc Discharge Plasma

The arc discharge is characterized by large currents, i~1-10^5 A, and high cathode current densities, J~10^2-10^7 A/cm^2, depending on the cathode material and arc mode. The burning voltage of an arc is low (~50 V in air at 1 bar with a 1 mm gap) and the cathode potential fall is on the order of the ionization potential of the cathode atoms, i.e., 10 to 20 V. The cathode fall is required to maintain electron emission from hot cathode spots (10-30 µm in diameter with T up to the boiling point of the cathode material) via thermionic, field or thermo-field emission. A more detailed review of the different cathode phenomena and electron emission mechanisms can be read in sections 2.2.1 and 2.2.2.

At atmospheric pressure or above, the arc column plasma is typically in local thermodynamic equilibrium (LTE) and T_e (electron temperature)=T_i (ion temperature)=T_g (gas

temperature) [17]. The density of electrons n_e equals the density of ions n_i and amounts to ~10^{17} e/cm^3. For low-current arcs (i~5 A), the temperature is between 6000 and 7000 K, which corresponds to the values reported for the arc phase of ignition discharges [2, 24]. For high-current arcs (i~1000 A), the temperature can reach up to 20 000 K. The energy of the arc is given by the current flowing in the arc column multiplied by the voltage drop (i.e. Joule heating) and is balanced by radial thermal losses and radiation [25]. The energy transfer from the plasma center to its surface occurs by heat conduction and mass diffusion. These processes become more inefficient the larger the column radius grows and determine the Gaussian shape of the temperature profile (Figure 2.7).

2.1.3.3 Glow Discharge Plasma

The glow discharge is one of the most studied and widely applied types of gas discharge. The name "glow discharge" comes from the presence of successive dark and bright luminous layers in the cathode region [26]. The interelectrode space of the glow discharge is an example of weakly ionized nonequilibrium plasma sustained by an electric field. Typical currents are i~10^{-4}-10^{-1} A and the current densities are low, J~1-10 A/cm^2. In normal glow discharge, current density in the region near the cathode is relatively constant, which implies that the cross-sectional area is proportional to the current [27]. Glow discharge is usually achieved at low pressures (few Torrs). However, it can also be produced at atmospheric pressures as long as the current density remains below the threshold for glow-to-arc transition (section 2.1.3.4). For constant currents, the current density in normal glow discharge increases with the square of the pressure, J~p^2 [28, 29]. At low pressures, appreciable parts of the cathode surface are covered by the plasma. High pressures tend to compress this area and favor, therefore, the transition to the arc regime.

As the current is low, the field strength in the gap region is on the order of 10^3 V/cm. The total burning voltage at 1 bar with a 1 mm gap amounts to 500 V. The plasma voltage increases with increasing pressure. The steady-state values for electron density and kernel temperature are 2×10^{14} cm^{-3} and 3000 K, respectively [1]. The energy transport mechanisms from the kernel to the plasma surface are the same as for the arc, and the plasma presents a Gaussian temperature profile (Figure 2.7). The erosion rates associated with the glow regime are low and are mainly caused by sputtering (section 2.4.3).

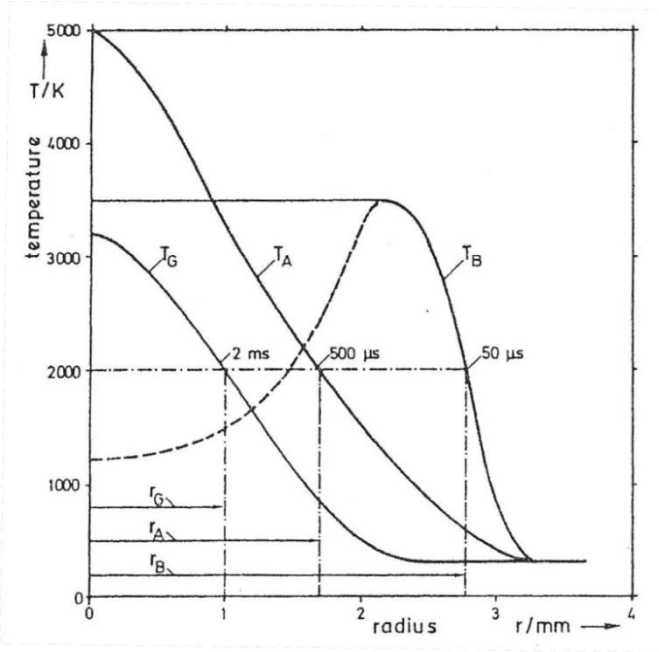

Figure 2.7 Radial temperature profiles T_B, T_A and T_G for breakdown, arc and glow discharge plasmas respectively, in air at 300 K and a 1 mm gap. Due to different power levels, final profiles will be reached at different time intervals. The breakdown profile is shown at the time of ceasing pressure expansion. r_B, r_A, r_G: plasma radii for an assumed flame temperature of 2000 K [1].

2.1.3.4 Glow Instabilities and Glow-to-Arc Transition

The threshold for the glow-to-arc transition can be reached by either increasing the current at constant pressure or increasing the pressure at constant current. For ignition sparks at atmospheric pressures, the threshold current is in the range of 100 mA. In this current range, rapid transitions occur between the arc and the glow regimes due to instabilities. For a given current density, the time constant for these instabilities decreases with increasing pressure and can be a few nanoseconds at atmospheric pressures [29]. The origins of the instabilities that could lead to glow-to-arc transition have been widely investigated. Early investigations focused on conditions at the electrodes such as cathode material and chemical processes at the cathode [30, 31]. Boyle [32] established field emission as the cause of the transition from a glow to an arc and concluded that small differences in the work function or in the surface roughness will have a large effect on the stability of the glow at high pressures. It became later evident that processes in the plasma could also affect this transition. These processes can be grouped into two types: electronic and thermal instabilities [27]. Thermal instability is the perturbing mechanism for glow discharges at elevated pressures and sufficiently high currents in atomic and molecular gases. It results in discharge contraction, and in the formation of currents filaments in which the degree of ionization and the gas temperature are much higher than in an ordinary glow discharge. The transition from a diffuse to a contracted glow discharge leading to the formation of filaments is sometimes referred to as arcing. Filament characteristics, such as the electron temperature and the electron density, lie between those of the nonequilibrium plasma of diffuse glow discharges and the

equilibrium plasma of arc discharges [8]. Transitions between glow and arc phases are an important phenomenon occurring in ignition discharges and will be discussed at the end of Chapter 4.

2.2 Cathode Processes

The surfaces of the electrodes separate two completely different conducting media from each other. The charge carriers, mainly the electrons, have to cross these boundaries. However, the electric potentials of the electrons are of a different level: near the Fermi level in the conduction band of the metallic electrode on the one hand, and near the vacuum potential of the gas/plasma on the other hand. This difference, in the simplest case, is characterized by the work function ϕ of the material. The main difficulty encountered by any gas discharge is to overcome this potential drop. The situation is different at the anode and at the cathode. The anode simply collects the electrons carrying the current from the discharge plasma. As long as the current densities are not too high, the anode is a passive electrode and the occurring processes are relatively simple. The situation is more complicated at the cathode, where electrons have to be extracted from the cathode surface. The emission of electrons at the cathode surface is realized by a system of space charge layers generated by the discharge itself, and involving many interconnected physical processes in a self-sustaining way. In this section, a review of the cathode processes occurring during the arc and glow discharges is made.

2.2.1 Cathode Layer

The potential drop of arc and glow discharges between two separated electrodes can be divided into three regions: cathode region, plasma column, and anode region (Figure 2.8). The potential fall in the anode region U_a forms to control the influx of electrons to the anode in accordance with the discharge current. The plasma column is an electrically neutral plasma (n_e=n_i) in local thermodynamic equilibrium (LTE) for the arc discharge (T_e=T_i) and in non-thermodynamic equilibrium for the glow discharge (T_e>T_i). The function of the cathode layer is to create the conditions for the self-sustainment of the current. The value of the cathode fall U_c is different in glow and arc discharges due to the different types of electron emission resulting in different ratios of electronic and ionic currents at the cathode.

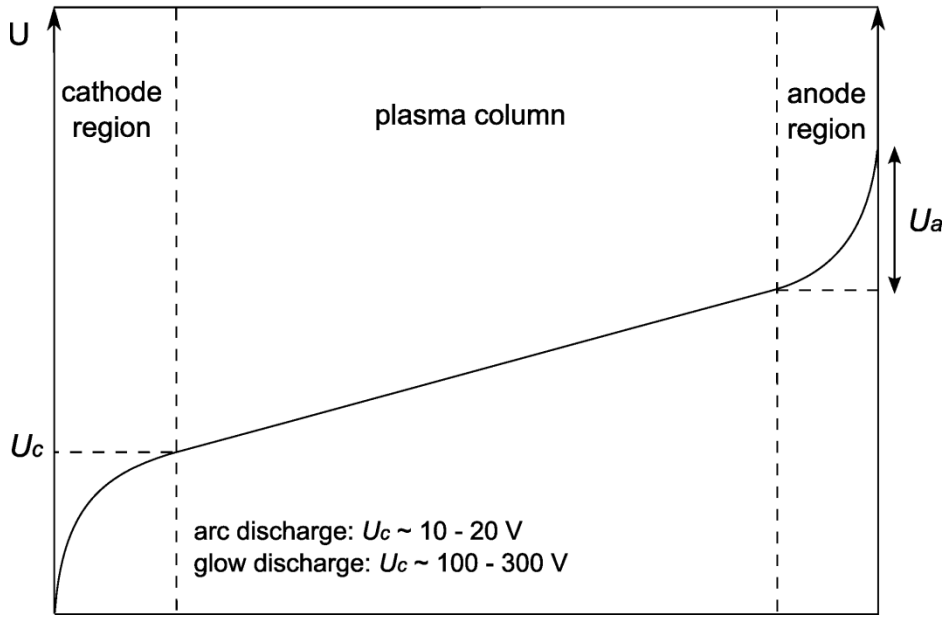

Figure 2.8 Schematic representation of the voltage in the inter-electrode space with potential falls U_c and U_a in the cathode and anode regions, respectively.

The emission of electrons at the cathode of a glow discharge is ensured by secondary emission due to the ionic flux (individual process). This is a strictly linear emission process, in which the emission current is proportional to the impacting flux of ions. Secondary emission produces only $\gamma \sim 10^{-3}$-10^{-1} electron per ion, so that the fraction of electronic current at the cathode is $\gamma/(1+\gamma) \sim 10^{-3}$-$10^{-1}$. Several generations of electrons must be produced in the cathode layer in order to raise this fraction to unity. This multiplication of electrons requires strong fields and it results in a cathode fall of hundreds of volts. For a normal glow discharge, the cathode fall U_c and the cathode layer thickness values are close to U_{min} and $(pd)_{min}$ for the breakdown of a plane gap discharge in the same gas and for the same cathode material. The lowest possible voltage fall is connected with a current density enabling optimum output of these electron generation processes [8].

The emission of electrons at the cathode of an arc discharge is produced by thermionic or thermo-field emission. This method of extracting electrons not by knocking them out individually, but by heating the surface (collective process) is more efficient than the secondary emission. Thermionic electron emission provides s~70-90 % of the total current, and ions carry 10-30 % of this current to the cathode. No additional generation is required and the cathode fall is much lower than for a glow, i.e., 10-20 V. This high efficiency, however, can be achieved only with high current density which sufficiently heats the cathode surface.

The arc cathode region is composed of a cathode sheath and an ionization zone or pre-sheath (Figure 2.9) [33-37]. The cathode sheath is collisionless and its charge is positive. In the cathode sheath, the ions generated by ionization in the pre-sheath are accelerated towards the cathode. The thickness of the cathode sheath is smaller than any collision mean free path, i.e., ~0.01 μm [38]. This layer consumes a considerable fraction of the cathode potential fall. The pre-sheath or ionization layer is a quasi-neutral plasma, which provides charged species by ionization of the vaporized atoms. The ionization of neutrals is mostly assumed by the electrons emitted from the cathode.

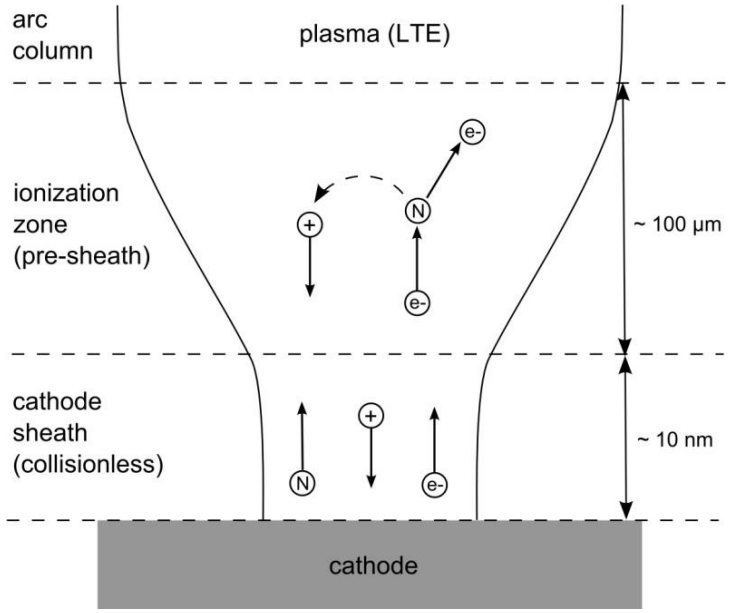

Figure 2.9 Structure of the cathode region of an arc on a cold cathode. The pre-sheath is responsible for the formation of charged particles while the cathode sheath is responsible for the important electric field at the cathode surface.

2.2.2 Arc Discharge and Cathode Spot

2.2.2.1 Electron Emission

The emission of electrons from the cathode is governed by the surface temperature T_s, the surface electric field E_s, and the presence of ions in the cathode region [39]. When the emission is only due to the temperature effect and the surface electric field is low, the emission is said to be thermionic and the electron current density J_T can be predicted by the Richardson-Dushman equation:

$$J_T = \frac{4\pi e m_e (k_B T_s)^2}{h^3} \exp\left(-\frac{e\phi}{k_B T_s}\right) \tag{2.8}$$

where ϕ is the work function of the cathode material. High surface electric fields induce a reduction of the work function, allowing easier thermal emission of the electrons. This effect

is known as the Schottky effect [40]. The work function ϕ in equation (2.8) should be replaced by the modified work function ϕ':

$$\phi' = \phi - \sqrt{\frac{e^3 E_s}{4\pi\varepsilon_0}} \tag{2.9}$$

The Richardson-Dushman formula with the modified work function is commonly called the field-enhanced thermionic equation. Prediction of the emission current with this equation is sufficiently accurate for refractory cathodes like tungsten, which are known to be thermionic emitters. However, the field-enhanced thermionic equation leads to a large underestimation of the current density for cold cathodes like Cu or Ag. This equation is therefore suitable for the prediction of the emission current of refractory cathodes with moderate surface electric field strengths E_s<10^8 V/m [41, 42]. In the case of electron emission by a pure electric field effect, the current density is given by the Fowler-Nordheim equation for field emission [43].

The combined action of thermionic and field emission is the most effective emission process and can lead to an increase by a factor of more than 500 compared with the sum of the two single effects [44]. This non-linear enhancement of the emission is necessary to fulfill the existence conditions of electric arcs with cold cathodes such as copper or silver. The combined thermal and field effect is called the thermo-field (TF) emission [45]. According to Murphy and Good [46], the thermo-field emission current density J_{TF} is related to the surface temperature T_s, the surface electric field E_s and the work function of the material ϕ by:

$$J_{TF} = \int_{-W_a}^{\infty} D(E_s, W) \cdot N(W, T_s, \phi) dW \tag{2.10}$$

where -W_a is the effective potential of electrons inside the metal surface (-W_a~10 eV), $D(E_s,W)$ is the electron tunneling probability across the potential barrier at the surface, and $N(W,T_s,\phi)$ is the Fermi-Dirac energy distribution function of electrons moving towards the surface. An example of the thermo-field current density calculated with the Murphy and Good formalism as a function of temperature and electric field is shown in Figure 2.10 for a work function ϕ=4,5 eV. This value of the work function corresponds approximately to pure tungsten (ϕ_W=4,54 eV) and pure copper (ϕ_{Cu}=4,45 eV) surfaces. Due to the complexity of the equation, the prediction of the thermo-field current densities implies the use of numerical methods. Approximation formulae of the Murphy and Good formalism exist in the literature but their use is restricted to defined ranges of temperature and electric field, and is only given

for some cathode materials [47, 48]. The Murphy and Good equation is assumed to be the most accurate for the prediction of the electron emission current of cold cathodes [42].

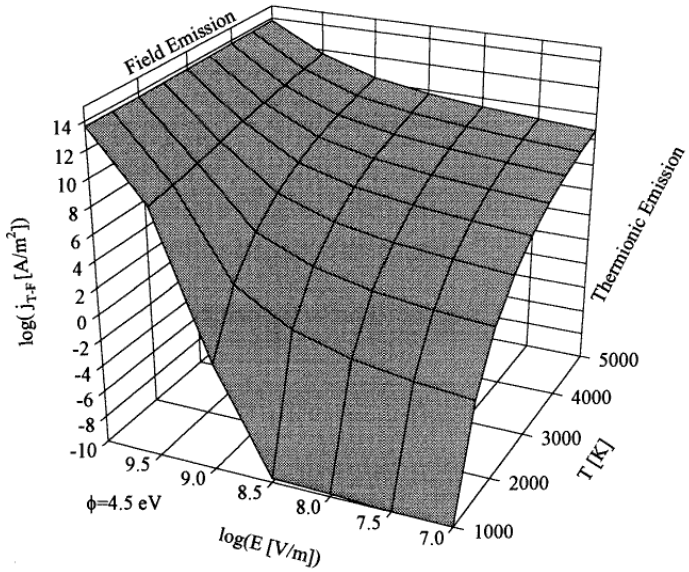

Figure 2.10 Logarithm of the thermo-field emission current density predicted by the Murphy and Good equation for ϕ=4,5 eV. The TF current density tends to become independent from the electric field for small fields (thermionic emission) and independent from the temperature for large fields (field emission) [42].

2.2.2.2 Basic Cathode Spot Mechanisms

Considering the different electron emission processes, cathodes of high pressure arcs can be classified as thermionic (hot cathodes) or non-thermionic (cold cathodes). Thermionic cathodes are made of high melting point materials such as W or Ir, and can sustain the high temperatures needed for thermionic emission without considerable melting or evaporation. The cathode arc root can be contracted (spot mode) or diffused and the current density is J~10^7-10^8 A/m^2 [49-52]. Non-thermionic cathodes made of non-refractory materials such as Cu or Ag cannot sustain high temperatures and they are expected to emit electrons in the thermo-field regime. The cathode spot processes associated with this last regime are presented in more detail here. These mechanisms will be mentioned later in Chapter 6 for the elaboration of the FEM simulation as well as for the discussion of the results.

The arc cathode spot must provide a sufficient yield of thermo-field electrons. Therefore, both the temperature and the electric field at the surface of the spot must be high enough. These conditions are achieved by the discharge itself, leading to the contraction of the arc spot until sufficient emission occurs. The cathode spot is heated by the impact of accelerated ions, which deliver their kinetic, thermal and recombination energy. Ions flowing toward the cathode also generate a strong electric field at the cathode surface because of their space charge. The calculation of the electric field requires solving the Poisson equation in the cathode sheath. A first analytical expression for the surface electric field E_s was originally developed by Mackeown [53] considering the ions and the emitted electrons:

$$E_s{}^2 = 7{,}57.10^5 \sqrt{U_c}\left(J_i \sqrt{1845 \cdot M} - J_e\right) \tag{2.11}$$

where U_c is the cathode potential fall, M is the atomic weight of the positive ion, and J_i and J_e are the ion and electron current densities, respectively. Different extended expressions of the Mackeown equation are proposed in the literature [37, 47, 54-58].

The ion flow towards the cathode produces both high temperatures and strong electric fields at the cathode spot surface. Thus, it provides the necessary conditions for sufficient high-yield electron emission and for the existence of the arc [44]. Since ions are generated by the ionization of neutrals in the cathode pre-sheath, the self-sustaining operation of an arc requires a sufficiently intense evaporation of cathode material. The presence of a dense metallic vapor in the cathode region will have the effect of maintaining an intense ion bombardment, which, in turn, allows high ion and electron current densities. The flux density of evaporated atoms Γ_n can be estimated by means of the Langmuir formula:

$$\Gamma_n = \frac{p_v}{\sqrt{2\pi m_n k_B T_s}} \qquad \text{with} \qquad p_v = -\frac{A}{T_s} + B + C \cdot log(T_s) \tag{2.12}$$

where m_n is the particle mass and p_v is the equilibrium vapor pressure of the cathode material. The constants A, B and C are found in tables (Appendix E).

High local vapor pressures in the cathode region are necessary for the self-sustainment of arcs on cold cathodes not only in vacuum [59], but also at atmospheric pressures [49]. Coulombe [37, 60] reported theoretical values of metallic pressure up to 50 atm to achieve the transfer of current densities of ~10 A/m^2 on copper cathodes. According to many authors [61-63], the basic operating mechanisms of arc cathode spots in vacuum and in gaseous media are similar and can be described by the same unique model. This can be explained by the fact that, if the local metallic pressure is higher than the external pressure, the internal structure of the cathode spot is not disturbed by the surrounding ambient gas. Moreover, as most metal vapors have lower ionization potentials than nitrogen, oxygen or other gases, any metal vapor in the cathode region will be preferentially ionized. Like in vacuum, the returning ions in high pressure arcs come from the cathode and not from the ambient gas.

The abovementioned cathode spot mechanisms describe a stationary phenomenon. In order to complete this model, new concepts were introduced such as, among others, the thermal runaway and the explosive emission [44, 64-67].

2.2.2.3 Crater Formation

Craters are *post-mortem* visible traces of the intense interaction between the plasma and the cathode surface occurring at the cathode spot. The craters are formed by (1) intense heating of the surface up to the boiling point, mainly caused by ion bombardment, (2) formation of a thin molten layer at the surface, and (3) formation of a depression due to the high plasma pressure acting on the surface (~1 GPa [44]), which pushes the liquid metal outwards to the crater rim, where it cools and solidifies. A simple form for the ion pressure p_{ion} acting on the crater surface is given by:

$$p_{ion} = J_i \sqrt{\frac{2U_c m_i}{Z_i e}} \tag{2.13}$$

where J_i is the ion current density, U_c is the cathode fall, m_i is the mass of the positive ion, and Z_i is the mean ion charge (=1). Hantzche [55], Prock [68, 69] and Jüttner [70], among others, have treated the crater formation mechanisms in detail.

The *in-situ* observation of cathode spots is complicated and requires measurement techniques with high temporal and spatial resolutions [71, 72]. Moreover, the cathode spot is surrounded by a plasma emitting light, which prevents the direct visualization of the spot and the accurate determination of its dimensions, especially in an ambient gas. This is the reason why the arc cathode roots observed *in-situ* with photographic techniques are much larger than the craters left on the surface [73]. Craters show the extent of the power and current transfer region on the cathode and it is generally assumed that the size of the crater corresponds to the size of the cathode spot. Therefore, the investigation of the crater region can provide very useful information about arc-cathode interaction. Combined with the measurement of the current, the size of the crater can yield information about the mean current density at the cathode spot.

Craters are typical features of the arc attachment on non-refractory cathodes due to the important contraction of the arc foot. Indeed, the trace left by the arc on a refractory cathode is rather a gross melting of the surface without depression zones [74]. Arc attachment on non-refractory cathodes consists of one or several cathode spots. At room temperature, the mean crater diameter remains nearly constant at values of 5-10 µm [75-77]. The independence of the individual crater size on the arc current can be explained by spot division [78]. As a consequence, erosion structures >10 µm can be explained by the action of a multitude of spots rather than by a single one. Cathode spot lifetimes reported in the literature differ by orders of magnitude with values ranging from some nanoseconds to some microseconds [79, 80]. The

current densities in a spot on non-refractory cathodes such as Ag, Au, and Cu are reported to range from 10^{10} to 10^{12} A/m^2 [49, 79, 81].

2.3 Energy Balance in Ignition Discharges

2.3.1 Energy Transferred to the Plasma

The purpose of the ignition discharge is to initiate the combustion of the air/fuel mixture by delivering its energy to the gas/plasma at the right moment. However, only a small fraction of the electrical energy is actually transferred to the plasma. A large part of the energy is lost in the electrodes. This unwanted energy does not contribute to the ignition of the mixture and reduces the efficiency of the ignition spark. Moreover, it leads to heating and degradation of the electrodes. The reason why the total electrical energy cannot be transferred to the plasma is that the electrode processes necessary for the sustainment of the discharge require energy. At the cathode, ions gain energy through acceleration in the strong electric field of the cathode layer. This energy will heat the cathode surface in order to supply the emission of electrons. However, a large fraction of heat is lost through conduction into the bulk of the cathode. Electrons absorbed at the anode also transfer their energy via recombination and heat the anode.

The ignition energy efficiency can be defined as the fraction of electrical energy deposited in the gas/plasma. This value is important for the characterization of the ignition system but also for the comprehension of the plasma-electrode interaction and electrode degradation mechanisms. Ignition energy efficiency values based on calorimetric measurements are reported in the literature [82, 83]. The electrical energy can be easily determined from the electrical parameters of the circuit coupled with the oscilloscopic measurement of the voltage and current curves. The thermal energy deposited in the plasma can be determined from measurements of the transient pressure rise following the discharge in a closed chamber (constant volume). The energy transfer efficiency is found to be different for each phase of the discharge [82]. The energy transferred to the plasma is plotted as a function of the electrical energy for the different phases of the discharge in Figure 2.11.

2.3.1.1 Breakdown Phase

During breakdown, the energy stored in the plug capacitor is discharged within a few nanoseconds. The electrical energy of the breakdown phase E_{br} is given by:

$$E_{br} = \frac{1}{2} C_p U_b^2 \tag{2.14}$$

where C_p is the plug capacitance and U_b is the breakdown voltage. The breakdown phase shows the higher efficiency of the three phases with approximately 90 % of the electrical energy transferred to the plasma. The high efficiency of the breakdown is due to the very short time (~ns) in which the energy is released in the inter-electrode space. Therefore, cooling processes at the electrodes cannot take place. However, the efficiency decreases as the stored energy increases (Figure 2.11). This is likely caused by the presence of a succeeding arc phase if the energy stored in the capacitor cannot be discharged completely during the breakdown phase.

2.3.1.2 Arc and Glow Phases

The arc and glow phases correspond to the discharge of the energy stored in the ignition coil. Using the voltage and current curves of the discharge, the corresponding electrical energies E_a and E_g can be calculated:

$$E_a = \int_{t_a} u_a(t) \cdot i_a(t)\, dt \tag{2.15}$$

$$E_g = \int_{t_g} u_g(t) \cdot i_g(t)\, dt \tag{2.16}$$

where t_a, t_g, u_a, u_b, and i_a, i_b are the duration, the burning voltage and the current of the arc and glow phases, respectively. The energy transfer efficiencies of arc and glow discharges are low in comparison with those of the breakdown phase due to the formation of cathode and anode layers and the heating of the electrodes. The efficiency of the arc discharge ranges from 50 % for electrodes having a small diameter (∅=0.1 mm) to 10 % for electrodes having a large diameter (∅=2.5 mm). The cathode material also plays a role and materials having a low boiling point increase the ignition efficiency of the discharge. The glow phase shows efficiencies somewhat lower, between 30 and 10 %, likely due to higher cathode falls. As with the arc phase, the glow efficiency decreases as the electrode diameter increases. Teets [83] investigated the efficiency of glow discharges at different pressures and gap lengths. His results are comparable with those of Saggau [82] for the glow discharge. He showed that the energy transferred to the plasma increases when the gas pressure and the gap length increase. Since losses via radiation are negligible [5], the fraction of energy not transferred to the

plasma is entirely lost in the electrodes, and it is admitted that 2/3 goes to the cathode and 1/3 to the anode [84].

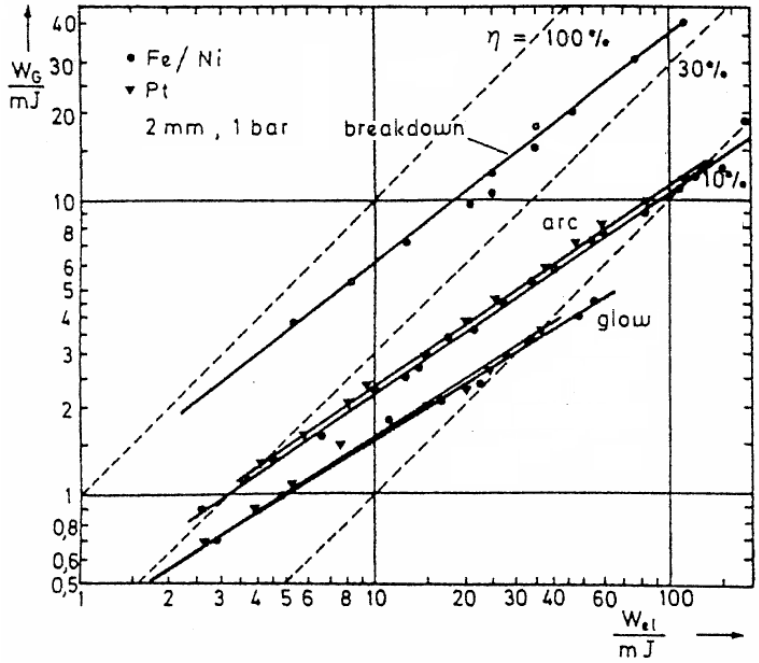

Figure 2.11 Energy transfer to the plasma as a function of stored electrical energy for the different phases of an ignition discharge [82].

2.3.2 Energy Balance at the Cathode Spot

In this section, the basis of the physical model used for the FEM thermal simulation in Chapter 6 is established. The different physical mechanisms taking place at the cathode spot can be classified into heating and cooling mechanisms.

2.3.2.1 Heating Mechanisms

The principal contribution to cathode surface heating is the bombardment of returning ions. Each ion impacting the surface liberates an effective energy equal to the sum of: its thermal energy, corresponding to the plasma ion temperature T_i; its kinetic energy, gained in the cathode fall potential U_c; its neutralization energy, from the recombination with electrons from the metal; and its condensation energy, which is equal to the evaporation energy. The assumption that all ions condense is not always made and some authors consider that all ions are backscattered after neutralization [37, 85]. The corresponding heat flux P_i is given by:

$$P_i = J_i \cdot U_i \tag{2.17}$$

where J_i is the ion current density, and U_i is the effective energy of each ion described above.

Not only ions but also neutral atoms and electrons return to the cathode. Returning atoms contribute to cathode heating by P_{rn} from their thermal and condensation energy:

$$P_{rn} = \Gamma_{rn}\left(W_{ev} + 2k_B T_p\right) \tag{2.18}$$

where Γ_{rn} is the flux density of returning neutrals, W_{ev} is the evaporation energy and T_p is the plasma temperature. Since only a small fraction of vaporized atoms return to the cathode, the power density of returning neutrals P_{rn} is usually negligible in comparison with ionic bombardment [47].

Though the cathode is at a lower potential than the plasma, some electrons can return to the cathode because of the high plasma temperature. Upon impact with the cathode surface, back-diffusing electrons liberate the sum of their condensation energy and initial enthalpy giving rise to the heat flux P_{bde}:

$$P_{bde} = J_{bde}\left(\phi' + \frac{5k_B T_e}{2e}\right) \tag{2.19}$$

where J_{bde} is the back-diffusing electron density, ϕ' is the modified work function and T_e is the plasma electron temperature. According to Rossignol [86], the power density associated with back-diffusion electrons P_{bde} is two orders of magnitude lower than the ionic bombardment P_i and can then be neglected.

Radiations emitted from the plasma are absorbed at the surface. The radiation power of the plasma $P_{r,p}$ can be estimated by the Stefan law:

$$P_{r,p} = \sigma T_e^4 \tag{2.20}$$

where σ is the Stefan-Boltzmann constant. The radiation power of the plasma is considered to be negligible in comparison with other heating terms [47, 86, 87].

The heating terms mentioned in the above paragraphs are surface terms. Additionally, the electric current flow in cathode bulk can result in Joule heating, which is a volume source. The equivalent power density P_j can be evaluated by [47]:

$$P_j = \frac{k' J^2 a}{\sigma_{el}} \tag{2.21}$$

where J is the current density, a is the spot radius, σ_{el} is the electrical conductivity and k' is a constant in the range of 0.5-0.8. Many authors [69, 85, 88, 89] consider that Joule heating is negligible in comparison with ionic bombardment.

2.3.2.2 Cooling Mechanisms

The thermo-field emission of electrons from the cathode spot surface is coupled with a cooling effect (so-called Nottingham effect) because the electrons are promoted outside the potential barrier of the metal surface by taking their energy from the lattice. The net energy exchange of each electron leaving the surface with the cathode is called the Nottingham potential [90]. Using the fitting formula proposed by Paulini *et al.* [48], the power density associated with electron emission P_e can be predicted by:

$$P_e = \frac{J_e}{e}(\phi' + 2k_B T_s) \tag{2.22}$$

where the emitted electron current density J_e equals J_{TF} (equation 2.10), ϕ' is the modified work function and T_s is the spot surface temperature. Note that for very high surface electric fields (E_s>10^{10} V/m) and low temperatures (T_s<2700 K), the Nottingham effect may result in a heating effect [37].

The power loss density due to the vaporization of atoms P_{vap} is given by:

$$P_{vap} = \Gamma_n (W_{ev} + 2k_B T_s) \tag{2.23}$$

where Γ_n is the flux density of vaporized atoms (equation 2.12), W_{ev} is the evaporation energy and T_s is the surface temperature.

A further loss of energy is caused by radiation of the cathode spot. Like plasma radiation, the power loss by spot radiation $P_{r,s}$ is given by the Stefan law assuming blackbody radiation:

$$P_{r,s} = \sigma T_s^4 \tag{2.24}$$

The power associated with spot radiations is usually negligible in comparison with the other cooling terms [47, 86, 87].

The remaining heat flux brought to the cathode surface is dissipated in the cathode bulk by heat conduction. This power $P_{electrode}$ is partially consumed to heat the cathode bulk and to melt the surface, forming a shallow pool of liquid metal.

Assuming that the surface is in energetic equilibrium, the power balance at the surface of the cathode spot is given by the relation:

$$P_i = P_e + P_{vap} + P_{electrode} \tag{2.25}$$

2.3.3 Energy Balance at the Cathode in Glow Discharges

During glow discharge, energy is delivered to the cathode in the form of bombarding ions and energetic neutrals. Since the degree of ionization in the glow discharge plasma is low, the most abundant species are neutrals. Experimental and theoretical investigations of heat transfer mechanisms reported that ~80 % of total glow discharge power is supplied to the cathode and causes its heating [91, 92]. The cathode flux of fast neutrals is likely to be significantly greater than that of ions. Therefore, the main contribution to cathode heating is brought by fast neutrals and not ions [91, 93].

2.4 Erosion Mechanisms

The interaction of electrical discharges with the surface of electrodes leads to material degradation. For the development of new electrode materials with enhanced durability, the understanding of the erosion processes is crucial. Since the phases of ignition discharge involve different physical phenomena, the erosion processes taking place during arc discharge may differ from those of glow discharge. In the following section, a review is made of the most important theories developed to explain the erosion caused by electrical discharges. Mechanisms like particle ejection, vaporization and oxide layer removal apply to the highly energetic cathode arc root while sputtering applies more to the glow discharge. Plasma assisted oxidation of the surface can occur during both arc and glow phases.

2.4.1 Particle Ejection

Under the heat from ion bombardment, the cathode surface melts and forms a thin layer of molten metal. A considerable part of the liquid metal is transported to the crater rims,

whereas a small part is ejected in the form of droplets. Gray *et al.* [94] proposed a model to explain the formation and ejection of droplets (Figure 2.12). During the discharge, a force due to the ion bombardment acts on the surface of the molten pool (equation 2.13). This force is balanced by a recoil force directed outward from the cathode bulk. Following the abrupt cessation of the ionic force at the extinction of the arc discharge, the recoil force is only balanced by the surface tension of the liquid metal, which acts against the displacement of the liquid. If the opposing surface tension force is smaller than the recoil force, a droplet will form and be ejected. Experimental evidence of this effect can be observed in [77]. As discussed by Gray *et al* [94], the liquid ejection induced by the pressure release upon arc extinction is less than 1 % of the entire liquid volume. According to Wang *et al.* [95], the ejection of particles is related with the flow behavior of the liquid in the molten pool during the ion bombardment, which is determined by the Reynolds number *Re*. If $Re<1$, the flow is laminar, while if $Re>1$, the flow will be turbulent and splashing will occur. For both mechanisms, high surface tension and high viscosity will reduce the ejection of molten droplets. The increase of the effective viscosity of molten metal can be achieved by incorporating high melting point particles in the electrode material (e.g. Ag/MeO contact materials).

Droplets can be investigated by collection on plates or by laser imaging techniques that allow *in-situ* observation. The size of the droplets varies from 0.1 µm up to about 100 µm [80]. However, most of the droplets observed around ignition discharge craters are <1 µm [96]. The velocity of the droplets may reach several 100 m/s [97, 98]. This high velocity indicates fast surface processes and supports the idea of short formation times for craters [69].

The melting of the surface coupled with the ejection of particles was found to be the most suitable mechanism to explain the loss of material in craters caused by single ignition discharge experiments [99]. This mechanism is supported by the observation of metal droplets around the craters. However, the particle ejection model is no longer appropriate to describe the wear of electrodes in endurance tests [100]. The absence of this effect in endurance tests can be explained by the re-deposition of most of the ejected particles on the electrode surface, resulting in no net loss of material.

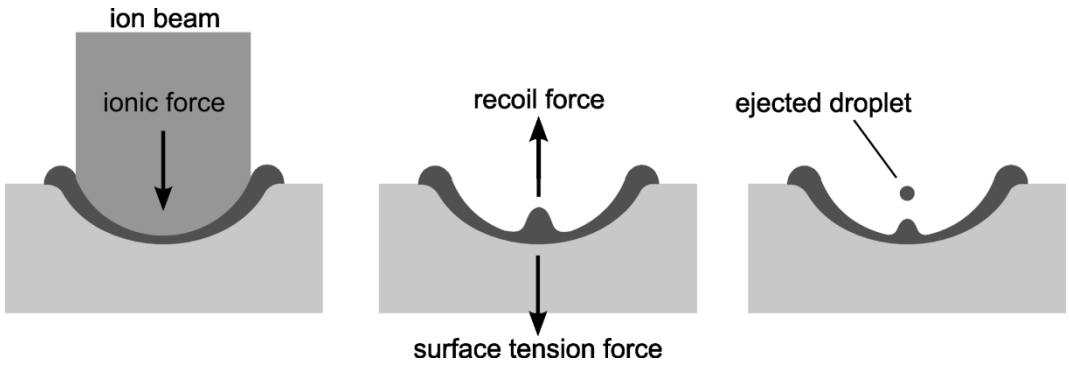

Figure 2.12 Schematic representation of the particle ejection model according to Gray *et al.* [94]. Following arc extinction, the recoil force is balanced by the surface tension force. If the recoil force is greater than the surface tension force, a droplet will be ejected.

2.4.2 Vaporization

Vaporization of cathode material is an important phenomenon contributing to the self-sustainment of arc discharges on cold cathodes (section 2.2.2.2). The flux of emitted atoms Γ_n in equation 2.12 corresponds to the maximum rate of vaporization occurring in a cathode spot, since the re-deposition of returning ions or back-diffusing neutrals is not taken into account. A lower limit for material vaporization is determined by assuming that all the returning ions re-condense on the surface. In vacuum arcs, the arc spot plasma is not as confined to the cathode surface when compared to atmospheric arcs. Therefore, a considerably lower fraction of ions re-condense on the cathode surface, leading to higher erosion rates. According to Benilov *et al.* [101], the effect of vaporization on the energy balance of the cathode spot and on the net erosion rate is determined by the ratio of equilibrium vapor pressure p_v (equation 2.12) to ambient pressure p. If p_v/p is smaller than unity, the net flux of vapor is much smaller than the emitted flux from the surface. If p_v/p exceeds approximately 4.5, vaporization occurs as in vacuum and the net flux of vapor is about 80 % of the emitted flux, while 20 % is reflected back to the surface. Theoretical predictions of the erosion rate of copper are of the order of 20-60 $\mu g \cdot C^{-1}$ [102], which are comparable with those determined experimentally (4-50 $\mu g \cdot C^{-1}$ [103]). An overview of the arc erosion rates of different cathode materials is given in [80].

Llewelyn-Jones [104] considered evaporation from the cathode spot area as the dominating erosion mechanism caused by sparks. His model is based on the energy balance on the surface of the electrode at its boiling point. Considering the energy required to heat the material to its boiling point and the energy lost via radiation and conduction, he proposed the following equation to calculate the volume of eroded material V_e:

$$V_e = \frac{aU_b^2 - bT_b^4 - ck(T_b - T)}{\rho\left[c_p(T_b - T) + 21\frac{T_b}{M}\right]} \tag{2.26}$$

where T_b is the boiling point, k is the thermal conductivity, ρ is the density, c_p is the specific heat capacity and M is the molecular weight. The constants a, b and c can be adjusted depending on electrode material, spot size and spark duration. Although the equation was initially developed considering that the heat input is provided by the breakdown phase (breakdown voltage U_b in the numerator), it can also be adapted for the arc phase by adjusting the constant a. Chemical attacks such as oxidation and energy lost by electron emission are not taken into account in the Llewelyn-Jones equation.

2.4.3 Sputtering

Sputtering of atoms from the surface is one possible mechanism responsible for electrode erosion. The sputtering is caused by the mixture of accelerated ions and fast atoms bombarding the cathode surface [105]. If, following bombardment, collisional backscattering in the surface layers of the electrode is sufficiently energetic, atoms can overcome their binding energy and are then ejected from the surface. The average number of atoms lost per bombarding particle is called the "primary sputter yield" and is dependent on bombardment energy, masses and types of incident and target species. The primary sputter yield Y can be derived from the sputtering theory developed by Sigmund [106]:

$$Y = \frac{3\alpha_s}{4\pi^2}\frac{4M_1M_2}{(M_1 + M_2)^2}\frac{E''}{U_s} \tag{2.27}$$

where α_s is a factor function of M_1/M_2, M_1 and M_2 are the masses of target and incident particles respectively, E'' is the bombarding energy and U_s is the surface binding energy usually equated to the heat of sublimation.

Osamura *et al.* [107] and Hiro *et al.* [108] considered that sputtering contributes to electrode wear during the inductive part of the discharge, i.e., arc and glow phases, while the wear caused during the capacitive discharge, i.e., instationary arc phase, can be explained by melting and splashing of material. Therefore, the use of material with high melting point and high atomic mass will reduce the spark erosion rate. According to Nishio *et al.* [109], sputtering of atoms under the glow discharge is the principle spark erosion mechanism and particle ejection can be excluded. In the presence of oxygen, the bombardment of oxygen ions can lead to the oxidation of the cathode surface which increases the erosion rate. Augis *et al.*

[110], however, suggested that sputtering occurring under the glow phase produces only a slight degradation of the surface layer, and does not contribute significantly to electrode wear.

2.4.4 Oxide Layer Removal

Guile and Hitchcock [111-113] investigated the erosion caused by arcs on non-refractory cathodes covered with oxide films. For an oxide film thickness from 25 nm to 350 nm, the damage caused by the arc was an area stripped of oxide. The depth of the stripped area was found to be equal to the oxide layer thickness. The erosion was thought to come from sub-µm craters, which had originally contained current-carrying filaments (~10 mA) formed through the oxide. These filaments were supposed to become molten as a result of Joule heating and the molten oxide was explosively ejected from the cathode, resulting in material erosion. Dimoff *et al*. [114] performed a theoretical analysis of the heating of oxidized cathode surfaces by arcs. They showed that the melting of the surface can occur 10 to 100 times faster and for much lower current densities than on clean metallic surfaces. Therefore, the resistance of a cathode surface to arc erosion is thought to be greatly altered by the presence of an oxide layer.

Soldera [115, 116] investigated the craters produced by single ignition discharges on the surface of pre-oxidized Ni and RuAl cathodes, having a thickness up to 14 µm. The depth of the craters was found to increase linearly with the oxide thickness, while the crater depth is always larger than the oxide thickness. Therefore, the discharge must destroy the oxide scale until the plasma reaches the metallic substrate. The destruction of the oxide scale was attributed to the combination of partial discharges (see [13]) and Joule heating in the oxide film.

Goering [117] tested the erosion resistance of several electrode materials in engines. His study led to the proposal that oxide layer removal rather than metal removal is the primary erosion mechanism for spark plug electrodes. This mechanism may be applied to materials that form insulating layers such as oxides or sulfides. In the absence of a protective layer, the erosion occurs by metal removal and the erosion rates are much lower. Rager [100] concluded also that the wear of nickel electrodes in air is caused by oxide layer removal. He proposed an equation to predict the erosion rate as a function of electrode surface temperature, electrode radius and sparking frequency.

2.4.5 Plasma Assisted Oxidation

Recently, Rager [24, 100] investigated the spark erosion behavior of several materials in air and nitrogen. Since no significant loss of material was observed in nitrogen, he concluded that oxidation is the dominating effect in electrode wear. Erosion mechanisms operating analogously in air and nitrogen, such as particle ejection, sputtering and vaporization, were excluded as dominant mechanisms. In the case of a noble metal like Pt, which does not form an oxide layer at high temperatures, the oxide layer removal mechanism cannot be applied. According to Rager, the erosion of Pt electrodes occurs through oxidation in the hot cathode spot during the arc discharge. The presence of oxygen radicals and ions in the plasma greatly enhances the oxidation reaction in comparison to molecular oxygen [118]. Since PtO_2 is not stable, oxide molecules constantly escape from the spot surface in gaseous form. A part is back-reflected and re-deposited as Pt elsewhere on the surface, resulting in the formation of oriented structures. The other part is ionized in the plasma and contributes to the net erosion of the electrode.

CHAPTER 3

Experimental

3.1 Generation of Ignition Discharges

3.1.1 Pressure Chamber

The ignition discharges are produced in a windowed pressure chamber made of brass. The experimental set-up is shown in Figure 3.1.

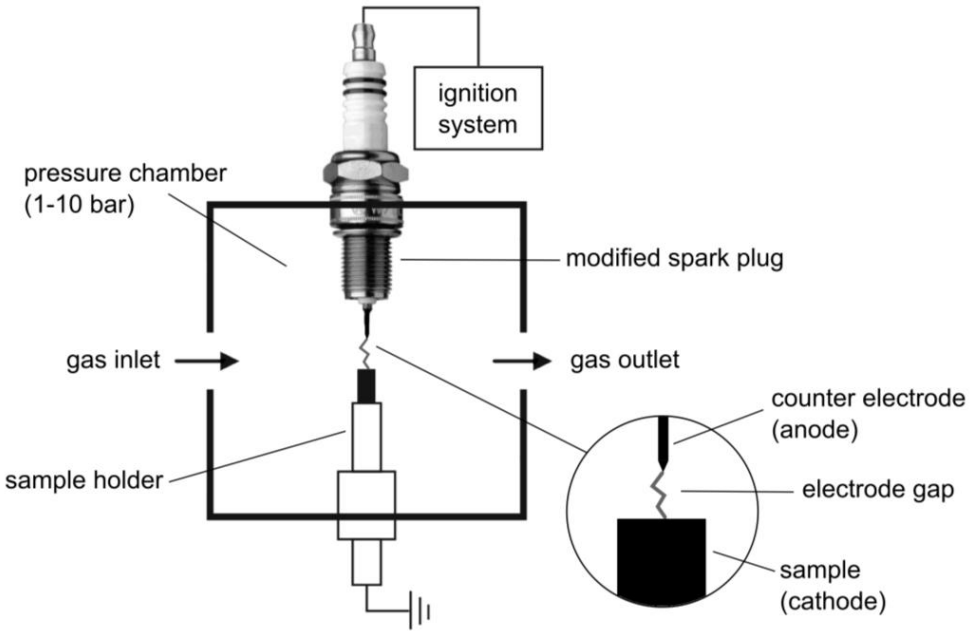

Figure 3.1 Schematic representation of the pressure chamber set-up used for the generation of ignition discharges.

The chamber is connected to gas bottles, which permit to work under various atmospheres such as synthetic air or nitrogen. The chamber pressure can be set from 1 to 10 bar absolute with pressure reducing regulators and is monitored by a manometer fixed on the chamber. Using a digital video microscope positioned perpendicularly to the electrodes, the gap can be set precisely between 0 and 3 mm without contacting the electrodes. In this work, the electrode gap is constant and equal to 1 mm. The sample consists of a cylindrical piece with a diameter of 3 mm, which is grounded and set as cathode. The counter electrode

(anode) is made of a commercially available spark plug without internal resistor, where the ground electrode was removed and a Pt-pin (∅=0.8 mm) was attached to the top of the center electrode. Due to the different geometries of the cathode and the anode, the electrode gap is said to be point-to-plane.

3.1.2 Ignition System

The ignition system used in this work, as well as commercial ignition systems, may be described by the equivalent circuit presented in Figure 3.2.

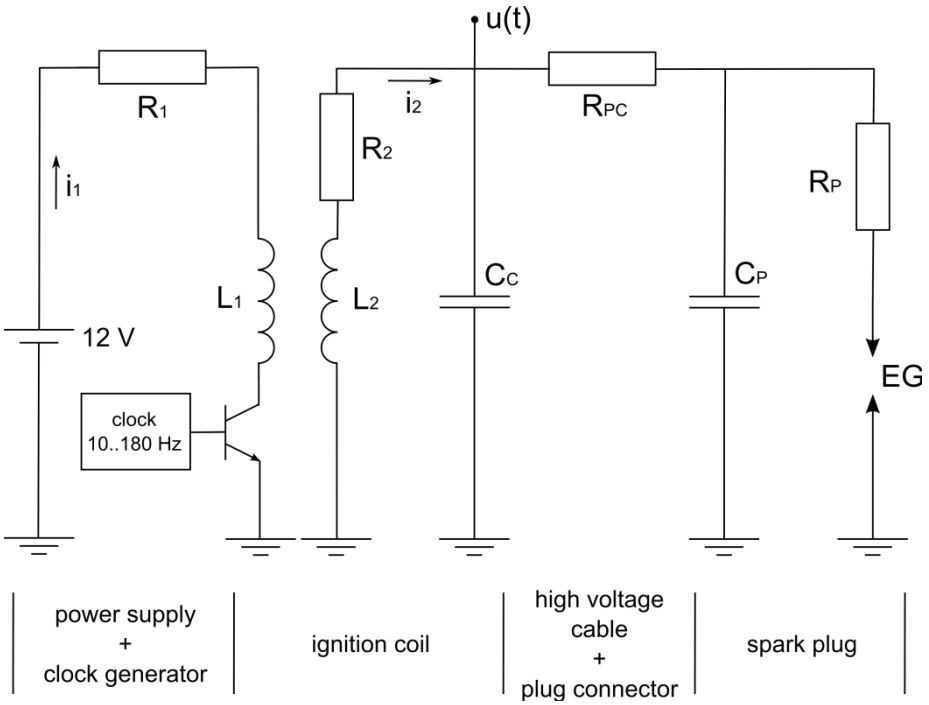

Figure 3.2 Equivalent circuit of the ignition system used for the generation of sparks. R_1, R_2: primary and secondary side coil resistances; L_1, L_2: primary and secondary side coil inductances; C_C: coil capacity; R_{PC}: resistance of the high voltage cable and the plug connector; C_P: spark plug capacity; R_P: spark plug resistance; *EG*: electrode gap; i_1, i_2: primary and secondary side currents; $u(t)$: ignition discharge voltage.

The ignition coil operates as both an energy storage device and a transformer, changing the 12 V low voltage of the DC power supply into the high voltage needed to generate the spark (20-30 kV). The frequency of the ignition impulse is produced by a transistor on the primary side operating as a simple contact breaker. The clock frequency can be varied between 10 and 180 Hz. When the primary side is closed, the energy of the power supply flows in the primary winding of the coil and is then stored in a magnetic field. The energy stored on the primary side (E_p=½·L_1·i_1^2) can be controlled by both the voltage of the power

supply and the loading time of the coil (0-10 ms). Once the primary side is open, a voltage is induced on the secondary side according to Lenz's law. The resulting energy first loads the secondary side capacitances C_C and C_P. As a result, the voltage across the electrode gap increases until the ignition voltage is reached and the spark fires.

3.1.3 Oscilloscope Measurements

Voltage and current on the secondary side are measured with a LeCroy™ WaveRunner® 6100A digital oscilloscope with a bandwidth of 1 GHz. The voltage *u(t)* is measured using two high voltage probes: one in the range of 5-25 kV for visualizing the ignition voltage (LeCroy™ PPE20kV with 1:1000 attenuation and 100 MHz bandwidth) and one in the range of 100-1000 V for visualizing the arc and glow voltages (Tektronik P6015A with 1:1000 attenuation and 75 MHz bandwidth). The secondary side current i_2 is measured with a current probe (LeCroy™ CP031 with 100 MHz bandwidth). The voltage- and current-time curves permit to gain useful information about the discharge such as ignition voltage, and duration and energy of the different phases. Typical voltage and current signals measured with the oscilloscope are shown in Figure 3.3.

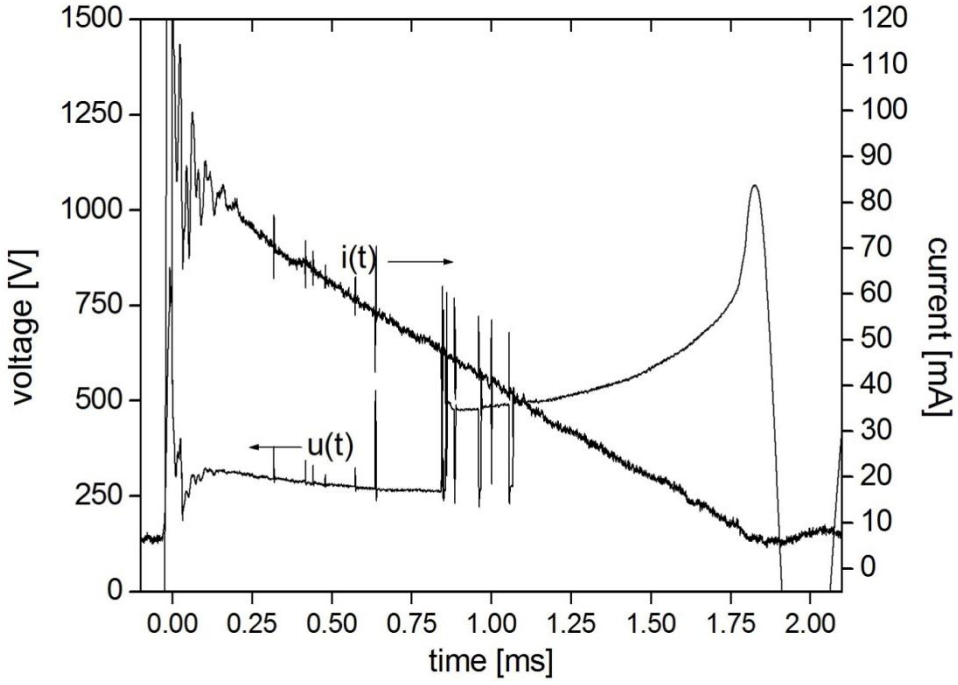

Figure 3.3 Voltage *u*(*t*) and current *i*(*t*) versus time curves of an ignition discharge measured with the oscilloscope.

3.2 Preparation of Multilayered Electrodes

The multilayered electrodes consist of bi-metallic multilayered surfaces deposited on silver rod substrates. The silver rods used as substrates have a diameter of 3 mm and a length of ~8 mm. The upper end of the substrates is polished with diamond and silicate suspensions down to 0.04 µm. The deposition of the multilayer is achieved by physical vapor deposition (PVD) in an Ar-ion gun facility (Roth & Rau, UniLab) under an Ar atmosphere of 4×10^{-4} mbar. The thickness of the layers is monitored in-situ during the deposition by a microbalance (Tectra, MTM-10) and verified later by FIB/SEM measurements. The configuration of the three multilayer systems used in this work is summarized in Table 3.1.

Table 3.1 Configuration of the multilayer systems used in this work.

Multilayer system	Layer thickness	Multilayer total thickness	surface layer
Ag/Ni	160 nm	1.6 µm	Ag
Ni/Cu	100 nm	2 µm	Ni
Pt/Ni	100 nm	1.5 µm	Pt

3.3 Electrode Surface Characterization

The characterization of the craters produced on the surface of the electrodes is based on both quantitative topographic measurements using white light interferometry (WLI), and microstructure and chemical analysis using FIB/SEM dual beam techniques.

3.3.1 White Light Interferometry

The surface of the craters is measured using a Zygo NewView 200 3D Image Surface Structure Analyser equipped with a Mirau interferometric objective (Figure 3.4a). The operating principle of this instrument is based on white light interferometry. Interference patterns of light and dark lines are produced through the interference of a reference beam and a specimen beam with a path difference. The beams are produced by a white light source (tungsten halogen lamp) which is split within the objective lens. The reference beam focuses onto an inner reference plane and the specimen beam onto the specimen surface. After reflection, the two beams are superimposed in the interferometer and there, by a process of

constructive and destructive interferences, produce the interference pattern. Interferograms for each of the image points or pixels of the surface are generated simultaneously by accurate vertical scanning of the sample surface achieved by a piezo (PZT), while interference intensity patterns are collected using a CCD camera. The data acquired in this way consists of an array of interferograms, one for each pixel, representing the variation in intensity as a function of scan position. The interferograms are processed by frequency-domain analysis (FDA) generating a quantitative three-dimensional image of the surface constructed from the height data and corresponding image plane coordinates [119]. The maximal vertical resolution which can be achieved is 0.3 nm, while the lateral resolution varies between 0.64 and 11.8 µm, depending on the objective lens used [120].

The craters were measured at high magnification (800X) with a corresponding lateral resolution of approximately 1 µm. WLI measurements provide quantitative information about crater topography of the such as height, depth and roughness. By defining the crater area as test mask and the surrounding unmodified area as reference mask, two volume fractions can be delimited: the volume below the reference surface defined as volume down (V_{down}) and the volume above the reference surface defined as volume up (V_{up}) (Figure 3.4b). Volume down and volume up correspond to the volume of the crater depression and the crater rim, respectively, and provide an estimation of the volume of material displaced during crater formation. The difference between V_{down} and V_{up} is the actual volume of material lost due to particle ejection or vaporization [121].

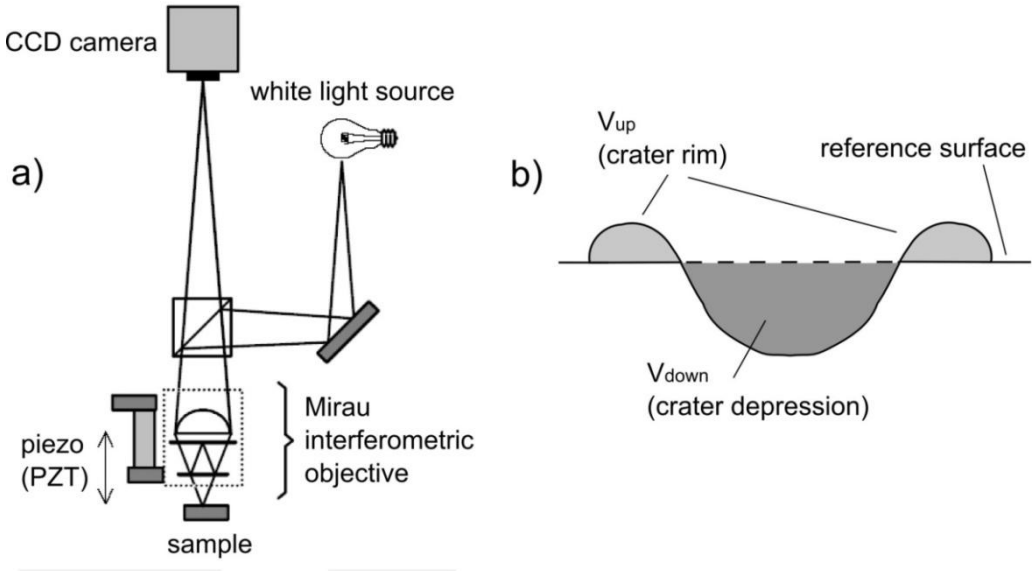

Figure 3.4 a) Representation of the optical system of a white light interferometer with a Mirau objective lens. b) Determination of the crater rim (V_{up}) and crater depression (V_{down}) volumes.

3.3.2 FIB/SEM Dual Beam Techniques

Site specific microstructure and chemical characterization of ignition discharge craters and eroded surfaces were carried out using a FEI Strata DB 235 FIB/SEM dual beam workstation.

3.3.2.1 Dual Beam System

The FIB/SEM dual beam incorporates both a focused ion beam (FIB) column and a field emission scanning electron microscope (SEM) column in a single system. The FIB instrument is very similar to a SEM and consists of a liquid metal ion source (Ga^+) and an ion column made up of lenses and apertures. The ion source is operated at an emission current of 2.2 µA. Typical accelerating voltages range from 5 to 30 kV. A set of apertures of various diameters permits to set the ion beam current from a few pA to 20 nA. Low ion currents are generally used for imaging or fine polishing of cross sections, whereas large ion currents are employed for the milling of large domains.

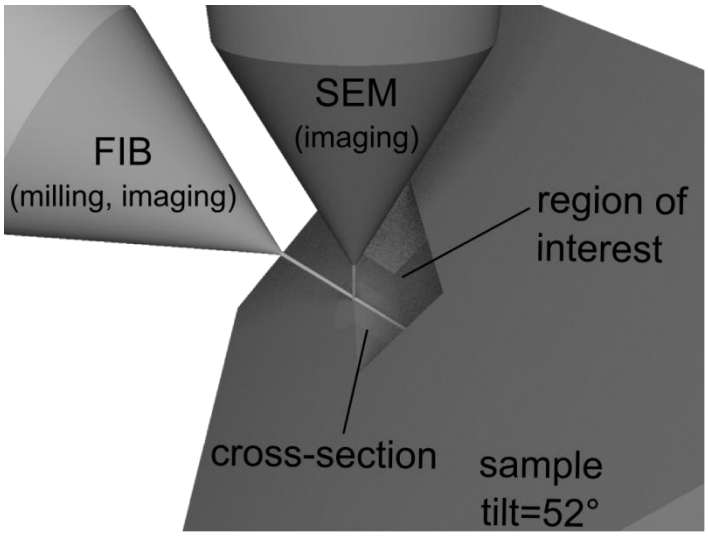

Figure 3.5 Geometrical configuration of the dual beam. The sample is tilted at 52° for milling operations so that the sample surface is normal to the ion beam. The electron and ion beams coincide, which simultaneously enables both precise ion milling of the region of interest and high resolution electron imaging of the cross section.

The configuration of the system employed is a vertical electron column with an ion column tilted at 52° from the vertical (Figure 3.5). To enable ion milling and electron imaging of the same region, the dual beams have a coincident point where the two beams intersect with the region of interest on the sample. This position is achieved when the sample is set on the “eucentric” height, i.e., for the system used, when the distance between the sample surface

and the electron lens is 5 mm. The advantage of this configuration is that sample tilt is not required between milling and imaging steps, resulting in less time-consuming operations and enhanced precision. A large overview of FIB/SEM systems and their applications can be found in the books of Giannuzzi and Stevie [122] and Orloff *et al.* [123].

3.3.2.2 Site Specific Cross-Sectioning

The sample is tilted to 52° from the horizontal so that the sample surface is perpendicular to the ion beam, and set at the eucentric height (Figure 3.6a). A band of Pt is deposited in-situ over the region of interest (e.g. the center of the crater) by ion beam induced deposition (IBID) via the decomposition of a Pt precursor gas (Figure 3.6b). The Pt band protects the surface against ion beam damaging during the following milling steps, provides a sharp cross section edge and helps in reducing the so-called curtaining effect (development of stripes on the surface of the cross section [122]). A large trench is first milled with a high ion beam current of 20 nA (Figure 3.6c). The cross section is further polished in two or three steps with decreasing ion beam currents from 7000 pA to 1000 pA, until a sufficiently smooth surface for imaging is achieved (Figure 3.6d).

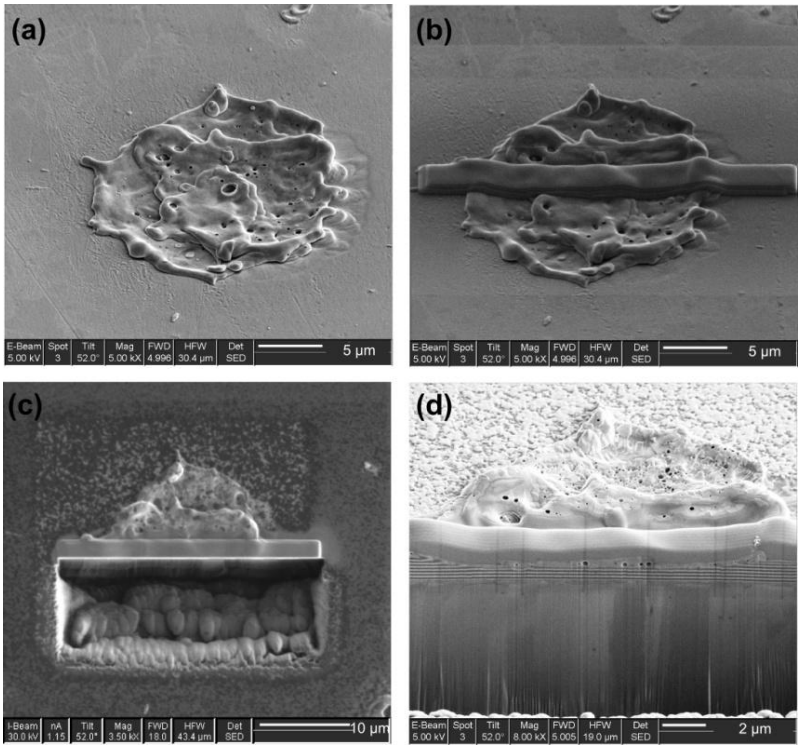

Figure 3.6 FIB cross-sectioning steps for a crater. (a) The sample is tilted and positioned at the eucentric height. (b) Deposition of a protective Pt band. (c) Ion milling and polishing (ion view). (d) Polished crater cross section ready for SEM imaging.

3.3.2.3 TEM foil preparation and STEM/TEM investigation

In order to prepare a TEM foil, two trenches are milled on both sides of the region of interest. The specimen is thinned down to 1 µm with gradually reducing ion beam currents. After reaching this thickness, the sample is back-tilted to 7° and the foil is partially cut free with a U-shaped pattern, still connected to the substrate via two thin branches at the top. For in-situ lift-out, a "Kleindiek MM3A" micromanipulator is inserted into the chamber. The tip of the micromanipulator is slowly lowered until it contacts the specimen. The specimen and the tip are welded by Pt deposition using the electron beam. When specimen and tip are fixed together, the specimen is cut free from the substrate. The specimen, now only fixed to the tip of the micromanipulator, is lifted out and moved to a pre-cut Cu TEM grid where it is fixed again by Pt deposition. Once fixed on the Cu grid, the specimen is finally thinned with ions down to a thickness of approximately 100 nm.

A STEM detector (Scanning Transmission Electron Microscopy) in the dual beam workstation permits a first observation of the TEM foil in bright and dark field with accelerating voltages <30 kV. Further TEM investigations are carried out with a JEOL 200 CX instrument at an operating voltage of 200 kV. Imaging of the microstructure, selected area diffraction and EDX analysis (Oxford Isis system) can be performed.

CHAPTER 4

Ignition Discharge Mode Analysis

In this chapter, a quantitative analysis of the arc and glow modes composing the ignition discharge is preformed. The goal is to understand how parameters such as pressure, cathode material and atmosphere can modify the behavior of the discharge. In a first part, a brief description of typical voltage-time curves is made and different measurement methods able to analyze these curves are evaluated with respect to their reliability and convenience. Results of arc fraction measurements are presented in a second part for four different cathode materials (Ag, Cu, Ni, Pt) and for discharges produced in air and nitrogen at external pressures ranging from 1 to 10 bar. Reaction of the sparked surface under certain conditions and influence of pressure, cathode material and atmosphere on the discharge characteristic are discussed. A summary of the more important results is proposed at the end of this chapter.

4.1 Determination of the Arc and Glow Phase Fractions

4.1.1 Introduction

The electrical discharges occurring in technical application fields can be classified either as arc or glow discharges. Arc discharges take place in arc vacuum interrupters, circuit breakers, arc welding and electro discharge machining, while glow discharges are used, amongst others, for the treatment of surfaces in the microelectronic industry (cleaning, etching, deposition) or in spectroscopy analysis. The ignition discharge has the particularity to possess both types of discharges, which differ by two different electron emission mechanisms from the cathode (section 2.1.3). The transition from arc to glow mode is characterized by an abrupt rise in the voltage of ~200 V, which corresponds approximately to the difference in the cathode fall voltage between arc and glow. This permits the identification of the different modes by means of the voltage-time curve registered with the oscilloscope (Figure 3.3). Because of the stochastic nature of the ignition discharge, numerous discharges must be collected and analyzed for a reliable determination of the arc and glow fractions for a given electrode material, gas and pressure conditions. However, the numerous arc-to-glow and glow-to-arc transitions, oscillations and irregularities present in the voltage-time curve render

this task non trivial. Figure 4.1 shows four voltage-time curves collected under the same conditions and presenting different behaviors. In Figure 4.1a the arc-to-glow transition is characterized by a unique voltage drop at t=500 µs and both arc and glow phases can be clearly distinguished. In Figure 4.1b the first transition occurs approximately at t=400 µs but multiple transitions take place during ~200 µs and the stable glow mode is finally achieved after 600 µs. In Figure 4.1c the transitions occur during a period of time of more than 1 ms. Finally, in Figure 4.1d, the curve is almost exclusively composed of transitions between the two modes and the determination of arc and glow fractions is difficult. A method able to analyze quantitatively such voltage-time curves is needed.

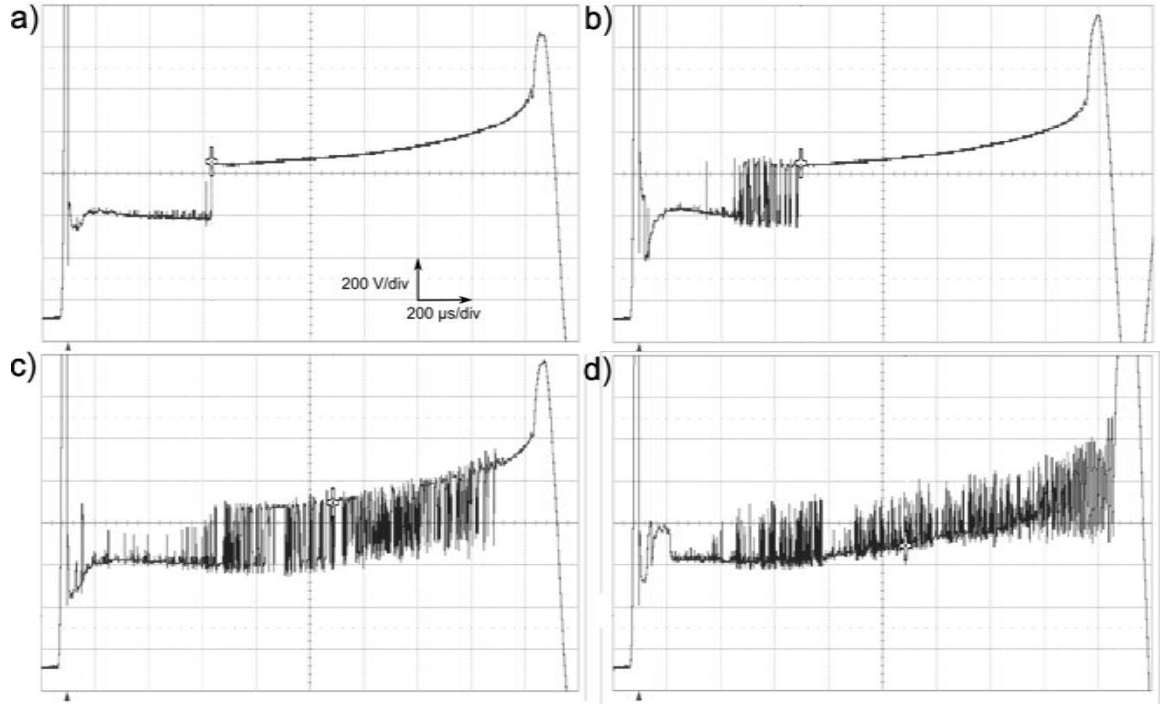

Figure 4.1 Four voltage-time curves registered in the same conditions and presenting different behaviors.

4.1.2 Measurement Methods

4.1.2.1 Time at Level Function

The oscilloscope possesses numerous functions permitting an automatic analysis of registered curves. The function "time@level" gives the time associated to a defined voltage level and is, for our task, particularly interesting. By choosing an appropriate voltage level situated between the arc and glow voltages (e.g. 500 V), this function will give the time at which the first transition occurs. The same function permits to determine total discharge duration by measuring the time between breakdown (t=0) and the rightmost voltage rise

associated with the extinction of the discharge. The ratio of the first transition time to the discharge duration gives the fraction of arc. This method works very well for discharge curves like in Figure 4.1a where only one arc-to-glow transition takes place. However, in cases like in Figures 4.1b-d, the "time@level" function will detect the first transition but it will not be able to consider the following changes, leading to an underestimation of the arc fraction. Moreover, this method requires setting a unique voltage value for the arc-to-glow transition. Because the arc and glow voltages slightly increase with time during the discharge, the transition voltage varies depending on whether the change of mode occurs at the beginning or at the end of the discharge. For these reasons, the "time@level" function proved not to be suitable for the precise determination of the arc and glow fractions of ignition discharges.

4.1.2.2 Eye Inspection

A straightforward method consists in visually analyzing the discharges. As opposed to the "time@level" function, the inspector is able to consider the oscillations of the curve and can estimate the more appropriate time for the arc-to-glow transition. However, this method suffers two major drawbacks. First, eye inspection is very time consuming, which limits the number of discharges examined and reduces the statistical significance of the measurement. Secondly, the method implies a large part of subjectivity from the inspector, resulting in no reliable results.

4.1.2.3 Persistence Method

The persistence method is based on a special function of the oscilloscope called "Analog Persistence". This function establishes a color-coded frequency view of the voltage-curve of numerous discharges. Figure 4.2 shows the persistence view of 1, 10, 100 and 500 cumulative discharges. Highly repetitive points in the voltage-time curves appear red while rarely repetitive points are purple. As the arc and glow phases are characterized by defined voltage levels, two red branches appear in the persistence view when the number of discharges increases, revealing a kind of mean voltage-time curve.

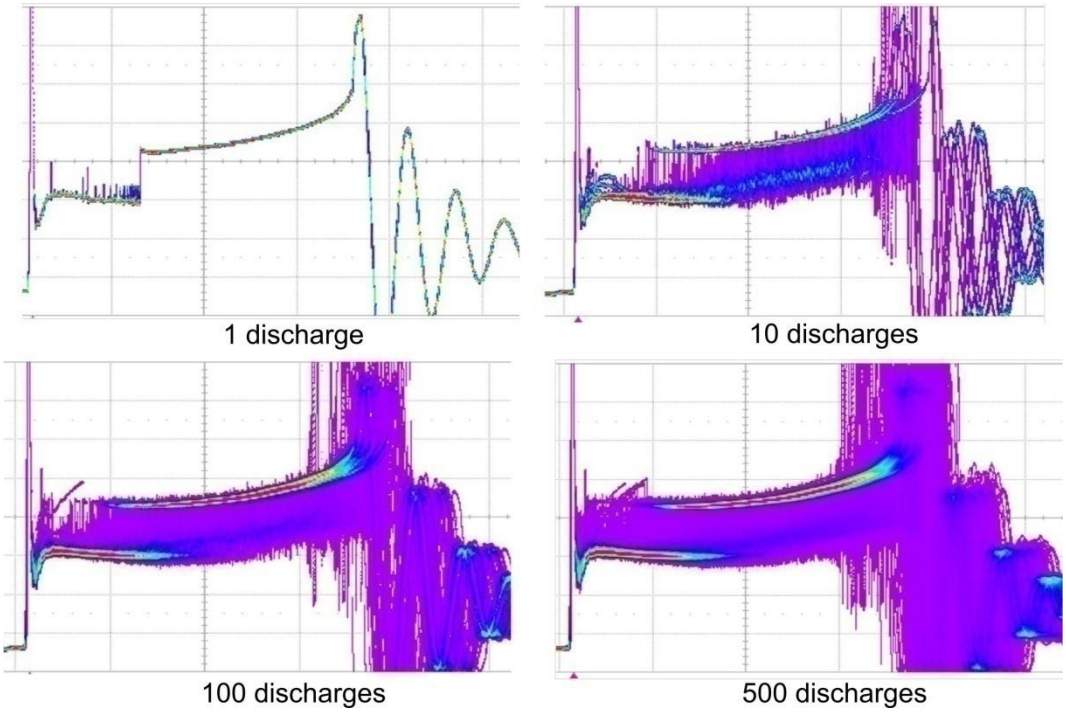

Figure 4.2 Persistence views of 1, 10, 100 and 500 cumulative discharges revealing the mean arc and glow phases (red branches).

The persistence curve provides a proper visualization of numerous cumulative discharges but it does not permit to determine the arc and glow fractions. To analyze the outcome of the persistence curve, an additional function package called “Jitter and Timing Analysis Package” (JTA2) including the function “persistence histogram” is needed. Persistence histogram provides a frequency vs. voltage histogram of the persistence curve in a defined voltage range. In Figure 4.3, the histogram of a voltage-time persistence curve is shown. Two peaks corresponding to the points at the arc and glow voltages can be clearly distinguished. Since the burning voltage of each mode is not constant during the whole discharge, the peaks, especially that of the glow, are not discrete but have a certain broadness. The number of points is counted in defined voltage intervals using the function “total population”. The ratio between the population of the arc (voltage range V_a to V_b) and the total population (voltage range V_a to V_c) gives the arc fraction.

Contrary to the “time@level” and “eye inspection” methods, the persistence method does not determine the time when the arc-to-glow transition occurs but rather analyzes the voltage-time curve on the basis of the characteristic arc and glow voltage levels. This method permits a reliable and precise determination of the arc fraction value of many discharges, regardless of the presence of transitions and irregularities in the curves.

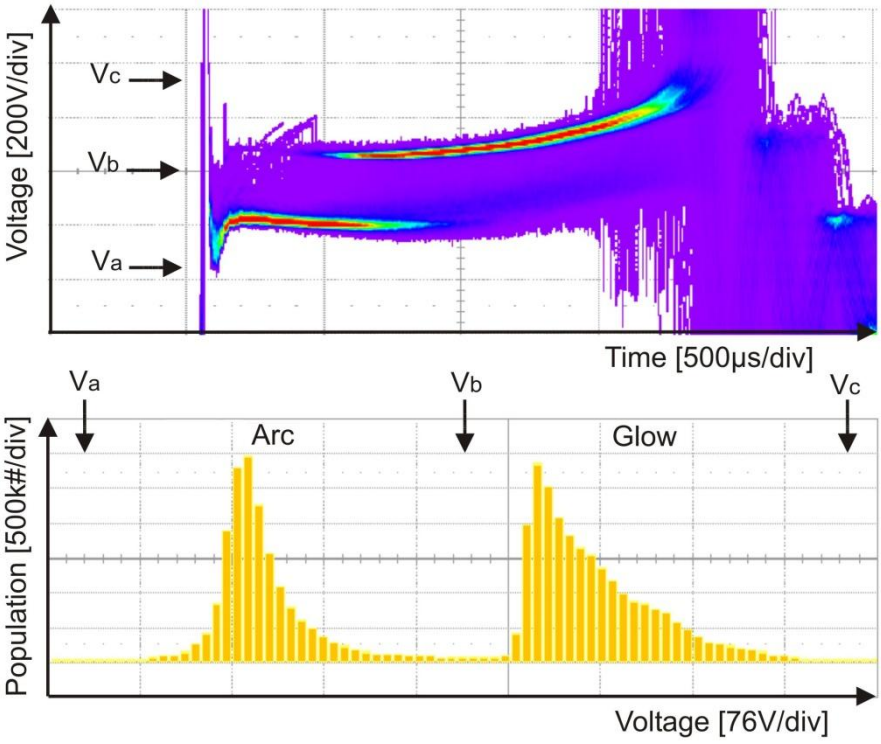

Figure 4.3 Persistence view of 500 discharges (top) and its corresponding frequency histogram (down) showing the distribution of the points of the voltage-time curves as a function of the voltage. By integrating the persistence histogram between the corresponding voltage levels, the arc and glow fractions can be precisely determined.

4.2 Results and Discussion

4.2.1 Arc Fraction Results

The arc fraction is determined for Ag, Cu, Ni and Pt electrodes at room temperature, in synthetic air and nitrogen for pressures ranging from 1 to 10 bar (absolute). For a given electrode material, a first set of measurements is performed in air by a stepwise increase of the pressure from 1 to 10 bar. For each pressure step, 500 discharges are collected and analyzed. After this, a second set of measurements is performed but this time under nitrogen. The procedure is repeated six times alternating the atmosphere (three times under air, three times under nitrogen). The discharges are produced at the lowest spark frequency achievable with our ignition system of 10 Hz. The low frequency aims to minimize electrode heating caused by spark repetition.

Figure 4.4 shows the arc fraction as a function of the pressure for Ag, Cu, Ni and Pt electrodes in air and nitrogen. Each point is the mean value of three measurements (3×500

discharges) while the scatter bar represents the standard deviation. For all electrodes under both air and nitrogen atmospheres, the arc fraction always increases with the pressure. However, the pressure at which the arc phase occurs and the maximal arc fraction reached at high pressure strongly depend on the electrode material and the atmosphere. For the Ag cathode in air, the arc fraction is already significant at 2 bar and grows rapidly to reach 70 % at 10 bar. In nitrogen, the arc phase first appears at a pressure of 5 bar and reaches 40 % at 10 bar. For the Cu cathode, the arc phase first increases at a pressure of 5 bar and reaches 55 % and 22 % at high pressure in nitrogen and air, respectively. In the case of Ni, the arc fraction becomes significant at 6 bar and amounts to 23 % and 8 % at 10 bar. Finally, the Pt cathode shows the lower arc fraction values with 5 % in air and 11 % in nitrogen. It is also interesting to note that the discharges at high pressures present more arc fraction in nitrogen than in air, except for Ag which shows the opposite behavior.

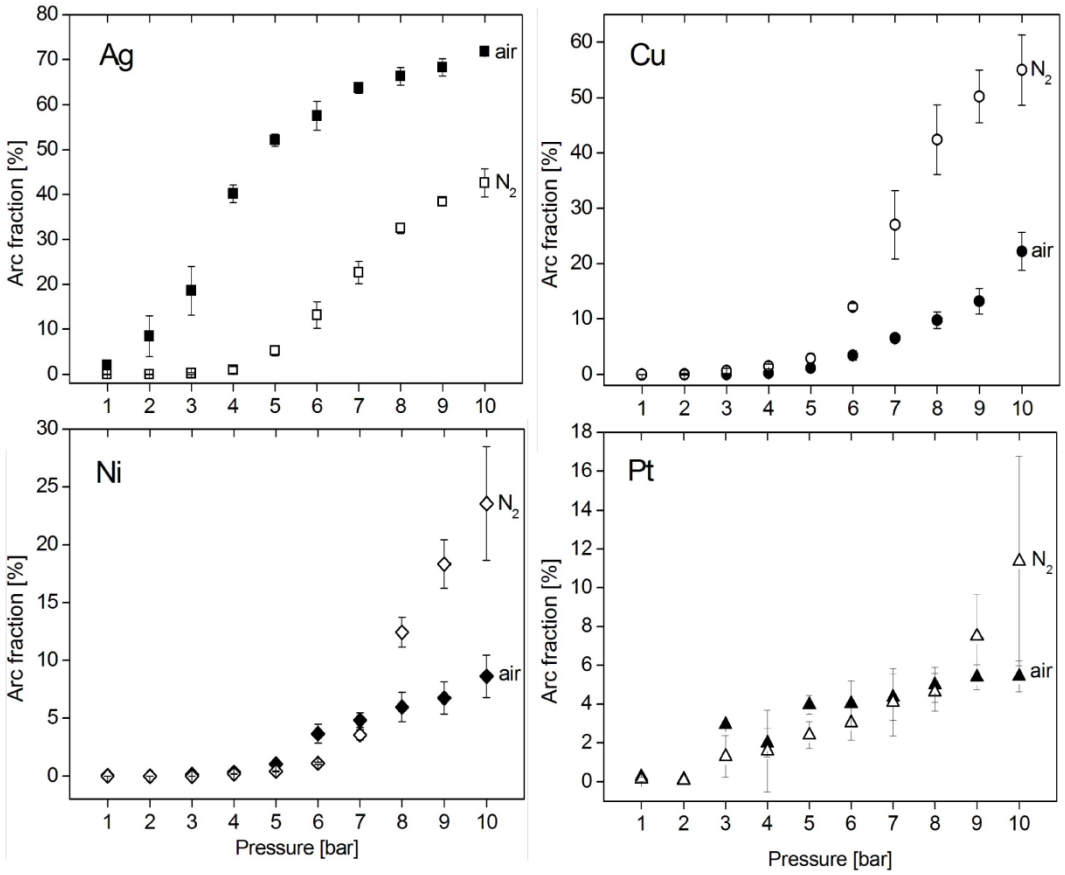

Figure 4.4 Arc fraction as a function of the pressure for Ag, Cu, Ni and Pt electrodes in air and nitrogen.

4.2.2 Plasma-Assisted Oxidation of Ag Cathode in Air

4.2.2.1 Surface Characterization

For Cu, Ni and Pt cathodes, the sparked area of the cathode surface is covered by numerous craters and no obvious difference is observed between air and nitrogen. In the case of Ag, however, two different morphologies are obtained on the surface, depending on whether the discharges are produced in air or nitrogen. Figure 4.5 shows the surface of a Ag electrode after approximately 1000 discharges produced in nitrogen (left) and in air (right) at 7 bar. Similar to the others metals, the sparked area of Ag in nitrogen is covered by small craters and the repetition of the spark produces nothing more than the superposition of craters with diameters varying from 2 to 10 µm. In air, however, craters cannot be observed and the sparked area is covered with a dark layer which is partially stripped off in some regions.

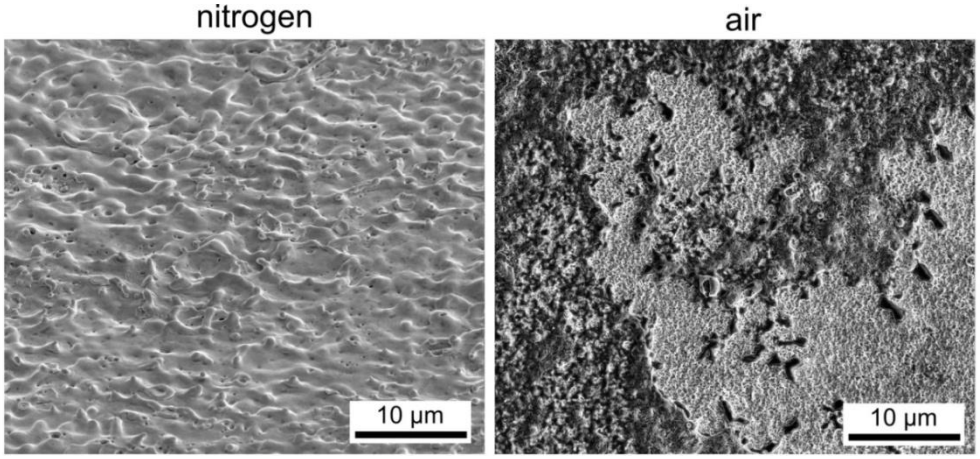

Figure 4.5 SEM images of the sparked area of a Ag cathode after 1000 discharges at 7 bar in nitrogen (left) and air (right).

Figure 4.6 shows the secondary electron image (SE) and the corresponding O and Ag element mapping (EDX) of the surface after 1000 discharges in air. This mapping indicates clearly that the dark layer contains more oxygen than the regions where the layer is stripped off. Therefore, it suggests that an oxide layer grows on the surface of the Ag cathode during the sparks. Two oxides, Ag_2O and AgO, can form upon the oxidation of silver. The sparked region of the surface exhibits a brownish color which is generally associated with Ag_2O, while the dark gray color is associated with AgO [124, 125]. Furthermore, AgO is an unstable oxide which decomposes into Ag_2O over 100°C. Therefore, it is likely that Ag_2O rather than AgO forms on the surface.

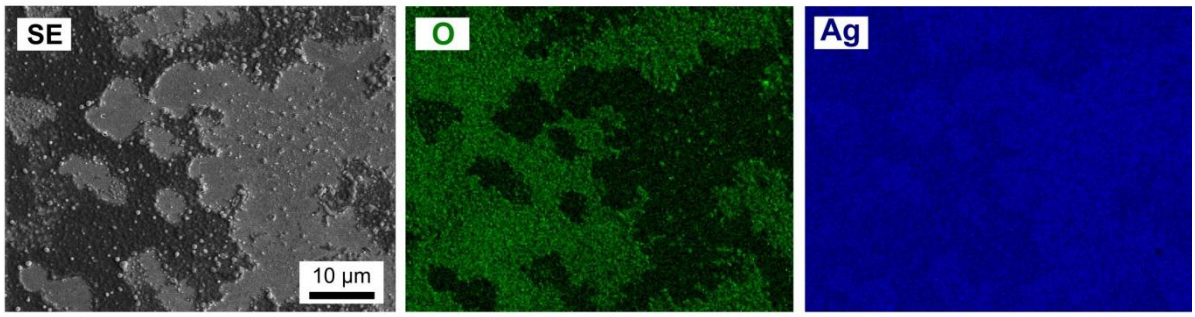

Figure 4.6 Element mapping (EDX) of the sparked area of Ag after 1000 discharges in air at 7 bar. The dark layer corresponds exactly to the regions where O is detected, indicating that an oxide film grows at the surface during sparking.

The stripped areas consist of several eroded circular areas having a size in the range of 5-10 µm which corresponds well to the size of arc cathode roots. This can be seen clearly in the SE image of Figure 4.6 as well as in Figure 4.7a-b. Therefore, it is very likely that the damage of the oxide film is caused by the displacement of the arc cathode root at the surface. The step between the stripped area and the oxide layer measured at the border of the sparked zone was found to be ~400 nm (Figure 4.7c). This value approximately indicates the thickness of the oxide film grown during the 1000 discharges produced at 7 bar. The surface of the sparked area is also covered with numerous molten oxide particles that have been ejected. The size of these particles is in the range of 1-2 µm.

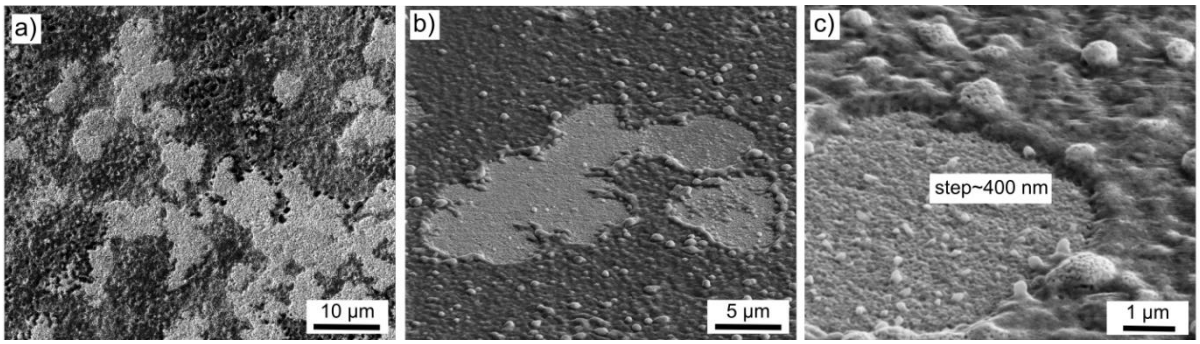

Figure 4.7 SEM images of stripped areas observed on Ag (1000 discharges, air, 7 bar). a-b) The stripped areas consist of several circular spots each having a diameter in the range of 5-10 µm. c) The step between the stripped area and the surrounding film was found to be ~400 nm.

4.2.2.2 Oxidation and Erosion Mechanisms

Ag is not oxidized by O_2 at ambient or slightly elevated temperatures and pressures. Instead O_2 is adsorbed dissociatively to form surface and bulk dissolved O atoms [126]. The dissociative adsorption of O_2 is not sufficient to cause oxidation. However, it is well known that ozone (O_3) and dissociated or ionized species in oxygen plasma are of a highly oxidizing

nature [127]. Both O_3 and oxygen plasma (O, O^+) are currently used as powerful reagent for the synthesis of metastable silver oxides (Ag_2O, AgO) [126, 128]. The glow plasma of the ignition discharge in air contains highly reactive species like O^+. Therefore, under the repetition of the sparks, a silver oxide film can grow on the cathode surface. The oxide film does not grow over the whole cathode area (∅ 3 mm) but is limited to an area which corresponds to the place occupied by the glow plasma (~∅ 1 mm). Therefore, it is clear that the formation of the oxide film is not due to any temperature elevation at the surface but rather to the glow discharge plasma. The brownish color of the oxidized area, the low thermal stability of AgO and the fact that Ag oxidized preferentially to Ag_2O in oxygen microwave plasma [128] suggest that Ag_2O is formed rather than AgO. Step size measurements between stripped areas and the growth film at the edge of the sparked zone permit to estimate that the repetition of 1000 discharges can produce an oxide film with a thickness on the order of 400 nm.

The arcing of clean metallic surfaces causes the formation of craters with molten rims, as observed for Ag in nitrogen and for the other metals. This is also the case when the oxide film is very thin (5-10 nm) [94, 111]. However, when a thick oxide film is present on the surface, the arc erosion processes differ completely. Hitchcock and Guile [113] investigated the arc erosion of pre-oxidized Cu cathodes. For oxide thicknesses of 25 nm or greater, they found that the damage caused by the arc was not a crater but an area stripped of oxide. The stripped areas produced by 4.5 and 40 A arcs on Cu cathodes covered with 225 and 275 nm oxide films that they observed, present great similarities with the stripped areas on Ag cathodes sparked in air observed in this work. In both cases, melting of the underlying metal in the stripped area does not occur, the stripped areas have a circular shape, and ejected molten oxide globules are observed. These similarities confirm that the stripped oxide areas observed in air are caused by the arc phase of the ignition discharge. Furthermore, semi-quantitative observations of the sparked regions produced at different pressures indicate that the total stripped area increases when the pressure and the arc fraction are greater.

The emission of electrons from cathodes coated with a thick oxide film is expected to occur via the formation of multiple conducting filaments through the oxide film [129]. This so-called electroforming process was found to occur in electric fields across the film between 10^7 and 10^8 V/m [130]. Filament currents are about 10 mA and the filament lifetimes are in the range of 1 to 100 ns [113]. Because of the high electrical resistivity of oxides compared to metals, Joule heating becomes predominant, resulting in the rapid melting of the filament [114] and the explosive ejection of molten oxide particles. The low thermal stability of Ag_2O

(450-500°C [131]) promotes the melting and ejection process which explains the high density of ejected molten particles observed at the surface. Electroformed filaments through oxide films are known to be efficient thermionic emitters and a number of theories have been proposed for the emission mechanism [129]. As the current in the filament rapidly rises to a value at which joule heating causes the filament to be ruptured, material is ejected and a new emission site is found. The arc prefers to run over places where electron emission is easiest. Therefore, instead of forming craters as in non-oxidized cathodes, the arc will run over the oxidized surface, leaving a path of adjacent circular stripped areas. This explains the fact that no craters are observed on the surface as well as the large arc fraction measured in discharges produced in air.

The erosion associated with the stripping mode is expected to be almost equal to the volume of the stripped regions left by the arc [111, 132] and results in the ejection of globular oxide particles. Even if the arc phase causes the destruction of the oxide film, the erosion rate is actually determined by the thickness of film grown on the surface during the glow phase of the discharge. As a relatively thick oxide layer (~400 nm) is observed after only 1000 discharges, an important erosion rate can be expected. This is consistent with the great electrode wear value of 40 μm^3/spark reported for Ag electrodes tested in air at low temperature [24]. As Ag_2O is not stable at high temperatures, it is likely that this erosion model based on the plasma-assisted oxidation of Ag and the stripping of the oxide film, does not occur in engines.

4.2.3 The Arc to Glow Transition

The presence of two phases during the inductive part of the ignition discharge can be seen as a competition between arc and glow modes, both associated with different electron emission mechanisms at the cathode surface. The discharge will always adopt the more appropriate and effective mode to permit the current to flow. Therefore, it is clear that the current value plays a decisive role in the mode taken by the discharge. Conventional voltage-current characteristics, like that shown in Figure 2.6, predict the arc-to-glow transition to take place at a current of ~1 A. However, others parameters like the pressure, the gas and the cathode material can affect this transition current value.

4.2.3.1 Influence of the Pressure

Arc fraction results displayed in Figure 4.4 clearly indicate that the arc fraction grows when the pressure increases, regardless of the electrode material and the gas used (air or nitrogen). The current of the ignition discharge, at least for its inductive part, is determined by the coil and is independent of the external pressure at which the sparks are produced. This means that the arc-to-glow transition current must change when the pressure is varied. Figure 4.8 shows the mean transition current calculated on the basis of the arc fraction results and considering that the discharge current decreases linearly with time from its initial value of 100 mA set by the coil to zero. As the pressure increases, the arc-to-glow transition current decreases and the arc phase can thus last for longer times. This effect is particularly obvious in nitrogen, while in air, the low arc fraction values for Ni and Pt (<10 %) do not permit a reliable determination of the transition current. Because of its singular behavior discussed previously, the transition current in the case of Ag in air is not shown.

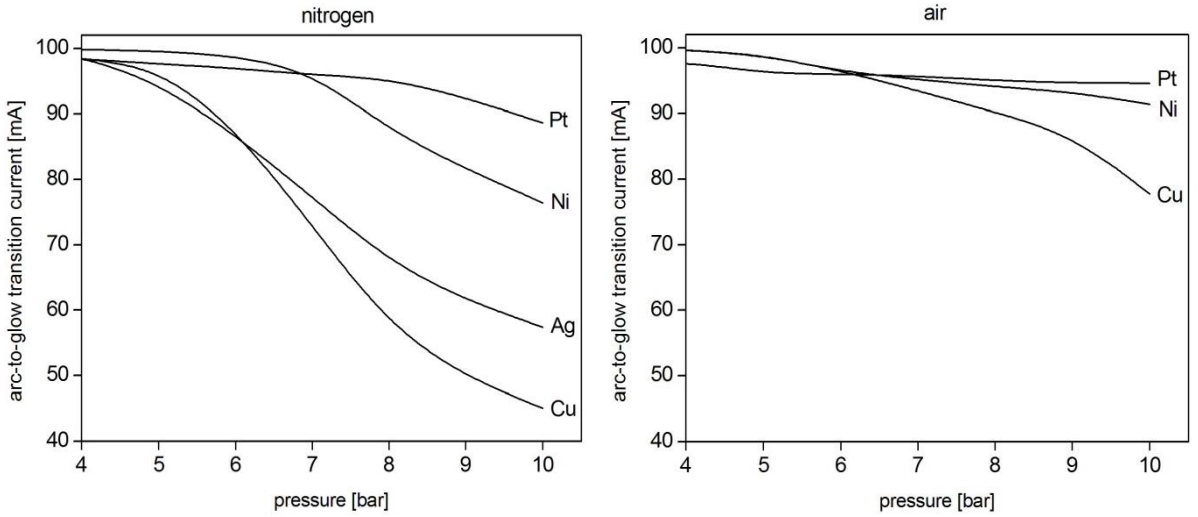

Figure 4.8 Mean arc-to-glow transition current as a function of the external pressure in nitrogen (left) and air (right) for Ag, Cu, Ni and Pt electrodes.

The influence of the pressure on the arc-to-glow current transition can be discussed on the basis of the large difference of current density associated with each mode. Indeed, the arc phase is characterized by current densities on the order of 10^8-10^9 A/m^2 corresponding to arc cathode roots of 1-10 µm which are visible *post-mortem* as craters. The current density at the cathode of the glow discharge is 4-5 orders of magnitude lower with values around 10^4-10^5 A/m^2. As a consequence, the arc-to-glow transition is accompanied by a great expansion of the cathode root from some µm to some 100 µm. As the discharge current decreases with time, the cathode root of the arc is able to contract in order to maintain a sufficiently high

current density to fulfill the conditions of temperature and electric field at the surface necessary for thermo-field emission of electrons. However, as the current becomes too low, the secondary emission of electrons becomes more efficient than the thermo-field emission and the discharge transforms into a glow. When the discharge is produced at low pressure, i.e. 1 bar, the glow plasma can expand in order to occupy a large cross-sectional area and reach a sufficiently low current density. The glow discharge is then said to be *normal*, that is, the cross-sectional area of the discharge near the cathode is proportional to the current, while the current density remains constant.

At high pressure, the higher species density in the gas permits the arc to contract and to maintain the required high current density even with low current values. As a consequence, the current at which the discharge transforms from an arc into a glow is lower and the arc can burn longer. This explains why the arc fraction and the time of the first arc-to-glow transition increase when the pressure increases. However, as the discharge tries to adopt a glow form, its free expansion is limited by the ambient pressure, increasing the current density at the cathode surface. When the current density is too high (10^5-10^6 A/m^2), the glow discharge is said to be *abnormal* (section FG of the voltage-current characteristic in Figure 2.6). Such abnormal glows are usually obtained when the entire cathode has been covered with the discharge, so that any further increase of the current inevitably increases the current density. In our case, the cathode exhibits sufficient area (∅ 3 mm) but the high ambient pressure reduces the effective area that can be occupied by the discharge. The high current density of the abnormal glow discharge also results in the intense heating of the cathode leading to the transition back to the arc mode. This happens locally at places where the electric field is higher or the work function is lower (pins, scratches, impurities, etc). The development of instabilities and the transition back to the arc mode occur when a current density threshold is reached. As the current density increases with the square of the pressure [27], the current at which this threshold is reached decreases rapidly when the pressure increases, leading to higher arc fractions at high pressure. Since the transitions take place over a certain current range, many changes between the arc and glow modes occur as it is observed in the voltage-time curves (Figure 4.1b-c). As the current further decreases, the discharge always ends up taking a glow form.

4.2.3.2 Influence of Gas and Material

The results show that the material and the gas also influence the behavior of the discharge. The basic operating mechanisms in the hot spot of the arc discharge are assumed to be the same in vacuum and in gas [61-63]. Therefore, it is unlikely that the nature of the

ambient gas (air or nitrogen) strongly affects the behavior of the arc phase. During the glow discharge, however, the species bombarding the cathode surface (ions, radical, and molecules) come exclusively from the gas. Thus, the glow phase is expected to be more influenced by the gas than the arc phase. Results show that the arc fraction at high pressures is lower in air than in nitrogen, except for Ag which exhibits strong oxidation of the surface. The cathode fall voltages of a normal glow discharge with Cu, Ni and Pt are 370 V, 226 V and 277 V in air and 208 V, 197 V and 216 V in nitrogen, respectively [133, 134]. As the cathode fall voltages are higher in air than in nitrogen, the accelerated ions can reach higher kinetic energies and secondary electron emission yield at the surface is increased. Higher current densities can thus be sustained, which promotes the glow mode and shifts the arc-to-glow transition to higher current values. In addition, it is also possible that a thin oxide film (~nm) is formed when sparking in air, which increases the secondary electron emission yield of the surface. Finally, the nature of the gas can have an impact on electronic and thermal instability phenomena occurring in the plasma of the glow discharge [27].

The influence of the material on the ignition discharge characteristic is complicated since it can affect both the arc and glow phases composing the ignition discharge. In the case of the arc discharge, thermal properties such as the melting and boiling points are relevant while in the case of the glow discharge, the secondary emission coefficient of the surface is important. Nevertheless, the results show that a lower melting (or boiling) point seems to have a positive influence on the existence of the arc phase. In nitrogen, materials with low melting point like Ag and Cu (961°C and 1084°C, respectively) show higher arc fractions at high pressure (40-50 %) than materials with a higher melting point like Ni and Pt (1455°C and 1768°C, respectively) with arc fraction values lower than 20 %. The lower the melting and boiling points, the more easily the conditions of high temperature and high electric field required for thermo-field emission are fulfilled. However, it is important to keep in mind that the complexity of the cathode spot processes may probably involve other properties related to electron emission and vaporization of the cathode material. A better understanding of the influence of the material on the discharge mode characteristic would require investigating more metals in a controlled atmosphere preventing any oxidation phenomena.

4.3 Summary

Contrary to most electrical discharges occurring in technical applications, the ignition discharge is composed of two different phases: the arc and the glow discharges. As each mode is associated with a specific burning voltage, the occurrence of these phases can be recognized on the voltage-time characteristics registered by means of the oscilloscope. However, a quantitative and reliable analysis of the discharge mode is not straightforward due to the numerous transitions and irregularities occurring in the voltage-time curve. A method based on the cumulative persistence measurement of numerous discharges is developed in order to achieve this task. Using this method, the arc fraction of ignition discharges produced on Ag, Cu, Ni, and Pt cathodes is investigated as a function of the pressure in air and nitrogen. The results show that parameters like the pressure, the gas and the cathode material can influence the discharge modes.

The Ag cathode sparked in air presents a singular behavior due to the strong oxidation of its surface. The oxidation and erosion process of Ag results from the combined action of both the arc and glow phases. The reactive oxygen species present in the glow plasma such as O and O^+, and the repetition of the sparks leads to the formation of a metastable Ag_2O thick oxide film on the surface (Figure 4.9a). Electron emission occurs via current-carrying filaments formed through the oxide (Figure 4.9b). As these filaments become molten as a result of Joule heating, molten oxide particles are explosively ejected from the surface (Figure 4.9c). The arc cathode root then moves to a new emitting site where this process is repeated, leaving circular areas stripped of oxide on the surface. The efficient electron emission of the current filaments formed through the oxide film and the oxide decomposition promote the arc mode, resulting in ignition discharges exhibiting high arc fractions. The erosion associated with the stripping mode is equal to the volume of stripped oxide and is expected to be much higher than when craters with molten rims are formed on metallic surfaces. The erosion rate is mainly determined by the large-scale oxidation taking place at the surface during the glow phase of the discharge.

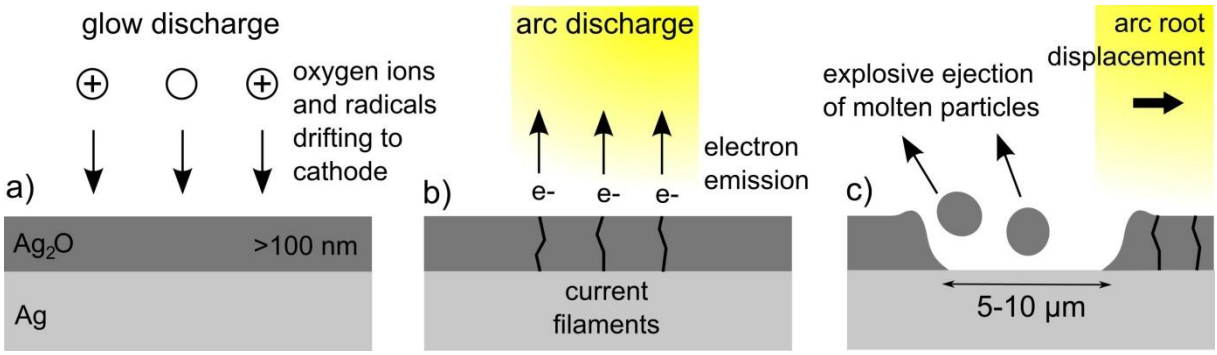

Figure 4.9 Schematic representation of the oxidation-erosion process at the surface of Ag cathodes sparked in air. a) Oxidation of the surface in the highly reactive plasma of the glow discharge. b) Formation of current-carrying filaments through the film at the arc cathode root. c) Explosive rupture of the filaments leaving oxide stripped areas and displacement of the arc root to a new emitting site.

The external pressure at which the discharges are produced has a large influence on the spark behavior. The fraction of arc always grows when the pressure is increased, irrespective of the cathode material and the nature of the gas (air or nitrogen). As the current of the inductive part of the discharge is independent of the external pressure, this effect can only be attributed to a decrease of the mean arc-to-glow transition current with the pressure (Figure 4.8). The transition from the arc to the glow mode is associated with a reduction of the cathode current density by many orders of magnitude, resulting in a great expansion of the discharge cathode root. At low pressure, the glow discharge plasma can expand and occupy enough area of the cathode, so that currents on the order of 100 mA can be sustained by the glow. In these conditions, the discharge adopts the glow form almost immediately after the breakdown. As the ambient pressure is increased, the arc cathode root can contract, which shifts the arc-to-glow transition to lower current values and enhances the fraction of arc in the discharge. Moreover, as the current becomes too low and the discharge tries to adopt a glow form, the surrounding high pressure confines the glow plasma and raises the current density at the cathode surface (abnormal glow discharge). This leads to instabilities and several transitions between the glow and arc modes occur. These transitions can be unambiguously recognized in the voltage-time curve of the discharges as shown in Figure 4.1b-d. In summary, the higher arc fraction at high pressures is a result of both the enhanced stability of the arc phase which leads to a later first arc-to-glow transition, and the instability of the glow phase which leads to numerous transitions back to the arc.

Discharges produced in nitrogen show higher arc fractions than discharges produced in air, except for silver where a thick oxide layer is formed on the surface. The higher glow

cathode fall voltages in air compared to nitrogen, which may promote secondary electron emission from the cathode, are a possible explanation for this effect. However, instabilities occurring in the glow discharge plasma itself cannot be excluded to explain the difference between both atmospheres. Finally, even if a proper relationship between the arc fraction and one or more material properties could not be found, the results show that materials with low melting/boiling point like Ag and Cu tend to exhibit higher arc fractions than materials with higher melting/boiling point like Ni and Pt.

CHAPTER 5

Microstructure Characterization of Craters

This chapter will focus on the microstructure characterization of craters created on the surface of cathodes by single ignition discharges. The goal of this study is to gain information about the crater formation process through the precise observation and analysis of the microstructure at and below the surface. In the first part, a non exhaustive review is presented of different studies dealing with the analysis of electrical discharge craters. In the second part, cross sections are performed in craters by means of focused ion beam (FIB). For monitoring the depth of the modification, a solution consisting in the production of craters in multilayered electrodes is introduced. Observations of cross sections are presented for craters on Ag/Ni, Ni/Cu and Pt/Ni multilayered surfaces and the different regions observed below the surface are discussed. Finally, the morphology and microstructure of craters in Pt/Ni electrodes are investigated for discharges produced at different external pressures ranging between 1 and 10 bar. For this analysis, FIB cross-sectioning, FIB tomography and EBSD are applied. For the first time, the volume of the crater molten pool is experimentally determined and the re-solidification microstructure is observed. These results are analyzed with regard to the different discharge phases, and crater formation mechanisms are discussed.

5.1 State of The Art

Since in-situ investigations of cathode spots are very difficult, many authors have performed *postmortem* studies of the craters produced by discharges on the cathode surface. Craters are the trace left by cathode spots on the surface and show the extent of the region of intense interaction between the plasma and the cathode. When combined with other parameters such as current and discharge duration, its size can yield information on erosion rate, spot residence time, and mean current density when dividing the discharge current by the observed crater area. For these reasons, arc discharge craters have been widely investigated in fields such as vacuum arc interrupters, contact materials, electrical discharge machining (EDM), and spark plug electrode applications.

Investigations of arc erosion craters produced in vacuum were carried out by Daalder [75, 76, 135], Jüttner [77], Hantzsche [136], and Puchkarev [78] for cathode metals such as

Cu, Mo and W. They measured the mean size and the number of craters as a function of the current in order to determine current densities and mean lifetime of cathode spots. Coulombe [37] investigated the surface morphology of Cu and Ti cathodes exposed to high pressure electric arcs in order to identify the arc attachment mode and estimate the size of the arc attachment points.

Wang [95, 137], Chang [138], and Hsu [139], among many other authors, investigated the arc erosion behavior of silver based composites for electrical contact applications. For this purpose, the shape and size of static-gap, single-spark craters were analyzed using SEM and profilometry techniques. Greene [140] studied the production of single craters on several metals under conditions similar to those in EDM. Crater morphology and surface texture were analyzed by means of SEM while the crater volumes were measured by a profilometer imaging technique. EDX-analyses were performed in dissimilar electrode pairs in order to obtain information on the cathode-to-anode and anode-to-cathode material transport during a discharge. The large size of the craters (~100 µm) permitted cross sections to be performed in the craters in order to estimate the thickness of the heat-affected zone.

Craters produced by single, high-pressure ignition discharges on the surface of spark plug electrodes were investigated for different materials. Lasagni [99] studied single spark craters caused on pure metal samples in order to correlate the crater size and volume with electrode material properties. Soldera [115, 116] investigated ignition craters produced on RuAl multiphase materials and pre-oxidized Ni-alloys. Similar single discharge studies were performed by Jeanvoine [141, 142] in Ag/MeO and AgNi composite contact materials, and by Rager [143] in Pt/MeO composite electrodes. All these investigations of ignition craters were based on both crater surface morphology analysis using SEM and precise crater topography and volume measurements by means of WLI. Furthermore, Soldera [144] performed TEM investigations in a crater produced in a bulk Pt cathode. The TEM foil was prepared using a focused ion beam (FIB). Voids were observed in the crater rim and the new re-solidified grains in the molten layer were found to grow epitaxially from the grains beneath. However, no molten and re-solidified area could be clearly identified.

5.2 Monitoring the Depth of Microstructure Modification

As presented in the preceding non-exhaustive review, most of the investigations carried out in single-discharge craters are limited to surface characterization. For a better understanding of crater formation, however, it will be of particular interest to be able to investigate the microstructure modifications below the crater surface. The main experimental difficulty here lies in the small size of the craters, which rarely exceed 30 µm in diameter. The application of conventional metallographic preparation methods turns out to be very difficult or even impossible when trying to achieve cross sections across single selected craters. Using FIB/SEM dual beam techniques, both precise cross sectioning and high resolution analyses are possible.

5.2.1 Bulk Electrodes

The SEM pictures in Figure 5.1 show crater cross sections in bulk Pt (a-b) and Ag (c-d) cathodes. These craters were produced at an absolute pressure of 10 bar in synthetic air. The grains can be clearly seen via electron channeling contrast. This contrast refers to the dependence of secondary electron yield on crystal orientation with respect to the incident electron beam [145]. However, the molten and re-solidified region cannot be distinguished from the unmodified one, very likely due to the epitaxial growth of the new grains that do not differ from the original grains.

For monitoring the depth of the microstructure modification induced by the discharge, one solution consists in producing craters on multilayered surfaces. This approach combining FIB cross sectioning and mapping of the damaged region in multilayers has already been employed for the investigations of nanoindentation craters [146, 147]. In the case of discharge craters, however, the modification in the layers is caused by the melting of the surface under the heat of the discharge and not by plastic deformations induced by the indenter. For simplifying the analysis of the modified region, the bi-metallic multilayer systems used in this work consist of simple binary alloy systems showing either complete immiscibility (Ag/Ni) or complete miscibility (Ni/Cu, Pt/Ni).

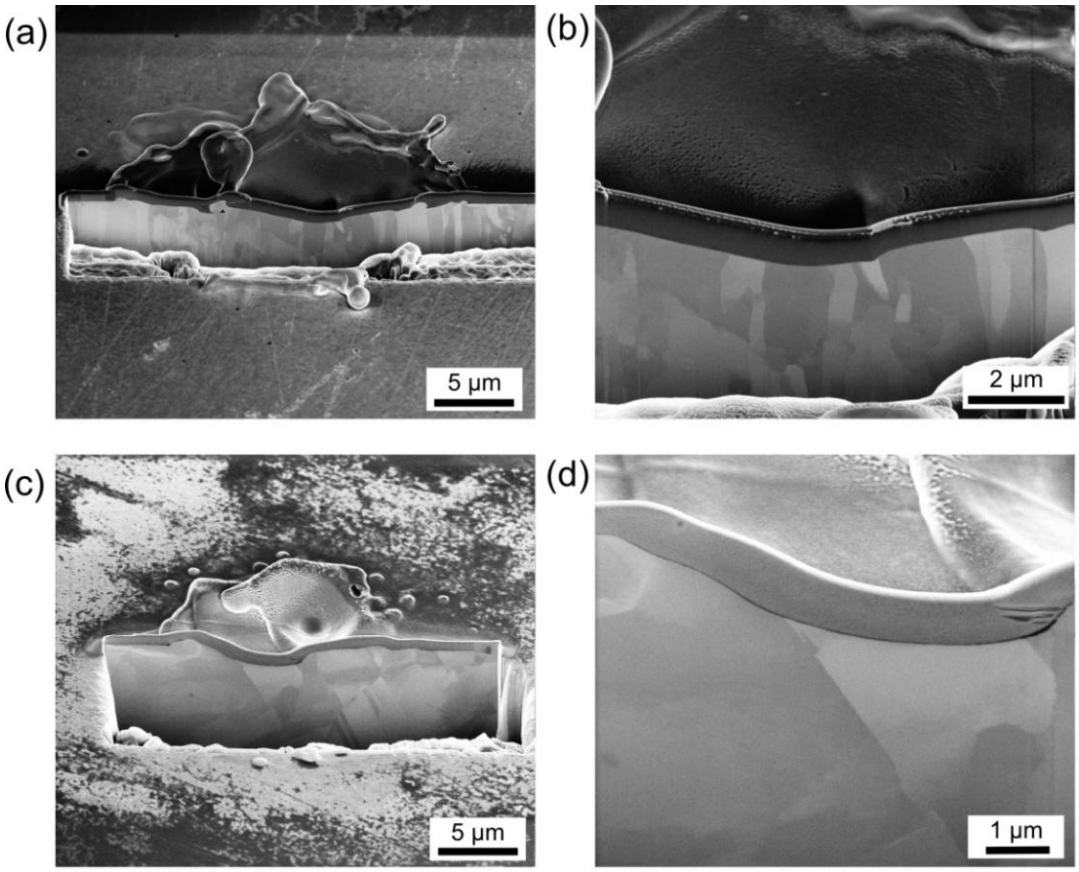

Figure 5.1 Cross sections of craters produced in pure Pt (a-b) and pure Ag (c-d) cathodes. The grains are revealed via electron channeling contrast; however, the molten region cannot be distinguished from the unchanged region.

5.2.2 Immiscible Multilayer System

The Ag-Ni phase diagram has a simple form: there are no intermediate phases and the elements have an almost complete insolubility in both solid and liquid states [148]. Figure 5.2 shows the cross section of a crater produced in a Ag/Ni multilayered electrode (10 bar, synthetic air). Except in the crater itself, the multilayered film remains intact after the spark, i.e., there is no delamination at any of the interfaces. For this crater, no Pt protective layer was deposited before the FIB milling steps, resulting in a weak curtaining effect [122] and a slightly damaged cross section edge especially in the depression center. Since the polished cross section presents no topography, the emission contrast in the SEM image is a material contrast, also called Z-contrast, due to the fact that the yield of both secondary and backscattered electrons increases with atomic number. As a result, Ag from the layers and the substrate appears brighter than Ni.

Only two layers remain unchanged in the crater depression, which corresponds to a depth of ~1.3 µm below the original surface. In the vicinity of the depression edge (<1 µm),

the Ag and Ni layers show slight expansion due to melting. Furthermore, a pronounced deformation of the layers is observed, particularly obvious in Ni films (arrow). The layers are partially broken and re-aligned parallel to the crater edge. This deformation, occurring very likely in liquid state, can be attributed to a strong pressure acting on the surface and pushing the molten material outwards to the crater centre.

Because the layers do not intermix even in the liquid state, the Ag/Ni multilayer system seems to be suitable to observe molten material displacement in crater and how individual layers are deformed under the action of the pressure. However, no new intermediate phases form and the molten layers do not differ strongly from the intact layers. As a result, it is difficult to determine the depth of the molten region with this system.

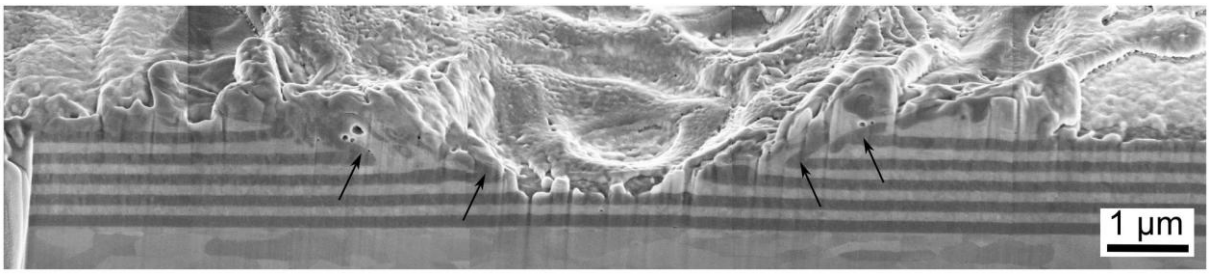

Figure 5.2 Crater cross section in a Ag/Ni multilayered surface. Pronounced deformations are observed in Ni layers (dark) in the vicinity of the depression (arrow), indicating how the molten material is pushed outwards to the crater rim.

5.2.3 Miscible Multilayer Systems

5.2.3.1 Ni/Cu Multilayer System

The first miscible multilayer system used is Cu-Ni. The Cu-Ni system is especially noted for the complete liquid and solid solubility of its two components, and is termed a binary isomorphous alloy. When the liquid Cu-Ni alloy solidifies at equilibrium, it forms a homogeneous substitutional solid solution.

The left SEM micrograph in Figure 5.3 shows the overall cross section of a crater produced on the Ni/Cu multilayer system (5 bar, synthetic air). The crater presents a flat undulated molten surface without a deep depression, as it is usually observed in craters on bulk Ni electrodes. The right SEM micrograph in Figure 5.3 shows a magnification of the cross section in the center of the crater (black frame). The light layer at the top of the cross section is the Pt protective band, and the bottom region is the Ag substrate. Two distinct regions can be identified in the multilayer assembly. The lower one, close to the Ag substrate,

is still composed of unmodified individual Cu and Ni layers. Since the atomic number of both elements is very close, 28 for Ni and 29 for Cu, the contrast between the layers is low. In the surface region, directly beneath the Pt band, the multilayer structure has disappeared and a coarse grained structure is observed. The formation of this region results from the melting of the top layers under the heat of the discharge. The pressure of the plasma acting on the molten surface causes convective mixing, and substantial diffusion in the liquid state can occur, effectively mixing both metals. Since the Ni/Cu system is completely miscible a Cu-Ni solid solution phase is formed upon re-solidification as confirmed later by EDX analysis. The contrast between the coarse grained, resolidified Cu-Ni phase and the unmodified layers allows delimiting the molten region. By observing this boundary along the whole crater cross section, the extent of the molten pool can be estimated. If one examines the cross section carefully, a third region situated between the unmodified layers and the Cu-Ni solid solution region can be observed. In this zone, the layers are still present but they show some deformation. This third region will be further discussed later in this section.

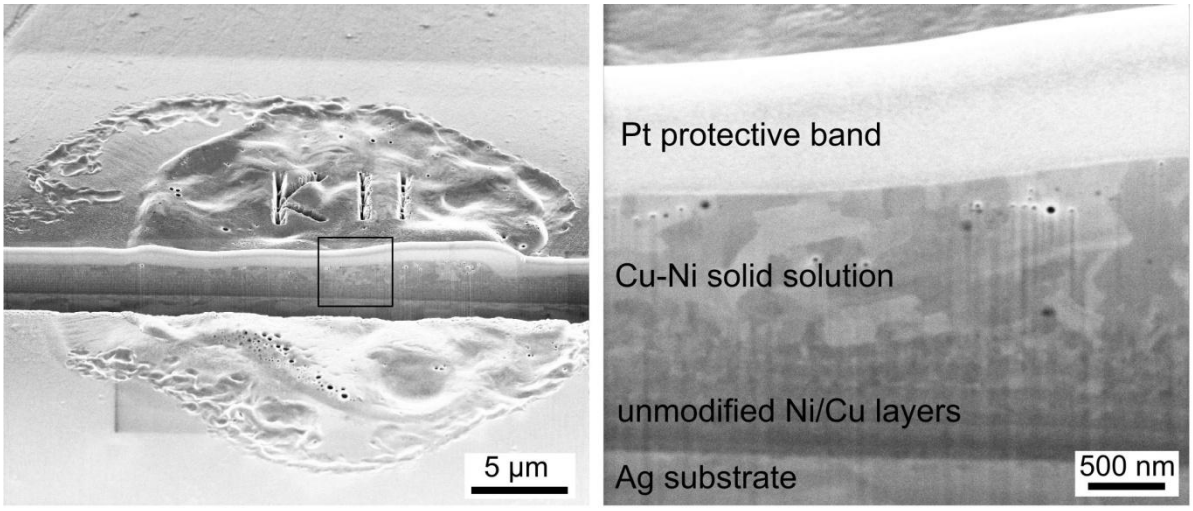

Figure 5.3 Crater cross section in a Ni/Cu multilayer. The contrast between the fine grains of the unmodified Ni and Cu layers and the coarse grains of the Cu-Ni solid solution permits the monitoring of the molten region.

Figure 5.4 shows a TEM image of the cross section in a crater. In addition, selected area diffraction patterns are shown where an individual diffraction pattern comes from an area of approximately 200 nm in diameter (as indicated by the circles on the figure). In the lower region (A), the layers have not been modified. The ring diffraction pattern in Figure 5.4 A indicates that the grains in this region are small (~5-10 nm). The fine grained structure of the layers results from the low deposition rate technique employed for their fabrication. The diffraction pattern in the upper region shows discrete points from the reflection of a few large

grains (Figure 5.4 B). These large grains are resulting from the melting and mixing of the Cu and Ni layers followed by the re-solidification into a coarse grained Cu-Ni solid solution.

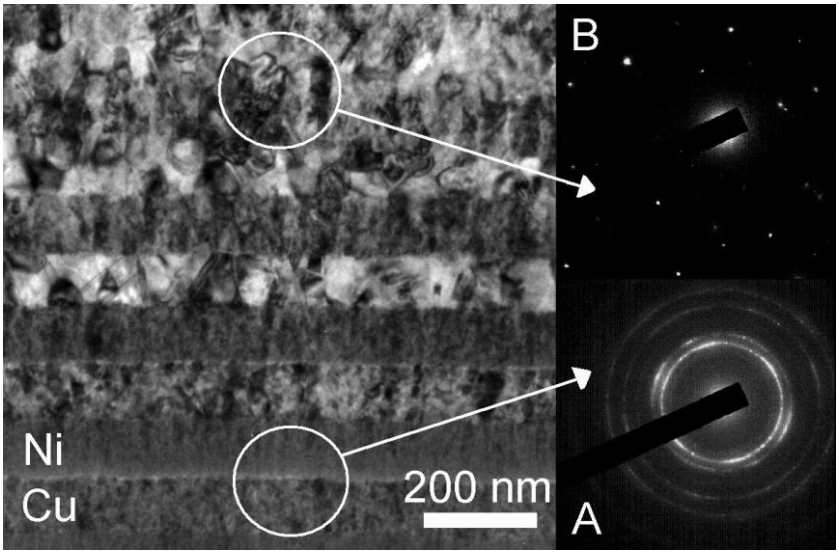

Figure 5.4 TEM image (bright field) and selected area diffraction patterns of the Cu/Ni multilayer sample at two different depths below the crater surface. The unmodified region (A) is very fine grained ("as-sputtered" texture). The upper molten region (B) is composed of large grains resulting from melting and re-solidification.

Figure 5.5 shows an EDX mapping of a TEM foil prepared in the center of the crater. In comparison with EDX analysis on a bulk sample, a much higher resolution can be achieved since the depth of interaction between the electrons and the material is reduced to the thickness of the specimen [149] (~100 nm). The distribution of selected elements is plotted with different colors: green for Ag, purple for Pt, red for Cu and yellow for Ni.

Three regions can be clearly distinguished. In the upper region (1) both Cu and Ni elements are mixed together confirming the melting and the formation of a Cu-Ni solid solution upon cooling. Because the solidification is assumed to occur far from equilibrium conditions, a nonuniform alloy with grains showing a cored structure can be expected [150]. However, despite the high resolution of the present EDX analysis, segregation and gradient composition inside the grains cannot be revealed. In the lower region (3) the layers remains as deposited and present neither melting nor mixing. In the intermediate region (2) the copper layers show variations of their thickness due to the expansion that takes place upon melting. Ni layers, however, show a constant thickness (no melting) but present some deformations due to the stress induced by the melting and expansion of the surrounding Cu layers. Using these three regions, the maximal temperature in the crater can be monitored as a function of the depth: In region (1) the temperature is higher than the melting point of Ni (T>1455°C). In

region (2) the temperature may lay between the melting points of Ni and Cu (1084°C<T<1455°C). In region (3), the temperature remains below the melting point of Cu (T<1084°C). Knowing the thickness of these regions, the temperature gradient in the crater depth can be estimated to be on the order of 700 K/µm.

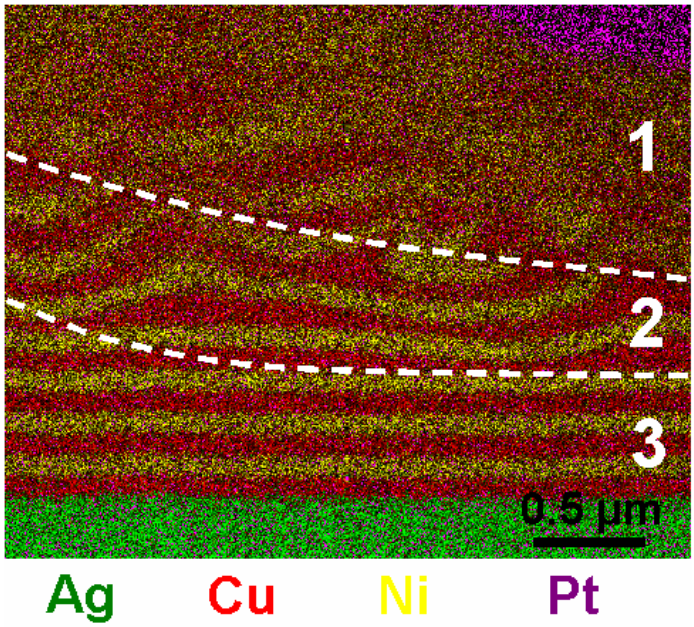

Figure 5.5 High resolution cross-sectional chemical analysis in a crater produced on the Ni/Cu multilayer system. The EDX element mapping reveals the melting of the layers as function of depth. Three regions delimited by dashed lines can be observed permitting the estimation of the temperature gradient below the crater surface.

5.2.3.2 Pt/Ni Multilayer System

The second miscible multilayer system used for monitoring the depth of melting is Pt/Ni. The Pt-Ni phase diagram is characterized by the existence of a face centered cubic (fcc) solid solution over the whole concentration range at temperatures above 620°C. At intermediate temperatures, the disordered solid solution transforms via first-order transitions into ordered $Ni_3Pt(L1_2)$, $NiPt(L1_0)$, and $NiPt_3(L1_2)$ phases, depending on the concentration [148].

The SEM image in Figure 5.6 shows the cross section of the center of a crater in the Pt/Ni multilayer system. This crater was produced in air at an absolute pressure of 6 bar. In contrast to the previous Ni/Cu multilayer system, Pt and Ni layers show an important contrast (Z-contrast) that permits to distinguish them clearly. The Pt layers (Z=78) appear bright while the Ni layers (Z=29) are dark. A contrast can also be observed between the Pt from the

protective band (in the plane of the cross section) and the Pt from the multilayer. This can be explained by the fact that the Pt protective band is contaminated with Ga from the ion beam and C from the precursor gas, while the sputter deposited Pt layers have much higher purity. Grain refinement of the Ag substrate surface can be observed resulting from the mechanical polishing of the substrate prior to the layer deposition by PVD. This points out that the substrate remains solid during the melting of the multilayered surface.

The 6-7 bottom layers remain unchanged during the formation of the crater. Below the crater surface, a region of mixing is observed. Like for the Ni/Cu multilayer system, the formation of this region is caused by the mixing of the molten top layers and the re-solidification in a Pt-Ni solid solution. As this region is composed of both Pt and Ni, it presents an intermediate contrast between that of the Pt layers and of the Ni layers. The different gray levels between the layers and the solid solution permit to clearly distinguish the molten zone from the unmodified regions. For a liquid having a composition close to $Pt_{50}Ni_{50}$ (stoichiometry of the multilayer), the phase diagram predicts the formation of a solid solution, which transforms into a NiPt ordered phase at temperatures below 620°C. This transformation, however, takes place in equilibrium condition, i.e., for slow cooling rates. FEM simulations of the temperature in a crater produced by the arc phase reported cooling rates on the order of $\sim 10^7$ K/s [151]. Therefore, it is very likely that the solid solution phase is rapidly quenched, preventing the formation of any ordered phases by diffusion.

Pores are sometimes observed in the molten zone of craters produced in Pt/Ni multilayers. Careful examination shows that these pores originate from the molten Ni layers. It is likely that the pores are resulting from the entrapment and inclusion of argon atoms in the nickel layers during the PVD process. Upon melting of the layers, desorption might occur with the formation of gas bubbles now visible as pores. This hypothesis is supported by the fact that argon inclusion was already reported in ion beam sputter-deposited gold layers realized at an argon pressure even slightly lower than in our case [152].

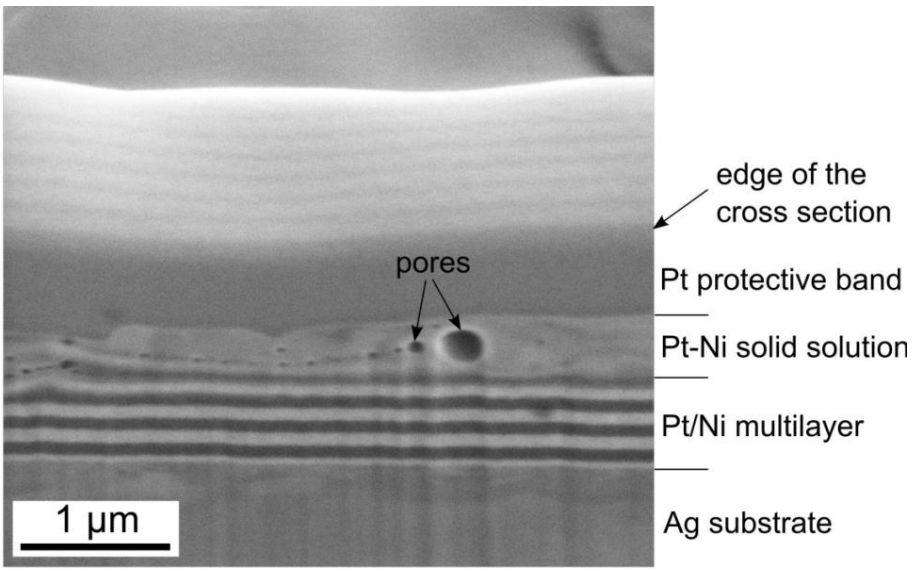

Figure 5.6 Cross section in the center of a crater produced on the Pt/Ni multilayer system. The melting and mixing of the upper layers results in the formation of a Pt-Ni solid solution, which can be clearly distinguished from the unmodified bottom layers, permitting the monitoring of the molten zone.

5.2.4 Comparison between Craters on Bulk and Multilayered Electrodes

The multilayer systems aim to act as markers in order to monitor modifications in the depth of the crater and determine the extent of the molten zone. As discussed in section 5.2.1, this cannot be achieved in bulk electrodes. It is important, however, that the multilayered cathode does not modify the behavior of the discharge in comparison with that of pure metal cathodes. Otherwise, the information gained in multilayers could not be used for the case of bulk electrodes as in real spark plug electrodes. The analysis of the voltage-time curves has no statistical significance for single-spark experiments because the number of discharges produced is too low. A straightforward comparison consists in analyzing, qualitatively and quantitatively, the craters produced on both bulk and multilayered electrodes.

Figure 5.7 shows the surface morphology of craters generated on bulk Ag, Pt, Ni electrodes (left) and Ag/Ni, Pt/Ni, Ni/Cu multilayered electrodes (right). It is interesting to note that the craters produced on bulk electrodes are similar in shape and size to those produced on multilayered electrodes when the surface layer is made of the same metal. For both bulk Ag and Ag/Ni, the craters consist of several small depressions having a diameter of ~5 µm. Craters in bulk Pt and Pt/Ni consist of fewer depressions having a slightly larger diameter ranging between 5 and 10 µm. The edge of the craters is clearly marked by a rim of molten material. Some pores are observed on the surface of the crater produced on the Pt/Ni

electrode, which are not observed on bulk Pt electrode. In bulk Ni as in Ni/Cu, the craters show a typical, smooth, undulated molten surface having a large diameter of ~30 µm. Contrary to Ag and Pt, these craters do not exhibit depressions.

It is also interesting to compare the topography of the craters, determined by WLI measurements. For this purpose, one can use the peak-to-valley value, which corresponds to the distance between the highest point (peak) and the lowest point (valley) within the crater area. Craters on bulk Pt have a peak-to-valley value of $2.63^{\pm 0.69}$ µm, close to that measured on Pt/Ni of $2.49^{\pm 0.32}$ µm. On bulk Ni and Ni/Cu, however, craters are shallower and the peak-to-valley value is of $1.55^{\pm 0.30}$ µm and $1.36^{\pm 0.35}$ µm, respectively. These results demonstrate that not only the morphology but also the size and depth are similar between craters generated on bulk electrodes and craters produced on multilayered electrodes. For multilayers, the type of crater is determined by the metal used on the surface layer.

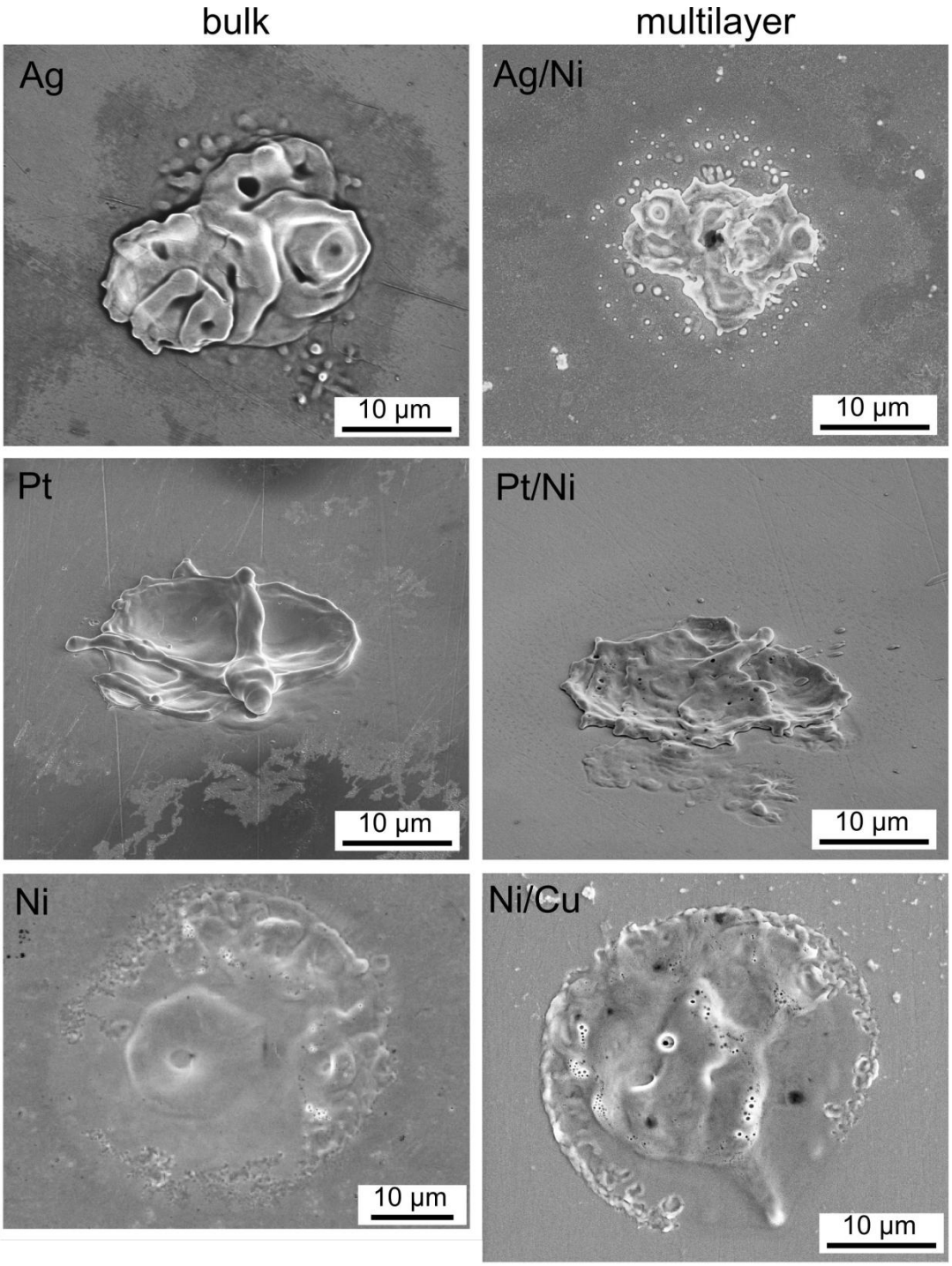

Figure 5.7 SEM images of craters produced on bulk Ag, Pt, Ni electrodes (left) and Ag/Ni, Pt/Ni, Ni/Cu multilayered electrodes (the image of the crater in bulk Ni is taken from [116]).

5.3 Microstructure of Craters Produced at Different Pressures

The influence of external pressure on crater formation is investigated in Pt/Ni multilayered cathodes for absolute pressures ranging from 1 to 10 bar in synthetic air.

5.3.1 Surface Characterization

The craters produced at external pressures of 1 and 4 bar present a smooth undulated molten surface with a central protrusion as shown in Figure 5.8a. The diameter of these craters rarely exceeds 10 µm. When the discharges are generated at pressures of 7 and 10 bar, the craters show a shape typical for cathode spot craters. They consist of one or several central depressions surrounded by a rim of molten material (Figure 5.8b). The formation of a depression and the flow of molten material outwards from the crater center will be discussed later in this chapter. The total diameter of these craters lies between 10 µm and 20 µm.

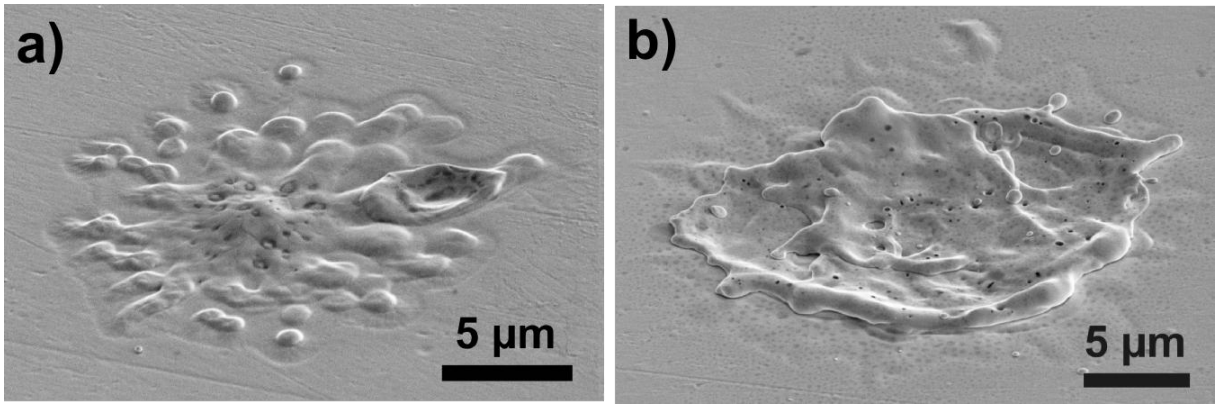

Figure 5.8 a) SEM image of a crater produced at an external pressure of 1 bar and showing a smooth undulated molten surface; b) SEM image of a crater produced at an external pressure of 10 bar and presenting a typical crater shape with a central depression surrounded by a rim of molten material.

Using WLI, the topography of the craters can be accurately measured and different surface parameters can be determined. The root-mean-square (rms) roughness is a good discriminator to quantitatively distinguish the two distinct morphologies of craters (Figure 5.9). The rms roughness is the average of the measured height deviations z taken within the crater area S and measured from the mean linear surface. The smooth craters created by discharges at 1 and 4 bar have roughness values between 50 and 100 nm, whereas at 7 and 10 bar, the craters show much higher roughness values in the range of 200 nm.

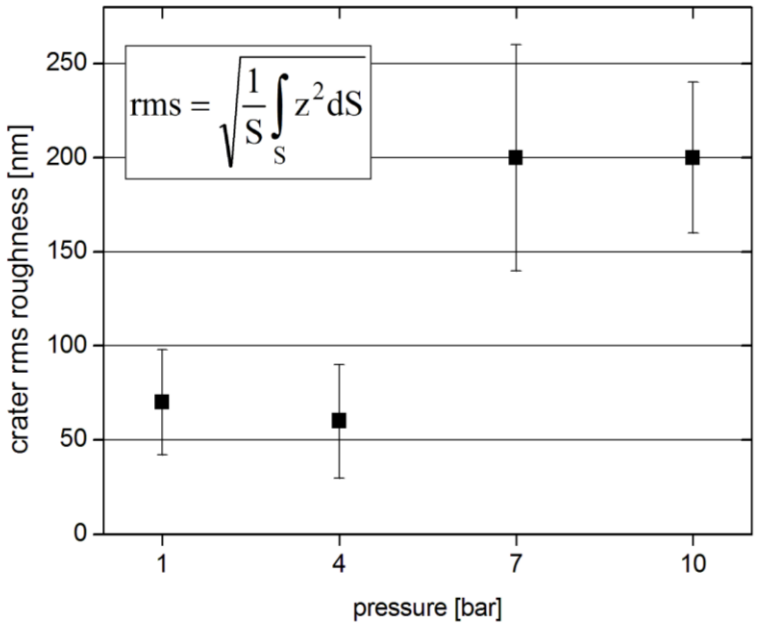

Figure 5.9 Crater rms roughness as a function of external pressure revealing the two types of crater morphologies. At low pressures (1 and 4 bar) craters are relatively smooth with low roughness values, whereas at elevated pressures (7 and 10 bar) craters show a higher topography with larger roughness values.

5.3.2 Crater Cross Section Analysis

In order to analyze the region below the surface, site specific cross sections were performed in craters using the FIB/SEM dual beam workstation as previously described in 3.4.2.3.

Figure 5.10 shows SEM images of a FIB cross section performed in the center of a crater produced at 1 bar. In the craters produced at low pressure (1 and 4 bar) the depth of modification does not exceed the 4-5 top layers. The deformation and expansion of the layers are evidence of melting. However, no mixing occurs and the Pt layers can still be clearly distinguished from the Ni layers. Nevertheless, if one examines Figure 5.10b carefully, it appears that the upper layers near the Pt protective strip are more diffuse than those near the Ag substrate. This observation suggests that there is some interdiffusion going on at the interface of the melted layers.

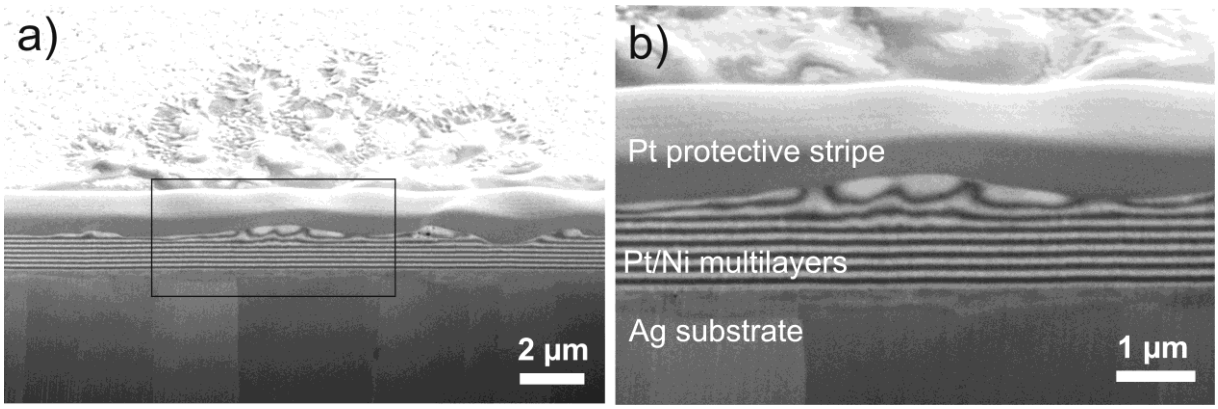

Figure 5.10 FIB cross section in a crater produced at 1 bar; a) overall view of crater cross section; b) crater protrusion with deformation of the upper Ni (dark) and Pt (light) layers due to melting.

Figure 5.11 shows SEM images of a FIB cross section performed in the center of a crater produced at 7 bar. In the craters caused by discharges at higher external pressures (7 and 10 bar), the melting zone extends to greater depths (~1 µm). In addition, a region of Pt-Ni solid-solution, having a contrast between those of Pt and Ni, can be clearly observed. The contour of the Pt-Ni solid solution delimits the extent of the molten pool. This region results from the complete intermixing of the molten Pt and Ni layers below the surface. This suggests that turbulent mixing is taking place in the molten pool probably due to the high pressure acting on the molten surface. This pressure is also responsible for the displacement of material and the formation of crater depressions and rims. The presence of pores in the molten pool is likely due to the desorption of argon, as mentioned previously in 5.2.3.2.

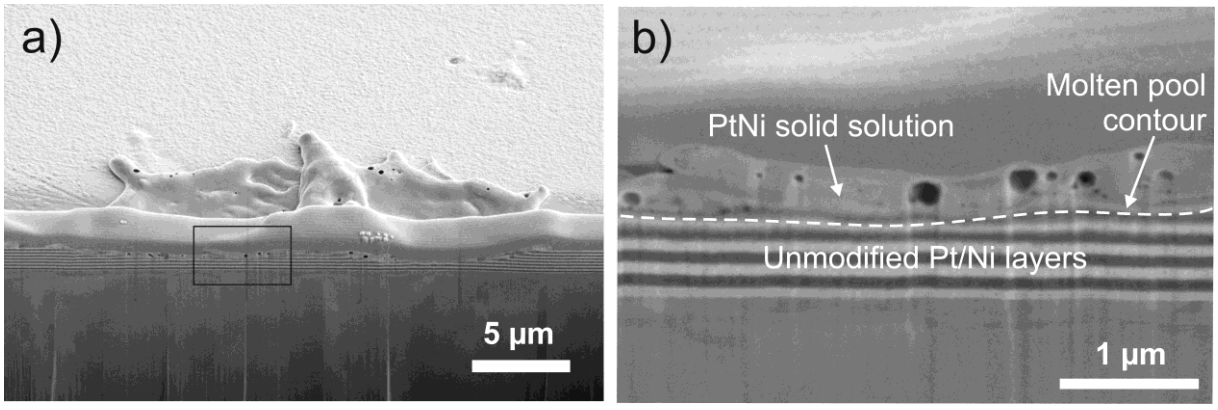

Figure 5.11 FIB cross section in a crater produced at 7 bar: a) overall view of the crater cross section; b) in the crater depression where the Pt/Ni layers below the surface have partially melted and mixed, forming a Pt-Ni solid solution. The limit between the Pt-Ni solid solution and the unmodified layers shows the contour of the molten pool (dashed line).

5.3.3 Determination of the Molten Pool Volume

Modifications of the multilayer assembly due to deformation or mixing of the layers permit to monitor the extent of the molten pool. Since the FIB cross sections are performed in the center of the craters, we consider that the exposed melting radius and melting depths are maximal. Assuming the shape of the molten pool as a spherical cap, the volume of molten material V_m in the craters can be estimated by:

$$V_m = \frac{\pi}{6} \cdot z_m (3r_m^2 + z_m^2) \tag{5.1}$$

where z_m and r_m are the experimentally measured molten depth and molten radius, respectively. The molten volumes calculated with equation (5.1) are displayed in Figure 5.12 as a function of the pressure. At 1 and 4 bar, the volume of the molten pools is approximately 50 µm^3, whereas at 7 and 10 bar, it lies between 200 and 250 µm^3. Like with the crater roughness (Figure 5.9), two types of craters are revealed: low pressure craters with small amounts of molten material (~50 µm^3) and high pressure craters with molten pool volumes in the range of 200-250 µm^3.

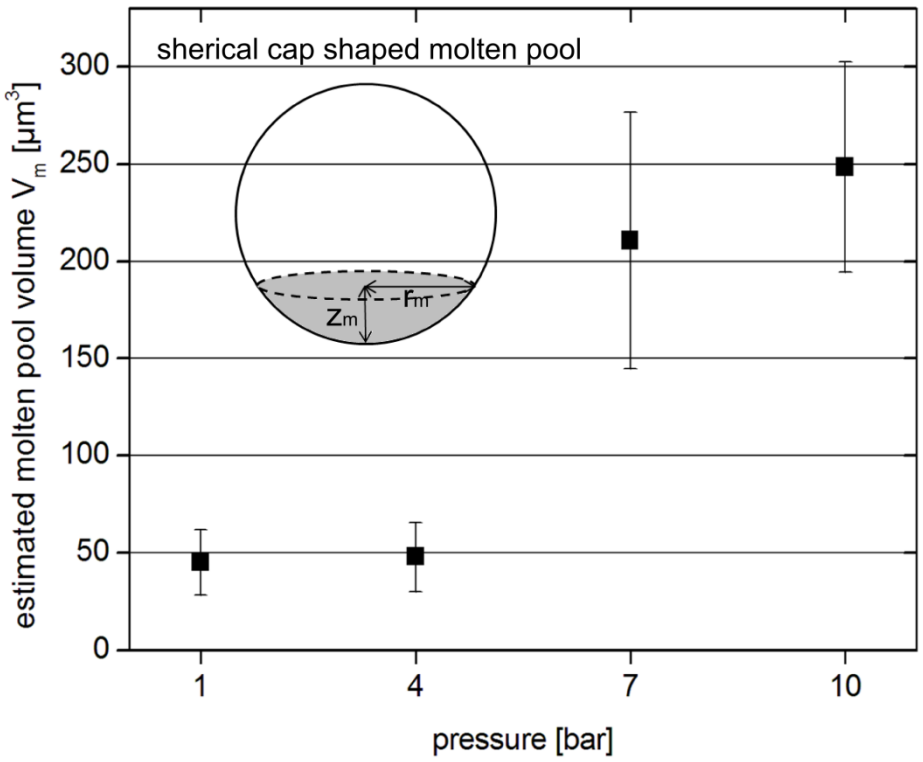

Figure 5.12 Estimated volumes of the crater molten pool as a function of the pressure. The volumes are calculated assuming the shape of the molten pool as a spherical cap, where z_m and r_m are the measured molten depth and molten radius, respectively.

5.3.4 3D Reconstruction of the Molten Pool

A more precise determination of the molten volume consists in performing a 3D reconstruction of the crater molten pool using FIB nanotomography. This was realized in a crater produced at 6 bar and having the same shape and size than the craters produced at 7 and 10 bar (Figure 5.8b), i.e., high pressure craters. Serial cross sectioning was performed by FIB using the slice and view program of the dual beam workstation. This program automatically performs a series of regularly spaced cuts and collects electron images of each of these slices. Similar to single cross-sectioning, mentioned in 3.3.2.2, a Pt protective film of the dimensions of the slicing area was deposited *in-situ* using the ion beam. For this reconstruction, 200 slices with a thickness of 100 nm were milled through the crater. The serial sectioning was performed using a 500 pA ion current and SEM pictures of each cross section were collected automatically. A schematic representation of the procedure is shown in Figure 5.13a. In this figure, for clarity, only 4 slices out of 200 are shown.

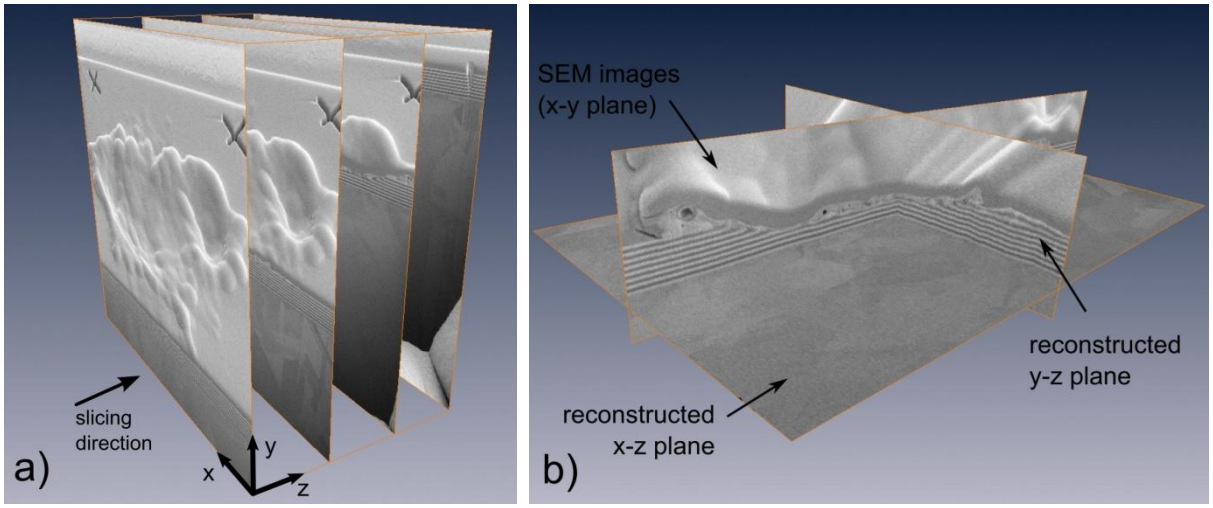

Figure 5.13 a) Stack of four out of 200 SEM images through the crater, obtained during the serial cross-sectioning procedure. b) 3D volume rendering: the x-y plane is a collected SEM image while the x-z and y-z planes are reconstructed by the software via interpolation.

The image processing and 3D reconstruction was performed with the commercial software Amira 5. Since the sample is tilted with respect to the electron beam, the cross section planes are systematically shifted vertically from slice to slice. Therefore, the slices have to be re-aligned in order to account for the aforementioned projection displacement and for any image-drift. After this step, a 3D rendering of the volume can be performed and planes can be reconstructed in arbitrary directions as shown in Figure 5.13b for x-z and y-z planes.

The three dimensional rendering is revealed to provide a proper visualization of the true microstructure below the surface. In particular, the reconstruction of horizontal x-z planes (also called coronal views) at different depths provides a clear picture of the extent of the molten zone. Figure 5.14 shows reconstructed horizontal x-z planes at different distances relative to the original surface: +420 nm, 0 (original surface), -420 nm and -840 nm, respectively. In the first picture (+420 nm) the crown of molten material forming the crater walls with the presence of pores can be clearly observed. The dark region corresponds to the intersection between the horizontal plane and the Pt protective layer deposited on the surface. At the original surface level (0), the first Pt layer (wide bright band) and the first Ni layer (dark region on the bottom left corner) can be seen. As the depth of the cut plane increases, the area of the crater region decreases. In the last picture (-840 nm) only the two deeper depressions of the crater can still be visualized.

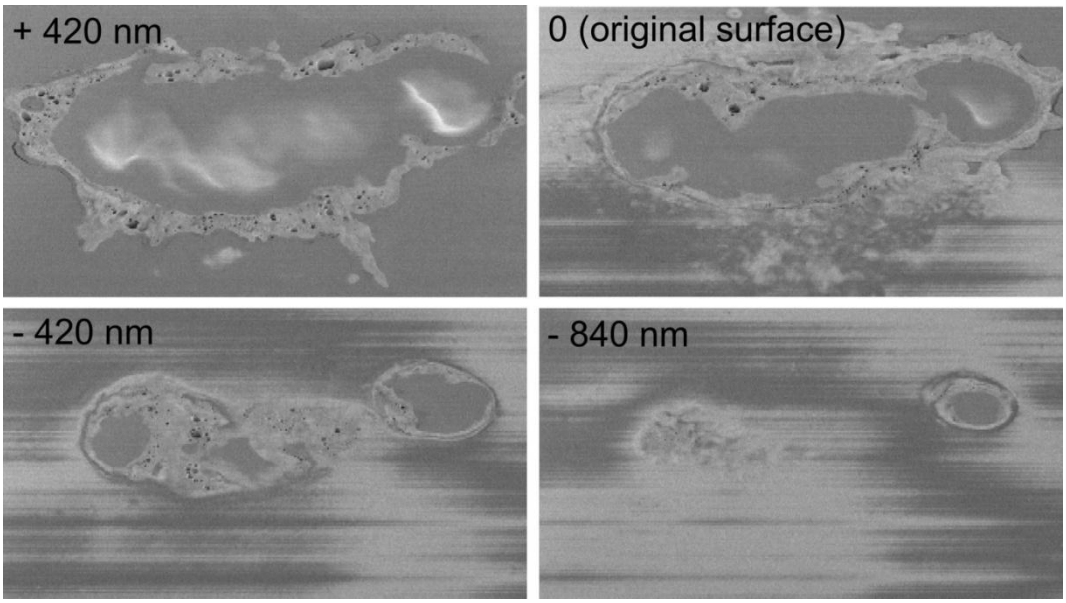

Figure 5.14 Reconstructed horizontal planes at different depths relative to the surface providing a clear picture of the extent of the crater as a function of depth.

For further quantitative analysis, the molten pool of the crater was reconstructed by volume segmentation. This procedure consists in defining a volume either by suitable chosen gray levels or by eye inspection and manual segmentation of the micrographs. In the present case, the insufficient contrast between the molten material and the layers does not permit automatic segmentation. Thus, the segmentation was performed manually by highlighting the area of the molten region in each slice. After this step, the surface of the segmented volume is generated via triangulation and the molten pool can be visualized in 3D (Figure 5.15).

The resolution of the 3D image is determined by the size of the voxels (voxel="3D pixel"), in our case, 33 nm, 42 nm and 100 nm in the x, y, and z axes, respectively. Note that the resolution in the z-axis corresponds to the slice thickness, i.e., 100 nm. Knowing the voxel size, the volume of the segmented molten pool can be calculated. The molten volume was found to be 208 μm^3 including all pores, which is comparable with the estimations based on the FIB cross sections for craters produced at 7 and 10 bar (Figure 5.12). This also validates the assumption of the shape of the molten pool as a spherical cap.

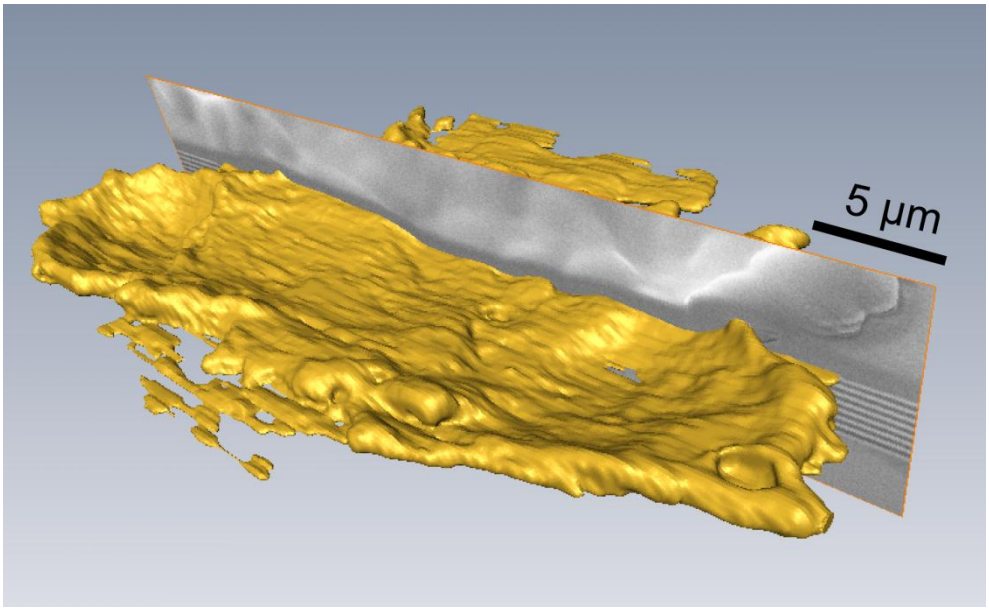

Figure 5.15 3D reconstruction of the crater by means of FIB nanotomography. The surface of the molten pool can be visualized together with one slice of the serial cross section. The volume of the reconstructed molten pool was found to be 208 μm^3.

5.3.5 Cross Section EBSD

For further characterization of the microstructure, electron backscatter diffraction (EBSD) was performed in a crater produced at 10 bar. EBSD analyses are usually performed on surfaces, where the sample is tilted to 70°. However, in the present case, the measurement had to be performed in a cross section perpendicular to the sample surface. In this position, a direct EBSD measurement is not possible because the remaining sample shields the EBSD detector from the backscattered electrons being emitted from the cross section. To avoid this geometrical problem, one alternative proposed by Holzapfel [153] consists in cutting and transferring the volume of interest to the edge of the sample. This procedure is essentially similar to lift-out TEM foil preparation, except that the volume here is much thicker (~2 µm) than a usual TEM foil (<100 nm). The volume containing the center part of the crater is cut

free by FIB milling (Figure 5.16a) and fixed on the tip on the micromanipulator by Pt deposition to be transferred to the edge of the sample (Figure 5.16b). Once positioned correctly, it is fixed by Pt deposition and the cross-section is further polished using low current ion beams (Figure 5.16c). Figure 5.16d shows the ion-polished cross section at the end of the preparation step. Ion polishing is an important advantage of FIB compared to other techniques, which permits the *in-situ* preparation of good quality surfaces for EBSD with only minor deformation, even in surfaces composed of materials having different hardness [154].

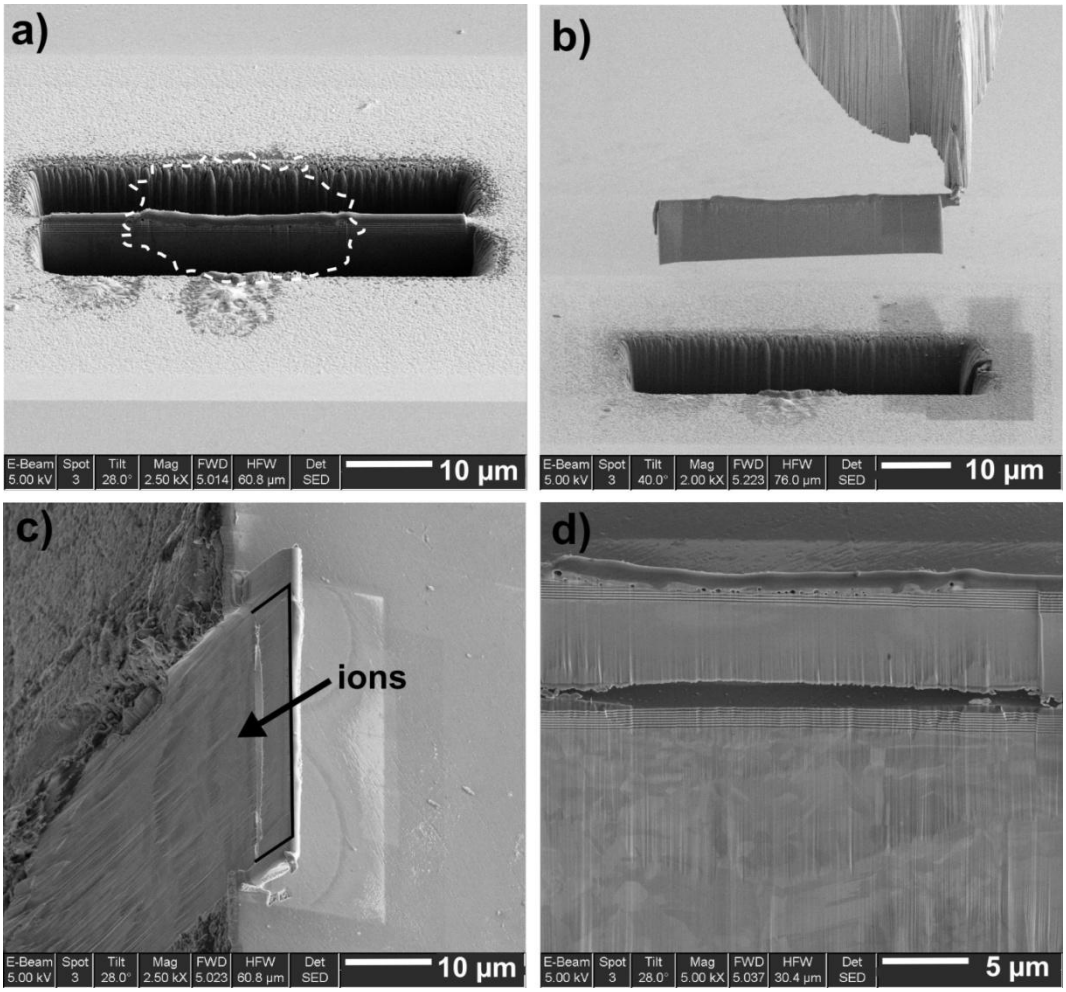

Figure 5.16 EBSD preparation steps in a crater; a) The center part of the crater is cut free on both sides. The dashed line shows the original contour of the crater; b) The foil is lifted out with the micromanipulator; c) The foil is positioned on the edge of the electrode where it is fixed by platinum deposition and polished with ions; d) Polished crater cross section providing the required surface quality for EBSD.

The results of the EBSD measurement are summarized in Figure 5.17. Figure 5.17a shows the SEM image of half of the crater cross section, whereas Figures 5.17b and 5.17c are the corresponding image quality map (iq) and the [001] inverse pole figure (ipf).

The image quality is low in the unmodified bottom layers (dark points in the iq map) due to the small size of the grains (<50 nm) resulting from the PVD process. The image quality, however, is lower in the Ni layers than in the Pt layers. This might be due to the aforementioned incorporation of argon in the Ni layers during the PVD process, which leads to lattice imperfection and decreases the image quality. In the Ag substrate as well as in the melted/re-solidified region, image quality is higher and a reliable measurement of grain orientation is possible (bright points in the iq map).

The ipf provides a color-coded map of the orientation of the grains (Figure 5.17c). The normal direction of the ipf is normal to the electrode surface and the phase used for indexing the EBSD patterns is Pt, which has the same fcc (face centered cubic) structure as Ni. Thus Pt, Ni and the Pt-Ni solid solution can all be indexed correctly with this same phase. Note that the goal here is not to differentiate the phases but only to get information about the orientation of the grains. The grains in the molten pool (Pt-Ni) are elongated in the direction normal to the surface and have re-crystallized into a columnar form. The length of the grains corresponds approximately to the thickness of the molten zone and thus increases from the crater center to the crater rim.

The orientation analysis of the molten and re-solidified region is plotted in the form of {111} and {220} pole figures in Figure 5.17d. Even if only a few grains contribute to the pole figures, a <111> texture is clearly revealed. This indicates that the grains grow preferentially with their {111} planes parallel to the surface rather than the {100} planes, which is more usual for solidified fcc metals [155]. The formation of a <111> texture can be explained under planar growth conditions [156], that is, under directional solidification and, for alloys, under high temperature gradients [157]. According to the plot of temperature gradient versus solidification rate and solidification morphology shown in [158], plane front solidification occurs for temperature gradients higher than 1000 K/µm. This value is on the same order of magnitude as the temperature gradient determined experimentally in the Ni/Cu multilayer system of ~700 K/µm. It is also well in accordance with values estimated roughly as follows. Assuming that the surface is at the boiling point of Pt (T_b^{Pt}=4100 K) and knowing that the melting depth is approximately 1 µm (T=T_m^{Pt}=2045 K at z=1 µm), the temperature gradient in the molten pool can be estimated to be ~2000 K/µm. As the molten pool cools down, the arc is extinguished and the heat can only be dissipated by conduction in the bulk. This results in high temperature gradients directed normally to the surface and in the formation of elongated grains with a <111> orientation.

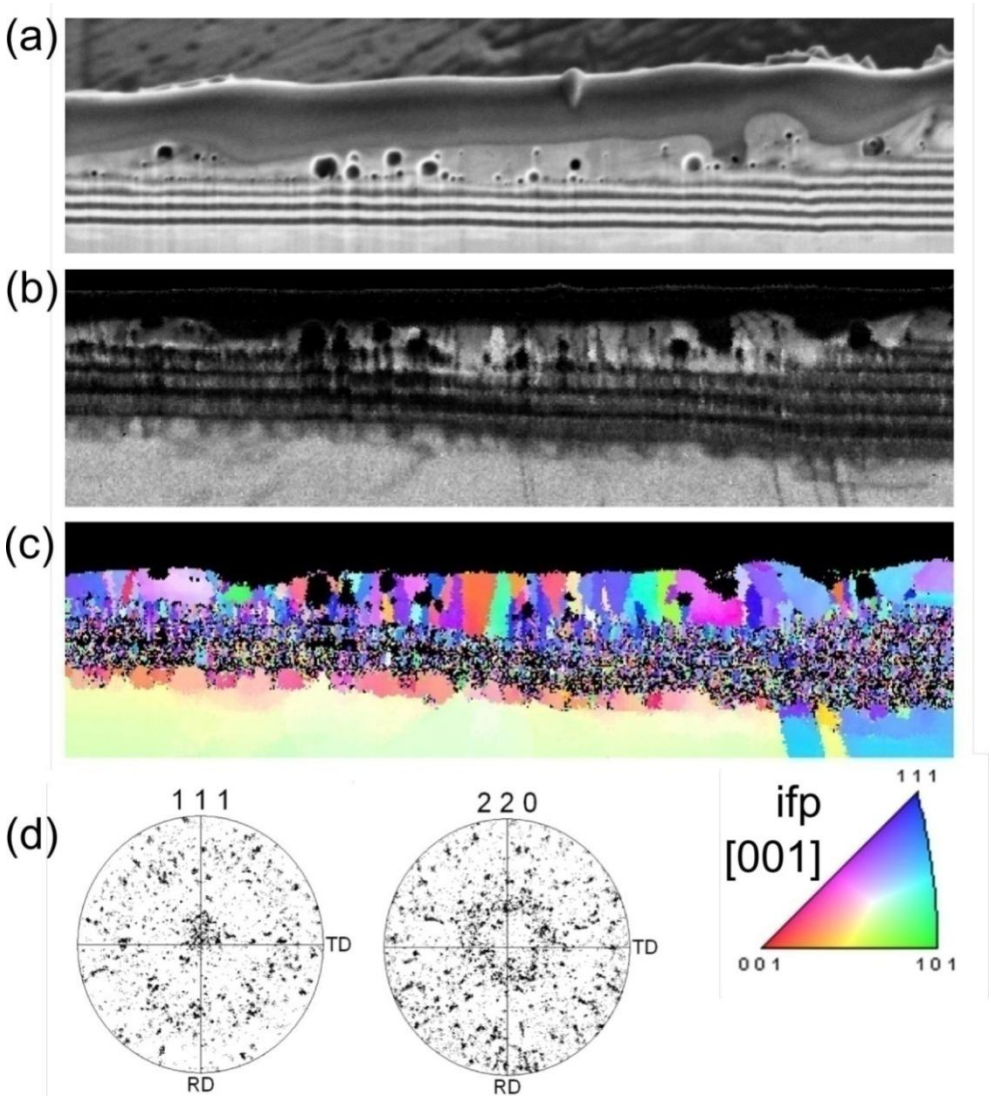

Figure 5.17 EBSD in the cross section of a crater produced at 10 bar: (a) SEM image of the cross section (5 kV accelerating voltage); (b) image quality map (iq); (c) [001] inverse pole figure (ipf) map where the morphology and orientation of the grains in the molten pool can be seen (normal direction is normal to the electrode surface); (d) {111} and {220} pole figures of the re-solidified grains showing a <111> texture.

5.4 Discussion

5.4.1 Low and High Pressure Craters

The microstructural investigations in Pt/Ni cathodes have revealed that two types of craters are formed depending on the external pressure at which the discharges are produced. These craters might be caused by two different parts of the ignition discharge.

In low pressure conditions (1-4 bar), the discharge causes superficial melting of the cathode surface with molten volumes around 50 μm^3. However, no depressions are formed at

the crater center and in the case of multilayers, no mixing of the molten layers occurs. These observations indicate that no severe pressure is acting on the molten surface during crater formation. The arc fraction measurements presented in Chapter 4 as well as a previous study [96] have shown that, at low pressures, the initial breakdown is immediately followed by the glow discharge. Although the energy of the glow discharge is relatively high (30-50 mJ), the discharge takes place over a large area (~mm^2) and a large time scale (~ms), leading to a low power input density in the range of 10^6 W/m^2, which is not sufficient to cause the melting of the surface (see section 6.1.3 in the next chapter). Therefore, the smooth craters observed at the cathode surface when discharges are produced at low pressure can only be attributed to the energy dissipated in the breakdown phase.

The craters left at the surface by discharges generated at higher external pressures (6-10 bar) present deep central depressions and greater molten volumes in the range of 200-250 μm^3. Furthermore, a turbulent mixing of the molten Pt and Ni layers takes place, suggesting that a pressure is acting on the surface during the melting stage. These craters present great similarities, in shape and size, to cathode spot craters that are caused by vacuum or atmospheric arcs. A detailed phenomenological description of this type of crater is made in [80]. The formation of these craters can thus be attributed to an arc occurring either during the capacitive discharge or the inductive discharge. However, the fact that the external pressure does not influence the initial current of the inductive discharge (~100 mA), and that similar arc craters reported in the literature are usually produced by currents in excess of 1 A, suggest that the craters are likely formed during the short capacitive discharge which immediately follows the breakdown, when high currents must be sustained. The influence of the external pressure on the current of the capacitive discharge and the formation of the craters will be discussed in detail in section 6.3.3. The similarity of our craters to arc cathode spot craters also justifies the use of the cathode spot model for the thermal simulation presented in the next chapter.

5.4.2 Crater Formation Mechanisms

The craters observed at elevated pressures result from both intensive heating and high pressure acting simultaneously at the surface. The pressure acting on the molten surface accelerates and pushes the liquid metal outwards, resulting in the formation of crater depressions and rims. Furthermore, in the case of multilayered surfaces, the formation of a solid solution indicates that convection-induced mixing is occurring in the molten layers.

The driving forces for fluid flow in a molten pool include different mechanisms such as plasma (or ion) pressure [44, 47], electromagnetic (or Lorentz) force and surface tension gradient [159-162]. The impinging ions produce a pressure normal to the surface of the molten pool, whereas the Lorentz force and the surface tension gradient generate a shear stress directed outward on and in the molten pool and cause the liquid metal to flow from the center to the edge of the pool. The three mechanisms are represented schematically in Figure 5.18. The Lorentz force is caused by the interaction between the current path in the molten pool and the magnetic field B it generates. The electric current lines are penetrating the cathode (negative electrode) resulting in a radial Lorentz force directed outward. The radial flow of liquid metal caused by electromagnetic forces is also known as pinch effect. The surface tension shear stress is caused by the temperature gradient within the pool surface. The surface tension of a liquid metal γ_l decreases with increasing temperature T, namely $\partial\gamma_l/\partial T < 0$ (in the absence of surface active agents [163]). The warmer liquid with a lower surface tension at the center of the pool is pulled outward by the cooler liquid metal with a higher surface tension at the edge of the pool, resulting in an outward shear stress. Surface tension driven flow is also called thermocapillarity flow or Marangoni flow.

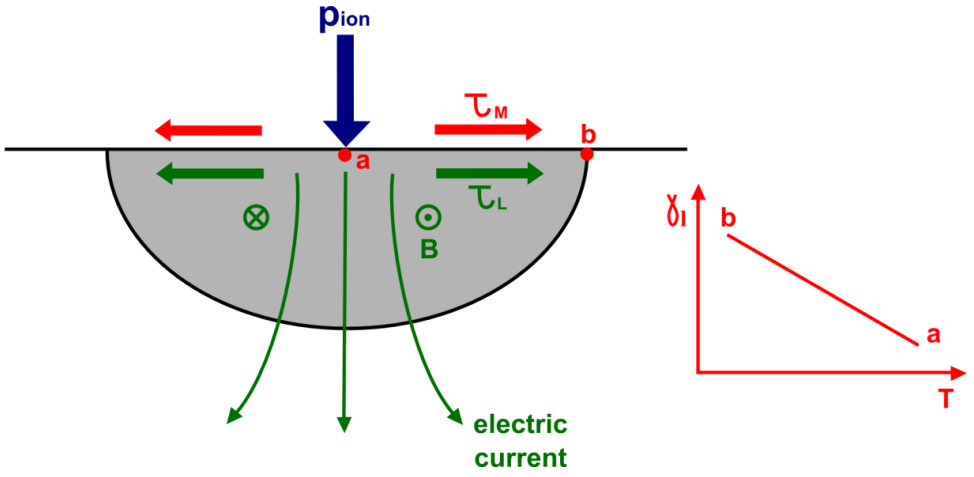

Figure 5.18 Schematic representation of the ion bombardment pressure p_{ion} (blue), the electromagnetic shear stress τ_L (green) and the surface tension gradient induced shear stress τ_M (red) acting on the molten pool surface.

A quantitative comparison is made between the ion pressure p_{ion} and the shear stresses τ_L and τ_M induced by the Lorentz force and the surface tension gradient, respectively. The ion pressure and the Lorentz force are calculated for currents of 1, 10 and 100 A, corresponding to current values at the beginning of the discharge, when craters are expected to be produced. The ion pressure is calculated using equation (2.13), assuming constant current density and an

electronic current fraction of 50 % within the cathode spot surface. The cathode fall of Pt is taken to be 16 V [80].

The radial Lorentz force per volume unit is given as

$$F_L = J \times B \tag{5.2}$$

where J is the current density normal to the surface and B is the magnetic field it generates. For a constant current density J the magnetic field B is [164]:

$$B = \frac{\mu_0}{r_m}\int_0^{r_m} Jrdr = \frac{J\mu_0 r_m}{2} \tag{5.3}$$

where μ_0 is the vacuum permeability and r_m is the radius of the molten pool. The shear stress caused by the electromagnetic force can thus be estimated as:

$$\tau_L = Jr_m B = \frac{J^2\mu_0 r_m^2}{2} \tag{5.4}$$

The shear stress caused by the surface tension gradient on the molten pool surface (Marangoni effect) is given by:

$$\tau_M = -\frac{\partial\gamma_l}{\partial r} = -\frac{\partial\gamma_l}{\partial T}\times\frac{\partial T}{\partial r} \tag{5.5}$$

At high temperatures, the temperature coefficient $\partial\gamma/\partial T$ of a binary alloy is a weighted average of the temperature coefficients of the two components [165]. Since the temperature coefficients of Pt and Ni are close (-0.307 and -0.33 $mN{\cdot}m^{-1}$ [166], respectively), the Marangoni effect in the Pt-Ni solid solution is likely to be the same as that in pure Pt. The radial temperature gradient $\partial T/\partial r$ is assumed to be constant. The temperatures at the center and at the edge of the pool are assumed to be equal to the boiling and melting points, respectively. For Pt, the Marangoni shear stress can thus be expressed as follows:

$$\tau_M = 0.307\cdot 10^{-3}\times\frac{2056}{r_m} \tag{5.6}$$

Figure 5.19 shows the ion pressure p_{ion} (full lines) and the shear stresses τ_L (dash lines) and τ_M (dash-dot line) induced by the Lorentz force and the surface tension gradient, respectively, for a molten pool having a radius between 5 and 10 µm. For a given current, the ion pressure is 2-4 orders of magnitude greater than the electromagnetic shear stress with values in the range of 10^7 to 10^{10} Pa. This is still true if higher electronic current fractions of 80-90 % are considered. The shear stress caused by the Marangoni effect is relatively low with values on the order of 10^5 Pa. Hence, the ion bombardment (or plasma pressure) is

proposed to be the principal mechanism causing the displacement of liquid metal in the molten pool and the formation of the crater depression and rim.

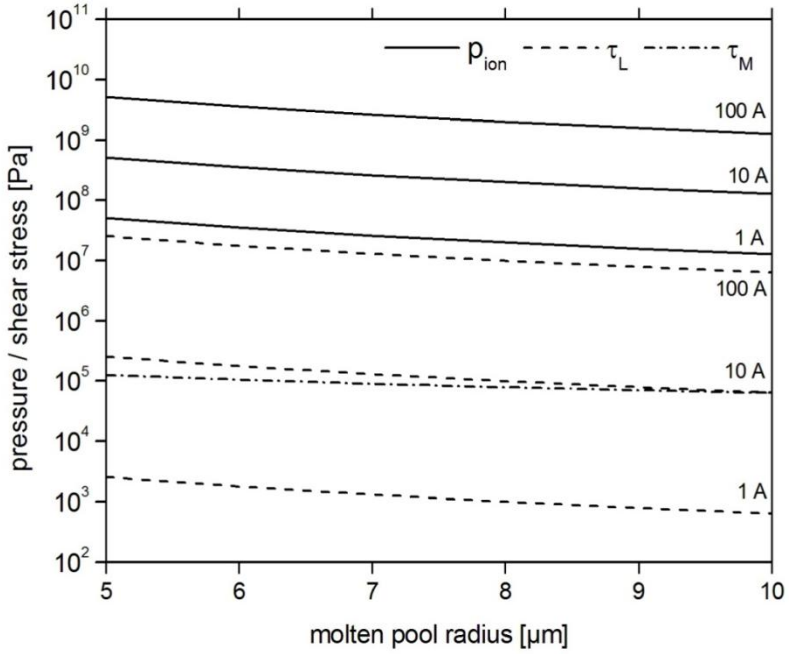

Figure 5.19 Comparison between the plasma pressure p_{ion}, the shear stress caused by the Lorentz force τ_L, and the shear stress caused by the tension surface gradient τ_M as functions of the molten pool radius.

5.4.3 Displaced Molten Volume

WLI measurements permit to determine precisely the topography of the craters (section 3.3.1). By defining appropriate reference and test masks, the volume of the crater depression (V_{down}) and of the crater rim (V_{up}) can be determined (Figure 3.4b) [121]. In the absence of severe ejection of liquid particles and vaporization (section 6.2.4.4), a large part of the molten material pushed outward from the crater center re-solidifies at the edge *of* the crater, forming the crater rim. Therefore, the volume of the crater rim should be equal to or slightly lower than that of the crater depression. Figure 5.20 shows the V_{up} and V_{down} values as a function of the estimated molten pool volume for several craters (section 5.3.3). In some cases, V_{up} is higher than V_{down}. This error may be due to the overestimation of V_{up} because of the impossibility for the WLI technique to detect the presence of covered voids at the edge of the crater. Both volume fractions, however, provide an estimation of the amount of molten material being displaced during crater formation. Comparing these volumes with the estimated molten pool volume, one can estimate that 20 to 40 % of the molten material is actually displaced under the pressure of the plasma from the crater center to the crater rim.

The remaining molten part may also be displaced but it re-solidifies at the bottom of the crater. Assuming that this ratio remains more or less the same for pure Pt as well as for other metals, the simple determination of V_{up} and V_{down} using WLI could provide a rough but realistic estimation of the molten material volume in the craters.

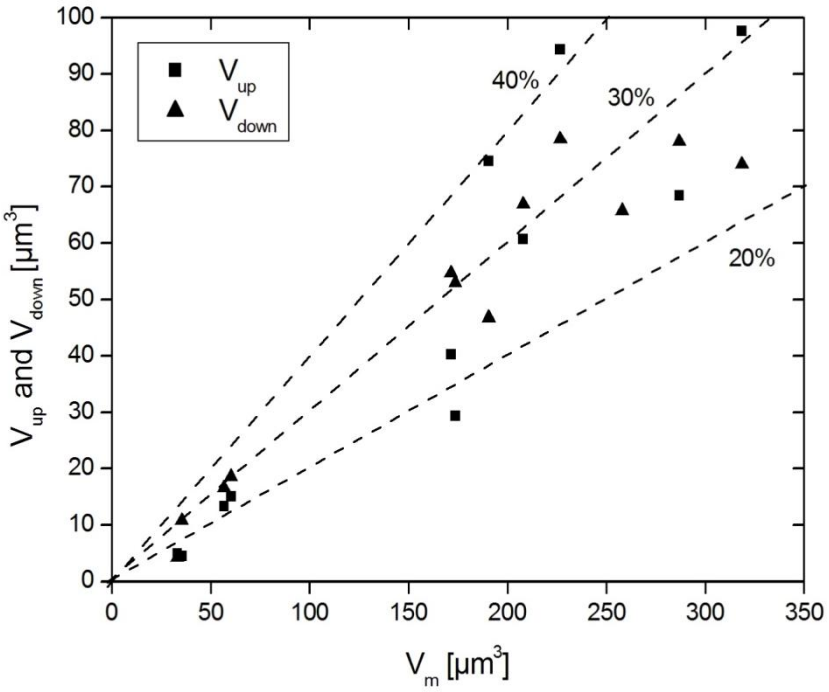

Figure 5.20 Measured V_{up} and V_{down} as a function of V_m. Between 20 and 40 % of the molten material is pushed outward from the crater center to the crater rim, where it re-solidifies.

5.5 Summary

The microstructure is a unique and authentic monitor of the material experience in the crater region. Through its analysis, new insight into the crater formation process could be gained. However, this could not be fully achieved so far due to the lack of characterization techniques permitting the analysis of such small features. The novel FIB/SEM dual beam techniques developed in this work prove to be particularly suited for the microstructure characterization of craters caused by electrical discharges on the surface of electrodes.

In craters produced on bulk metallic electrodes, no severe microstructure modification is observed, so the molten pool cannot be distinguished from the unmodified material. To solve this problem, discharges were produced on electrodes covered with thick multilayered films and craters were analyzed. Three different multilayer systems were tested: Ag/Ni, Ni/Cu and Pt/Ni. The Ag/Ni system permits to monitor the displacement of molten material in the crater

via the deformation of the layers. However, as both elements are immiscible, the molten pool cannot be clearly seen. The Ni/Cu system is miscible and the molten and mixed layers re-solidify into a coarse grained Ni-Cu solid solution as it was demonstrated by TEM and high resolution EDX analyses. This enables the monitoring of the molten region as well as the estimation of the temperature gradient in the crater. The Pt/Ni system is also miscible and proves thus to be appropriate for monitoring the molten zone. Moreover, the higher Z-contrast between Pt and Ni permits to clearly distinguish the unmodified layers from the molten region in comparison with the Ni/Cu system. For all systems, the Ag substrate below the craters does not show evidence of melting. It is also important to point out that craters produced on multilayered electrodes are similar, in shape and size, to craters produced on bulk electrodes and that these features are determined by the material present at the surface (top layer).

The Pt/Ni system was used to investigate the influence of the external pressure on crater morphology and molten pool volume. The craters formed in this system are thus comparable to those observed in pure Pt electrode. At low pressure (<4 bar), the discharge produces only a smooth melting of the surface with molten volumes in the range of 50 μm^3, and it seems that no pressure is acting on the molten surface. The formation of these craters is attributed to the breakdown phase of the ignition discharge. At high pressure (>6 bar), craters consist of one or more depressions surrounded by a rim of molten material and intermixing of the molten layers occurs. The molten volume of these craters was determined, by means of FIB cross section observations and FIB nanotomography, to be around 200-250 μm^3. Orientation analysis of the re-solidified grains realized by EBSD indicates that cooling and re-solidification of the molten pool take place under high temperature gradients (>10^9 K/m) normal to the surface. The displacement of molten material and the mixing of molten layers are proposed to be due to the ion or plasma pressure acting on the surface rather than to electromagnetic or surface tension gradient forces. Comparison between the molten pool volume and the depression and rim volumes shows that between 20 and 40 % of the molten material is displaced under the plasma pressure from the center to the edge of the crater. The craters produced at high pressure are very similar to arc cathode craters, so that their formation can be attributed to the arc phase (capacitive and/or inductive) of the discharge. Characteristic features of the low and high pressure craters are summarized in Table 5.1.

Table 5.1 Features of low and high pressure craters

external pressure	< 4 bar	> 6 bar
crater morphology	smooth undulated surface	depression and rim
rms surface roughness	50-100 nm	~200 nm
molten depth	0.4-0.5 µm	~1 µm
molten volume	~50 μm^3	200-250 μm^3
molten layer reaction	no mixing	turbulent mixing
crater type	breakdown crater	arc crater

CHAPTER 6

Thermal Analysis of the Crater Formation

The microstructure characterization presented in Chapter 5 has provided new insight into the microstructure modifications occurring at the cathode surface during crater formation. Using the combination of multilayered electrodes and FIB techniques, very useful data such as the molten depth and volume could be gained. This chapter aims to analyze these experimental data in order to determine some characteristic features of the crater formation process which are still not well known, such as the time and the power input in the cathode. The goal is to provide a reliable estimation of these values by modeling the thermal behavior of a cathode subjected to a constant heat flux of different durations.

In the first part, the melting caused by the spark is analyzed using analytical models such as the semi-continuous point and disk sources. Although numerous assumptions have to be made, the preliminary study with analytical models provides a first insight into the temperature distribution in the electrode and sheds light on how the thermal boundary conditions, the heat pulse duration and the thermal properties of the material can affect the melting of the electrode surface. The second part focuses on the crater formation process in Pt cathodes. A FEM thermal simulation is developed based on the cathode spot models existing in the literature, including phenomena such as ion bombardment, heat conduction, melting, vaporization and electron emission. For simulating the heat of the discharge, cathodes are subjected to various power input densities during time intervals of 0.1, 1 and 10 μs. Results such as the spot surface temperature, the molten depth and volume, the emitted current, and the energy loss distribution are presented and analyzed. Simulations are also performed in Pt/Ni multilayered cathodes for a better comparison with experimental results. Finally, the results of the simulation are related with the current-time characteristics of ignition discharges produced at different pressures. The effects caused by the capacitive and inductive parts of the discharge on the cathode surface as well as the wear process are discussed.

6.1 Analytical Models

6.1.1 Heat Conduction in a Semi-Infinite Electrode

The heating caused by a spark on the electrode surface can be reduced to a heat conduction problem in a semi-infinite electrode subjected to a heat source. Three heat source geometries can be considered: the point source, the disk source and a Gaussian source (Figure 6.1). The quantity of heat Q_0 can be deposited on the surface either instantaneously or over a finite time interval at a constant rate. In this second case, the source is called semi-continuous. Wang *et al.* presented a comprehensive review of these different models [167]. Because the energy is deposited within an infinitely short time, the instantaneous source overestimates the maximal temperatures reached in the electrode and reduces the influence of the thermal conductivity. Although the calculations are more complex, the semi-continuous source is more realistic when representing the behavior of the spark. Therefore, the semi-continuous models will be preferred for this study.

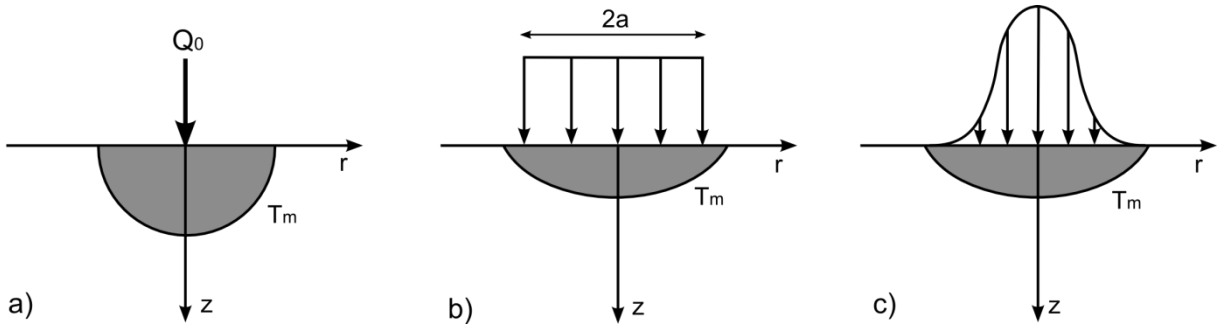

Figure 6.1 Schematic representation of the geometry of the different heat sources: a) point source, b) disk source (radius=a), c) Gaussian source.

The properties of the electrode material: the specific heat capacity c_p, the density ρ, and the thermal conductivity k are assumed to be isotropic and constant, i.e., independent of the temperature. The heart of the heat conduction problem is the heat diffusion equation:

$$\nabla^2 T = \frac{1}{\alpha}\frac{\partial T}{\partial t} \tag{6.1}$$

where $\alpha = k/\rho\, c_p$ is the thermal diffusivity of the material.

Heat conduction problems become very complicated when a part of the electrode melts because of the presence of two phases (solid and liquid) with a moving boundary (liquid/solid interface). Due to the complexity of this kind of problems, numerical calculations are required

to obtain the temperature distribution in the electrode. Therefore, in the present thermal analysis, we consider no phase change (no melting, no boiling). The entire heat input is assumed to be transferred into the electrode and there is no loss through radiation and convection at the surface.

6.1.2 Semi-Continuous Point Source

The temperature in a semi-infinite electrode subjected to a semi-continuous point source can be expressed in spherical coordinates (r=z) as [168]:

$$T(r,t) = T_0 + \frac{Q_0}{4\rho c_p (\pi\alpha)^{3/2}} \int_0^{t_0} \frac{\exp\left(\frac{-r^2}{4\alpha(t-t')}\right)}{(t-t')^{3/2}} dt' \qquad (6.2)$$

where T_0 is the initial temperature (=25°C), t_0 is the pulse duration and $t' \leq t_0$ is a dummy variable for the integration. Equation (7.2) was solved using the mathematics software Maple 8. Figure 6.2 shows the temperature distribution $T(r,z,t)$ in a Ni electrode at three different times after a pulse of heat Q_0=10 µJ and a duration t_0=1µs. At t=1.05 µs (50 ns after the end of the pulse), the temperature at r=0 reaches very high values (~7000°C). Although melting is not considered (latent heat of melting is zero), the liquid/solid interface is shown via the isotherm line $T=T_m$ (black line). The depth/radius of the melting zone exceeds 6 µm. At t=1.2 µs, the temperature has decreased below 2500°C and the melting zone is slightly smaller (~5 µm). At t=1.5 µs, the temperature has dropped below the melting point of Ni and the whole electrode is resolidified.

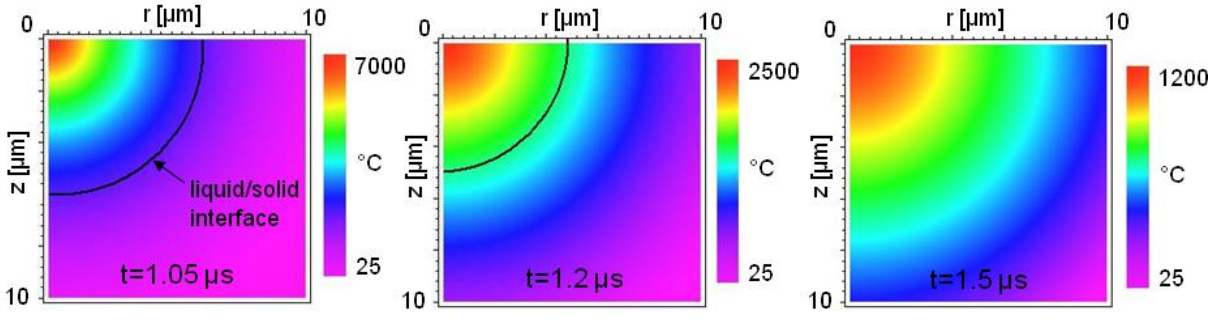

Figure 6.2 Temperature distribution in a semi-infinite electrode subjected to a semi-continuous point source (Q_0=10 µJ, t_0=1 µs) at three different times. The isotherm line $T=T_m$ (solid line) symbolizes the liquid/solid interface.

From Figure 6.2, it appears that the point heat source predicts a hemispherical molten pool with the melting depth equal to the melting radius. However, it is known from the

observations of crater cross sections presented in Chapter 5 that the molten pools are shallower. They present a spherical cap shape whereas their melting radius (r_m~10 µm) is much larger than their melting depth (z_m~1 µm). Therefore, a widely distributed heat source like the disk or the Gaussian source should be considered to better predict the shape of the molten pool. The Gaussian source is generally used to simulate the heat of a laser beam transferred to a surface [169]. There is however no indication to believe that this shape is also suitable in the case of an electric arc or a spark [151]. Actually, the cathode spot corresponds to an active current transfer region, where electrons are emitted only if sufficient heating of the surface is achieved (section 2.2.2.2). At the place where this condition is not fulfilled, no current and no heat transfer will take place. For a Gaussian source, heat is spread widely and, far from the center, the required high temperature may not be reached. It is therefore generally assumed that the current and power densities are constant over the crater radius. Hence, we believe that the disk source is more appropriate than the Gaussian source to represent the heat input of the spark.

6.1.3 Semi-Continuous Disk Source

In this case, a semi-infinite electrode subjected to a semi-continuous disk source is considered. A constant heat flux q_0 is deposited on a circular area of radius a=10 µm (~crater radius) over a period of time t_0:

$$q_0 = \frac{Q_0}{t_0 \pi a^2} \tag{6.3}$$

In cylindrical coordinates, the temperature in the semi-infinite electrode can be expressed as [168]:

$$T(r,z,t) = T_0 + \frac{Q_0}{\pi a \rho c_p t_0 (\pi\alpha)^{1/2}} \int_0^{t_0} F(t-t')\, dt' \tag{6.4}$$

with

$$F(t-t') = \frac{e^{-z^2/4\alpha(t-t')}}{\sqrt{t-t'}} \int_0^{\infty} e^{-\alpha(t-t')\lambda^2} J_0(\lambda r) J_1(\lambda a)\, d\lambda \tag{6.5}$$

where J_0 and J_1 are the Bessel functions of the first kind of order 0 and 1, respectively, and t' and λ are integration variables. It would require numerical calculation to obtain the temperature in the electrode. At r=0, i.e., along the z-axis, the integral of equation (6.5) can be simplified:

$$\int_0^\infty e^{-\alpha(t-t')\lambda^2} J_0(\lambda r) J_1(\lambda a)\, d\lambda = \frac{1 - e^{-a^2/4\alpha(t-t')}}{a} \tag{6.6}$$

Because phase changes are not considered in the present model, we calculate the power density P_m required for heating the center of the disk only up to the melting point, i.e., to reach the temperature T_m at the position r=0, z=0. Using equations (7.3)-(7.6), the melting power density is given as:

$$P_m = \frac{(T_m - T_0)\rho c_p (\pi\alpha)^{1/2}}{\int_0^{t_0} G(t-t')dt'} \tag{6.7}$$

where

$$G(t-t') = \frac{1 - e^{-a^2/4\alpha(t-t')}}{\sqrt{t-t'}} \tag{6.8}$$

Equations (6.7) and (6.8) were solved using Maple 8. Figure 6.3 shows the melting power density P_m as a function of the pulse duration t_0 for various metals employed as contact or electrode materials. This kind of representation - power density vs. interaction time - is well-known in the field of laser processing of materials [169]. For the selected metals and for pulse durations between 10 ns and 1 ms, the melting power densities range from 10^{10} to 10^{12} W/m^2 and they increase as the pulse duration becomes shorter. This result is quite obvious and means that when the melting point has to be reached within a shorter time, higher power is required. For longer pulses (t_0>10 µs), however, P_m remains more or less constant. It is interesting to see that, in spite of lower melting points, a higher power density is required to heat Ag and Cu up to their melting point, than for Pt and Ni. A material like Ir, having high melting point (T_m=2446°C) and moderate thermal conductivity (k=147 W/m·K) has a higher P_m than that of Cu and Ni for short pulse durations (t_0<1 µs). Between 1 and 10 µs, however, the curves intersect and it becomes easier to melt Ir than Cu and Ag, which both have relatively low melting points (T_m=1084 and 962°C, respectively) but very high thermal conductivities (k=401 and 429 W/m·K, respectively). The same comment applies to the case of Al compared to Ni and Pt. Therefore, it is clear that the melting point and the thermal conductivity have more or less influence on the melting susceptibility of the electrode depending on the time scale.

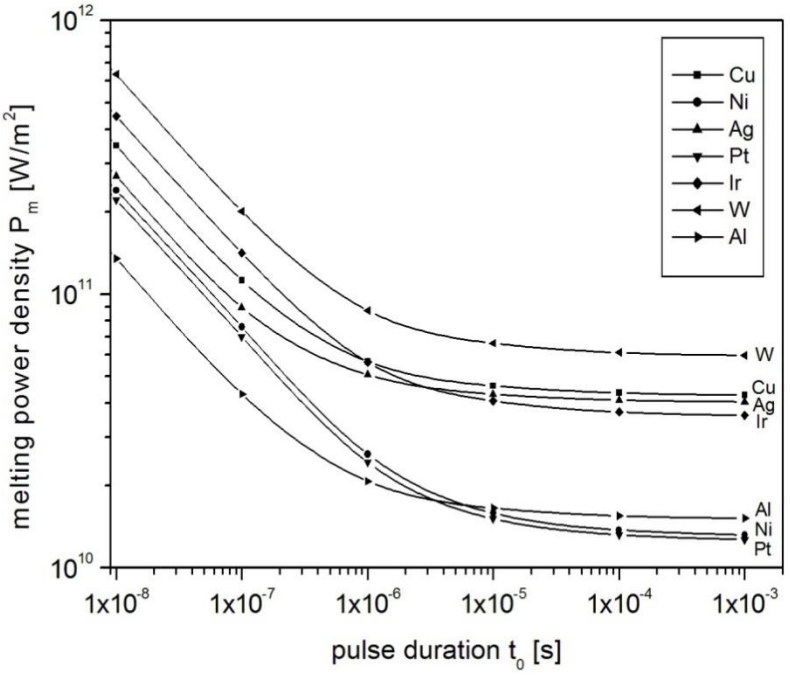

Figure 6.3 Melting power density as a function of the pulse duration for various metals currently employed in electrode or electrical contact applications.

For a better visualization of this effect, the melting power density P_m is calculated for four "virtual" materials combining extremely high/low melting points with extremely high/low thermal conductivities (Figure 6.4). The high/low thermal conductivities are 500 and 10 W/m·K, respectively, while the high/low melting points are 4000°C and 200°C, respectively. These values are not completely unrealistic and are close to those encountered for some metals. The density and the specific heat capacity are taken to be those of Pt for the four materials. It is obvious that the material combining both the high melting point and the high thermal conductivity presents the greater melting power density. Likewise, the material with both low T_m and low k shows the lower P_m values. The two intermediate cases, namely the material with low k and high T_m and the material with high k and low T_m are more interesting. For a short heat pulse (t_0<1 µs), the material with the high melting point prevails over the one with the high conductivity. As the pulse becomes longer (t_0>10 µs), the material with the high conductivity becomes more difficult to melt than the one with the high melting point. Like in the cases of Ir with Cu or Ag, and Al with Pt or Ni (Figure 6.3) the transition occurs for a t_0 situated between 1 and 10 µs. These results indicate that there are two possible strategies to prevent melting depending on the duration of the heat pulse t_0. An electrode with high melting point is favorable when t_0<1 µs, whereas it would be better to have an electrode with high thermal conductivity when t_0>10 µs.

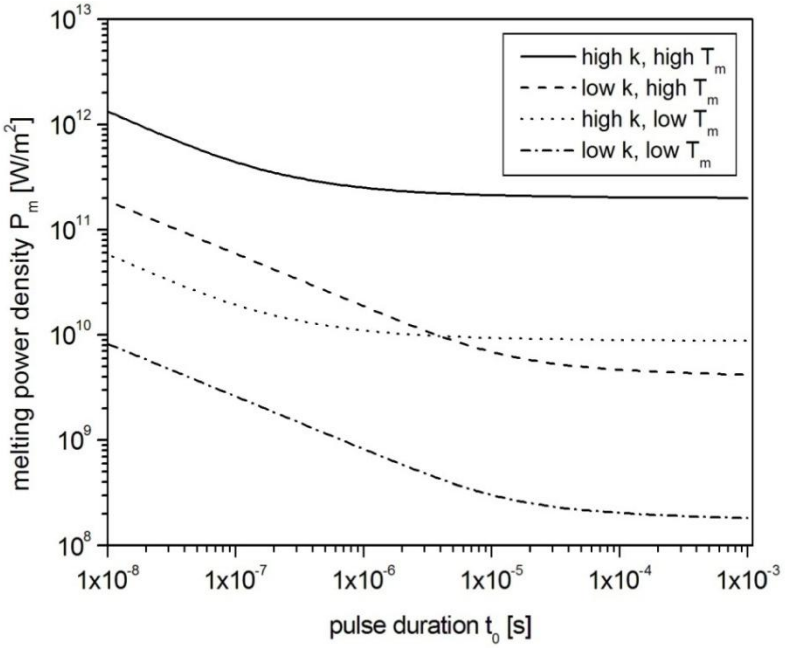

Figure 6.4 Melting power density as a function of the pulse duration for four "virtual" materials; high k=500 W/m·K; low k=10 W/m·K; high T_m=4000 °C; low T_m=200 °C

Moreover, the results point out that the pulse duration has a strong influence on the value of the melting power density. In other words, the same temperature at the surface of the electrode (or the same melting depth) can be reached by different power input densities depending on the time of interaction between the spark and the electrode. Similarly, the same power input can lead to completely different effects on the electrode surface (slight heating, melting, boiling) depending on the pulse duration. Therefore, a reliable determination of the power input involved in the crater formation will require to know, at least approximately, the time of formation of the crater.

6.2 FEM Thermal Simulation

The previous thermal analysis focused on analytical solutions for heat conduction problems in a semi-infinite electrode. For solving these problems without carrying out numerical calculations, numerous assumptions were made (no phase change, constant properties, etc.). The results of the analytical models pointed out how thermal properties such as melting point and thermal conductivity can affect the melting behavior of the electrode and how it is important to know the time of formation of the crater in order to estimate the corresponding power input. For a better description of crater formation, however, melting, vaporization as well as electron emission on the electrode surface should be considered.

The melting and vaporization of an electrode heated by a flux is a Stefan-like problem with moving boundaries [170]. This kind of thermal problem can be solved using an enthalpy method combined with Kirchhoff and coordinate transformations as demonstrated by Hunter [171]. Rossignol [172] and Abbaboui [173] employed this method in order to predict characteristic information related to the liquid and vapor formation for various materials submitted to different heat fluxes.

In this part, a thermal simulation by finite elements method (FEM) is developed considering melting, heat conduction, vaporization and electron emission at the surface. The simulation aims to determine the temperature distribution in the electrode, the extent of molten and vaporized material and the energy balance at the surface during crater formation.

6.2.1 Description of the Physical Model

The physical model used to simulate crater formation is based on the modeling of cathode spot phenomena in vacuum [57]. The arc cathode region has been studied with stationary or dynamic models by numerous authors such as, among others, Coulombe [37, 102], Rossignol [86], Zhou [35], Rethfeld [33], He [174], Mitterauer [88], Klein [85], and Messaad [175]. Most of these studies consider the entire cathode region divided into three zones: the first zone is the cathode surface itself where heating, vaporization and electron emission take place; the second zone is the cathode sheath where emitted electrons are accelerated towards the ionization zone and positive ions are accelerated towards the cathode; the third zone is the ionization zone where vaporized atoms are ionized by electrons.

Our model includes the relevant features reported in the aforementioned works. However, it is limited to the bulk and the surface of the cathode. Phenomena occurring in the cathode sheath and in the ionization zone are not considered. The cathode surface is assumed to be heated exclusively by ion bombardment whereas electron emission, vaporization, melting and conduction into the bulk are the cooling mechanisms (Figure 6.5).

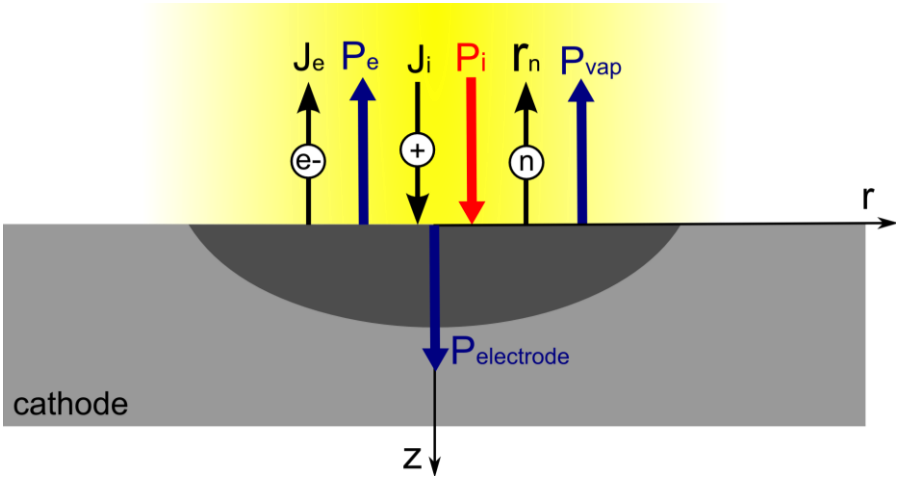

Figure 6.5 Schematic representation of the cathode spot model used in the thermal simulation. J_e, J_i and Γ_n are the electron current, ion current and neutral flux densities, respectively. P_e, P_i and P_{vap} are the corresponding electron emission, ion and vaporization power densities. $P_{electrode}$ corresponds to the power lost in the electrode via conduction and melting.

6.2.1.1 Heat Conduction and Melting

Heat conduction into the electrode and solid-liquid phase transition are considered in the heat diffusion equation:

$$\nabla \cdot (k \cdot \nabla T) + \dot{q}_{SL} = \rho \cdot c_p \frac{\partial T}{\partial t} \tag{6.9}$$

where k is the thermal conductivity, c_p is the specific heat capacity, and ρ is the density. These properties are all temperature dependent in the simulation. The term $\dot{q}_{SL}$ is the power per unit of volume involved in the solid-liquid phase transition, and can be defined by [151]:

$$\dot{q}_{SL} = L_m \rho \frac{\partial \left[0.5 erfc\left(\frac{T - T_m}{\Delta T_m}\right)\right]}{\partial t} \tag{6.10}$$

where L_m is the latent heat of melting, *erfc* is the complementary error function, T_m is the melting temperature and ΔT_m is a small temperature interval to smooth the solid-liquid transition (ΔT_m was selected to be 10 K). Note that when the temperature increases (solid-liquid transition), $\dot{q}_{SL}$ is negative and heat is consumed, whereas when the temperature decreases (liquid-solid transition), $\dot{q}_{SL}$ is positive and heat is produced.

6.2.1.2 Vaporization

The flux density of vaporized atoms Γ_n is calculated using the Langmuir formula. It is related to the equilibrium vapor pressure of the material p_v as shown in equation (2.12). The values of the constants A, B and C are taken from [176]. The power density associated with

the vaporization of atoms is calculated using equation (2.23). The vaporized atom flux and the corresponding power density are calculated as a function of the surface temperature T_s for the case of platinum (Figure 6.6). It is assumed that the liquid metal surface is in equilibrium with its vapor. Therefore, the cathode surface temperature under the spot is related to the metallic plasma pressure via the equilibrium vapor pressure $T_s=T_s(p_v)$.

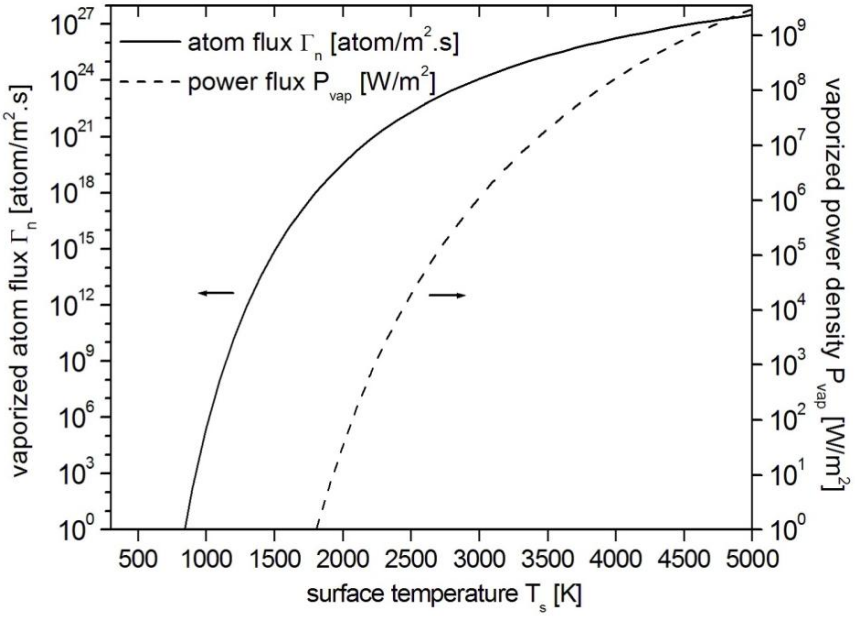

Figure 6.6 Vaporized atom flux Γ_n and corresponding vaporization power density P_{vap} as functions of the surface temperature T_s for the case of Pt.

6.2.1.3 Electron Emission

Cathodes are either classified as thermionic or non-thermionic electron emitters. Thermionic cathodes (or hot cathodes) are made of refractory materials such as tungsten and can sustain the high temperatures needed for thermionic emission. The electron emission current of hot cathodes can be accurately predicted by the Richardson-Dushman equation (2.8) with the Schottky correction (2.9). Non-thermionic cathodes (or cold cathodes), made of non-refractory materials such as Cu or Ag cannot sustain such high temperatures. The electron emission mechanism of cold cathodes is expected to be thermo-field, i.e., electrons are emitted under the combined action of high surface temperatures T_s and high surface field strengths E_s. The thermo-field current is best predicted by the Murphy and Good equation (2.10). Since Pt can be classified as a cold cathode (see Appendix A), the electron emission current must be calculated using the Murphy and Good formalism.

The treatment of this equation is very complex and requires multiple numerical integrations that cannot be performed directly in the simulation. Therefore, an approximation

is necessary. The Murphy and Good equation was solved numerically[1] in the case of Pt for temperatures ranging from 2000 to 5000 K and for electric field strengths ranging from 10^9 to 10^{10} V/m (Figure 6.7).

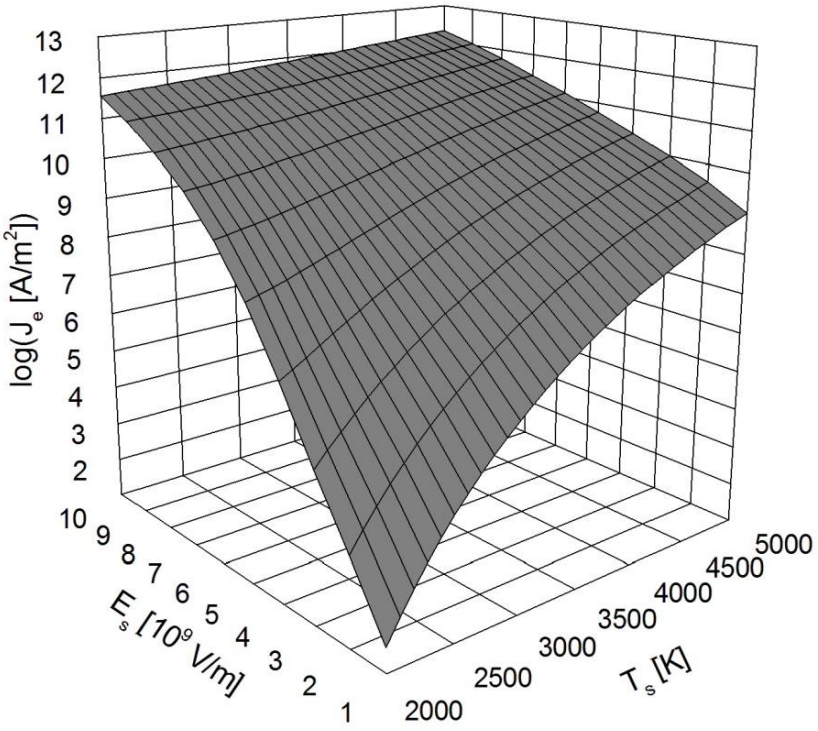

Figure 6.7 Thermo-field current density calculated with the Murphy and Good equation as a function of the temperature and surface electric field strength for Pt (ϕ=5.65 eV).

Because the simulations are performed under constant values of ion power density, the ion current and the electric field strength are constant and the electron current density can be expressed as a function of the surface temperature $J_e(T_s)$. The function $\log(J_e(T_s))$ is then fitted with a polynomial function of order n=3 for each value of E_s and introduced in the simulation (Figure 6.8). The polynomial constants A_0, B_1, B_2 and B_3 are displayed in Appendix B. The mean deviation from the exact results calculated with the Murphy and Good equation is found to be less than 0.5 % in the temperature and electric field strength ranges considered. Knowing the electron emission current density J_e, the associated cooling power density P_e, also known as Nottingham cooling, can be calculated using equation (2.22).

[1] The author greatly acknowledges Dipl.-Ing Meik Sacher, Lehrstuhl für elektrische Geräte und Anlage, TU Ilmenau for the numerical calculation of the Murphy and Good equation for Pt.

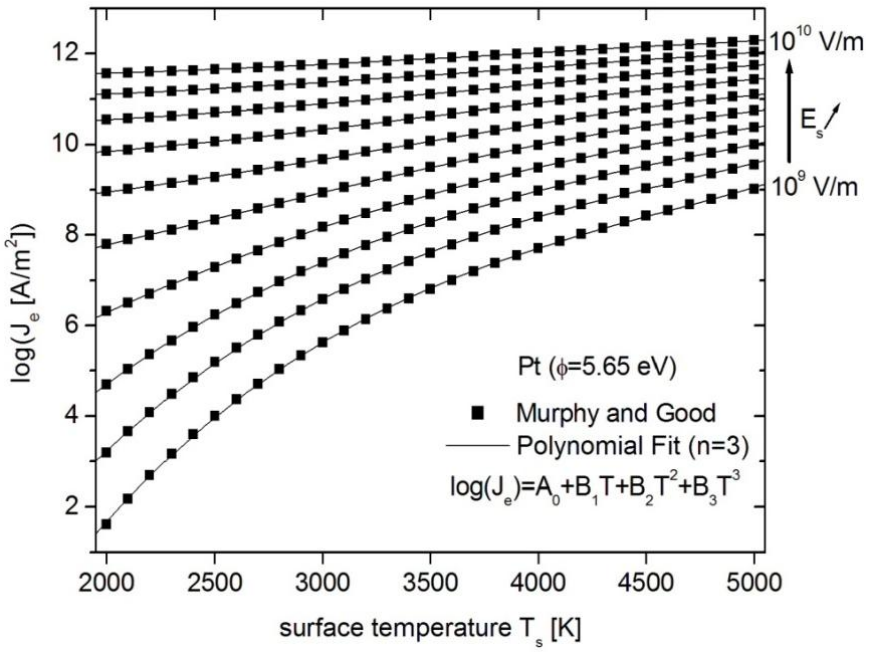

Figure 6.8 Fitting of $\log(J_e(T_s))$ with polynomial functions of order n=3 for E_s values between 10^9 and 10^{10} V/m.

6.2.1.4 Ion Bombardment

Ion bombardment is the only heating contribution in the present model because other heating mechanisms such as back-diffused electrons, returning atoms, radiation and Joule heating can be neglected (section 2.3.2.1). The ion power density P_i is the product of the ion current density J_i by the mean energy delivered by each ion impacting the cathode U_i as described in equation (2.17). The mean ion energy is composed of the thermal, kinetic, neutralization and condensation energies, and it can be written as:

$$U_i = \frac{5k_B T_i}{2e} + \frac{k_B T_e}{2e} + U_c + E_i - \phi' + W_{ev} \tag{6.11}$$

where U_c is the cathode fall, E_i is the neutralization (or ionization) energy reduced by the modified work function ϕ' (equation (2.9)), W_{ev} is the condensation (or vaporization) energy, T_i and T_e are the ion and electron temperatures at the cathode sheath edge. According to Coulombe [37], the ion temperature can be assumed constant and equal to the cathode surface temperature. Thus, in our model we take T_i=T_b^{Pt}=4100 K. The electron temperature is assumed to be higher than the ion temperature and set to be T_e=8000 K according to the ignition discharge plasma temperature reported in [24]. Note that the two first terms of equation (6.11) are small compared to the other terms so that the assumptions made for T_i and T_e do not strongly affect the value of U_i.

6.2.1.5 Surface Electric Field

The electric field strength at the cathode surface E_s is related to the ion current density J_i via the Mackeown equation (2.11). In our model, we use the equation form proposed in [88]:

$$E_s = \left(\frac{8 \cdot Z_i \cdot m_i \cdot J_i^2 \cdot U_c}{e \cdot \varepsilon_0^2} \right)^{1/4} \tag{6.12}$$

where m_i is the ion mass and Z_i is the mean ion charge assumed to be equal to 1 (single ionization).

6.2.2 Geometry and Boundary Conditions

The simulation is performed in cylindrical coordinates (r, z). The geometry of the electrode and the boundary conditions are schematically shown in Figure 6.9.

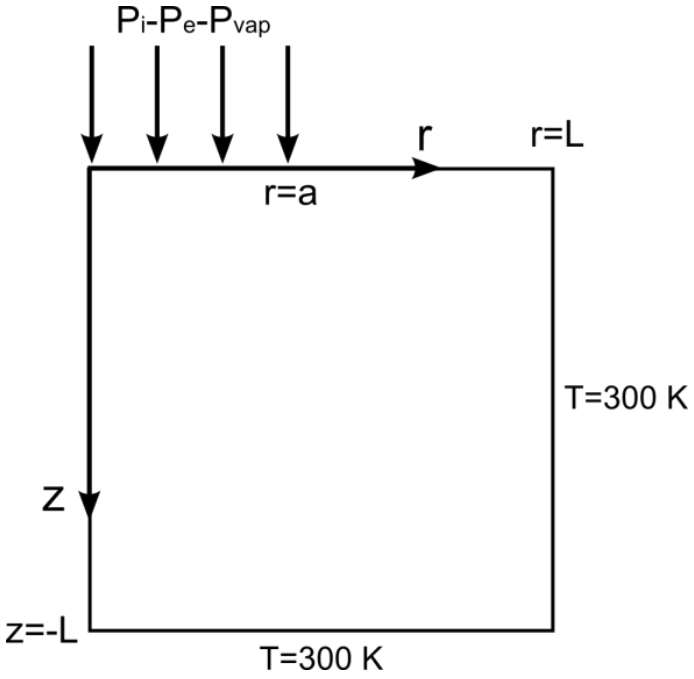

Figure 6.9 Schematic representations of the geometry and boundary conditions of the simulation with a=10 µm and L=100 µm.

The radius and height of the simulated electrode are defined as being equal to L. The temperature at the side (r=L) and at the bottom (z=-L) of the electrode is maintained constant at the initial temperature T=300 K. This fixed temperature can strongly affect the results when L becomes smaller than 30-50 µm. Here, we choose L large enough (L=100 µm) to guarantee that the size of the electrode does not induce errors in the calculation of the temperature (Appendix C). The power balance at the cathode surface is given by the ion power density P_i

reduced by the electron emission and vaporization power densities P_e and P_{vap} over a disk of radius a=10 µm, which corresponds to the maximal crater size observed experimentally. The pulse of heat is deposited during the time t_0. The remaining part of the surface is assumed to be adiabatic. The boundary conditions can be summarized as follows:

$$T|_{r=L} = T|_{z=-L} = 300\ K$$

$$-k\frac{dT}{dz}\Big|_{\substack{0<r<a \\ z=0}} = P_i - P_e(T_s) - P_{vap}(T_s)$$

$$-k\frac{dT}{dz}\Big|_{\substack{a<r<L \\ z=0}} = 0$$

6.2.3 Simulation Procedure

The simulations are carried out in a transient regime for given (P_i, t_0) couples in the case of a Pt cathode. According to the previous analytical results (Figure 6.3), the ion power densities P_i are chosen between 10^{10} and 10^{12} W/m^2. The time of interaction or pulse duration t_0 is taken to be 0.1, 1 and 10 µs. For a given value of P_i, the mean ion energy U_i and the surface electric field strength E_s are calculated. Since U_i is related to E_s via the modified work function ϕ' in equation (6.11), and E_s is related to U_i via the ion current density J_i in the Mackeown equation (6.12), both parameters are coupled and must be determined simultaneously. We compute the values of U_i and E_s using an iterative process (Appendix D). Figure 6.10 shows the values of U_i and E_s as a function of P_i for Pt^{1+} ions. Knowing the value of E_s, the modified work function ϕ' as well as the constants A_0, B_1, B_2, and B_3 of the polynomial function used to predict the electron emission current density can be determined.

Finally, all the parameters mentioned above are introduced in the FEM simulation together with the material properties of the cathode (Appendix E). The simulation is performed with the finite element software FlexPDE 5. The software solves the partial differential equation (6.9) and calculates the field of temperature in the electrode as a function of the time T=f(r,z,t). Furthermore, parameters derived from the temperature field such as melting depth/radius, vaporization rate, electron emission current and energy balance are determined.

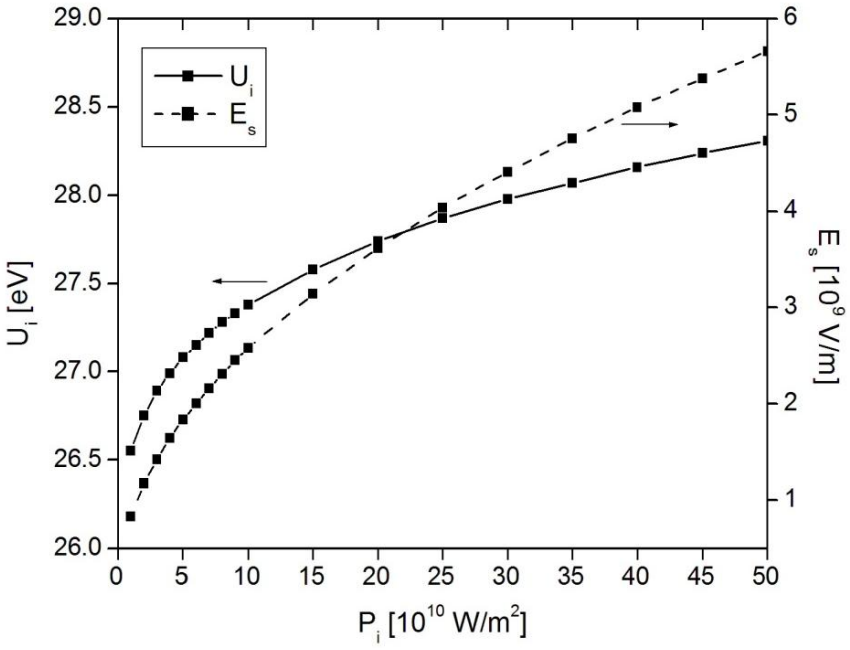

Figure 6.10 Mean ion energy U_i and surface electric field E_s as a function of P_i for the case of Pt^{1+} ions.

6.2.4 Results in Bulk Pt

6.2.4.1 Spot Temperature

Figure 6.11 shows the spot temperature T_{spot} as a function of the ion power density P_i for different pulse durations t_0=10, 1 and 0.1 µs. The spot temperature is defined as the mean temperature over the spot surface at the end of the pulse, i.e., at time $t=t_0$:

$$T_{spot} = \frac{1}{\pi a^2} \int_S T(r, 0, t_0) \cdot dS \tag{6.13}$$

where S is the area of the spot. As it was pointed out previously with the help of analytical models, the power input density required to reach a certain temperature increases as the pulse duration becomes shorter. This is the reason why the curves are shifted to the right as t_0 decreases. For example, the ion power density necessary to reach a spot temperature of 4000 K is approximately 4×10^{10} and 7×10^{10} W/m^2 for t_0=10 and 1 µs, respectively, while it amounts to 18×10^{10} W/m^2 for t_0=0.1 µs. For all pulse durations, the spot temperature first increases rapidly before reaching a maximal value of ~5000 K at high ion power densities, likely due to the important cooling at the surface. The exact contribution of the different cooling mechanisms will be discussed at the end of this section.

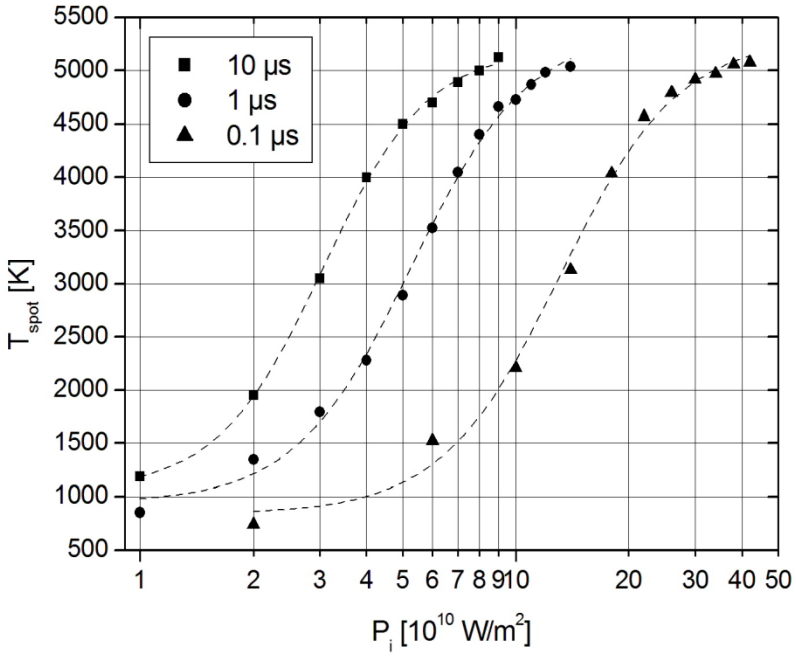

Figure 6.11 Spot temperature T_{spot} as a function of ion power density P_i for t_0=10, 1 and 0.1 µs.

6.2.4.2 Molten Depth and Molten Volume

Because the same ion power density can lead to completely different surface temperatures depending on the time of interaction considered, the melting depth and volume are not plotted as a function of P_i but as a function of the spot temperature (Figure 6.12). Hence, the effect of the different pulse durations on the melting behavior of the cathode surface can be better compared. The molten pool of the crater is assumed to present a spherical cap shape and the molten volume V_m is calculated using equation (5.1) based on the simulated molten depth z_m and molten radius r_m. The results show that for a given spot temperature, the longer the pulse duration is, the larger the associated molten depth/volume becomes. This is due to the increase of the thermal diffusion length $(2\alpha \cdot t_0)^{1/2}$ with the time of interaction t_0, where α is the thermal diffusivity coefficient. In other words, for a short pulse, diffusion is low and the heat is highly concentrated on the surface, while for a long pulse the heat penetrates deeper into the bulk, leading to a larger amount of molten material. The gray stripe in Figure 6.12 symbolizes the values of molten depths (~1 µm) and volumes (200-250 µm^3) determined experimentally in craters produced at high pressures (section 5.3). The corresponding surface spot temperature differs strongly depending on the pulse duration. For t_0=10 and 1 µs, the corresponding T_{spot} lie around 2000 K and 2500 K, respectively, whereas for t_0=0.1 µs it is much higher, in the range of 4500 K.

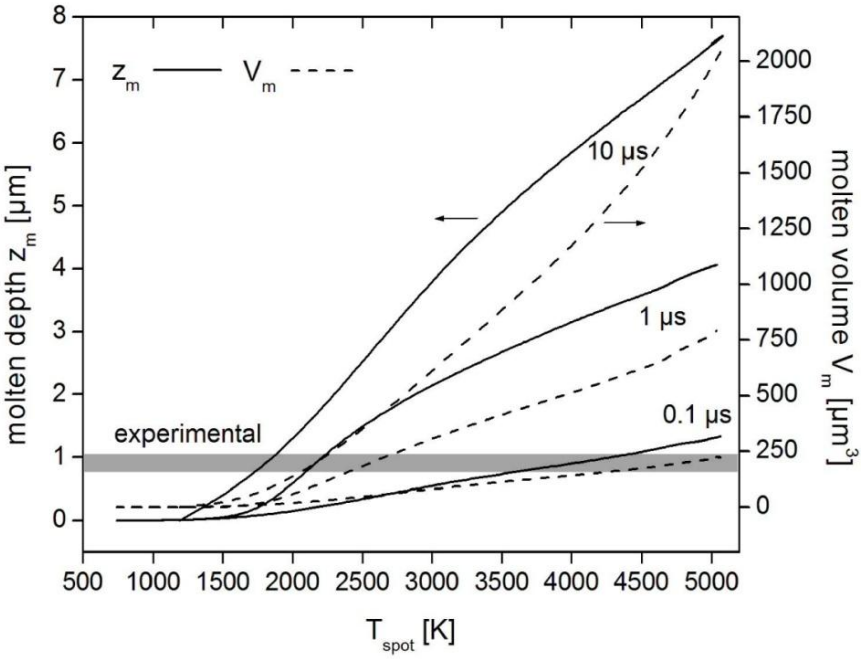

Figure 6.12 Molten depth z_m (left axis) and molten volume V_m (right axis) as a function of T_{spot} for t_0=10, 1 and 0.1 µs. The gray stripe represents the experimental data of z_m (~1 µm) and V_m (~200-250 µm^3).

6.2.4.3 Electronic Current Fraction

The electronic current fraction s is defined as the ratio of electronic to total current densities at the cathode surface:

$$s = \frac{J_e}{J} = \frac{J_e}{J_i + J_e} \tag{6.14}$$

where J_i remains constant through the relationship with the ion power density (J_i=P_i/U_i) and J_e is the mean electron current density over the spot at time t=t_0. Figure 6.13 shows the evolution of s as a function of the spot temperature for the three pulse durations. The electron emission becomes significant from a spot temperature of ~3000 K and increases to reach 70-80 % of the total current for T_{spot}=5000 K. The slight difference between the three curves is due to the different temperature distributions within the spot surface. Indeed, the temperature within the spot is more homogeneous for a short pulse because heat diffusion is less important than for a long pulse. Since the electron emission current is not linear with the temperature, for a same spot temperature, the electron current density is slightly higher for t_0=0.1 µs than for t_0=10 or 1 µs.

The formation of an arc discharge is possible only if a sufficient flux of emitted electrons can be achieved. For non-refractory cathodes like Pt, these electrons are emitted in the thermo-field regime under the combined action of high surface temperatures and electric

fields achieved mainly by ion bombardment. Once emitted from the cathode surface, the electrons are accelerated through the cathode sheath without collisions to the ionization zone, where inelastic collisions with vaporized atoms occur, resulting in the production of ions. The maximum kinetic energy taken by the electrons in the cathode sheath corresponds to the cathode fall voltage and is therefore around 10-20 eV. For this energy range, only single-ionization can take place upon electron impact [177]. Therefore, the flux of ions produced by the ionization of vaporized atoms cannot be higher than the electron flux that generates it. Consequently, a restraining criterion for the existence of an arc discharge and the formation of a cathode spot crater is that $J_e \geq J_i$ or $s \geq 0.5$. According to the results of the simulation, this condition is fulfilled for a spot temperature equal to or higher than 4500 K.

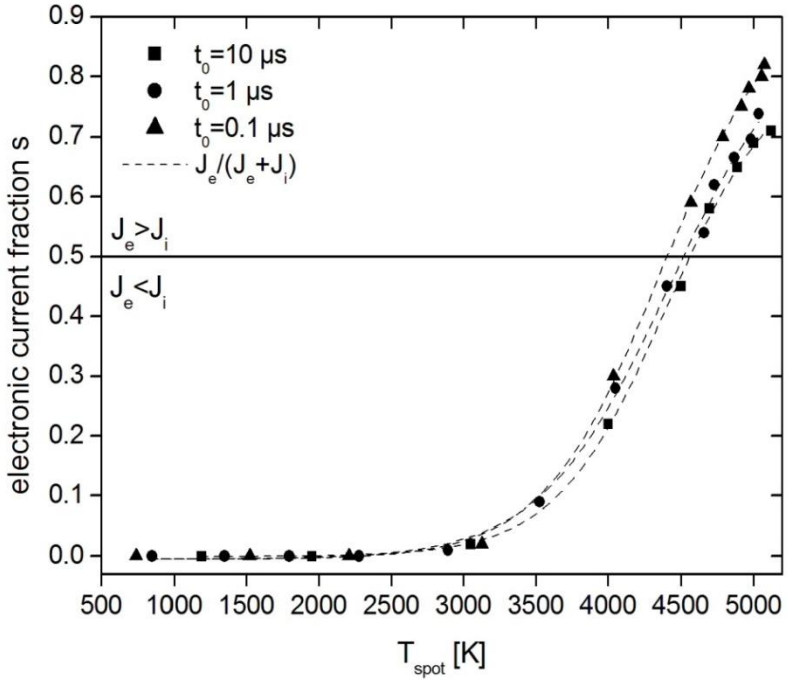

Figure 6.13 Electronic current fraction $s=J_e/(J_e+J_i)$ at the cathode surface as a function of the spot temperature for t_0=10, 1 and 0.1 µs. The line s=0.5 corresponds to $J_e=J_i$.

It is now possible to compare the theoretical criterion $T_{spot} \geq 4500$ K with the molten depths and volumes shown in Figure 6.12 to evaluate the most probable duration of crater formation. The melting depth/volume and ion power density corresponding to the criterion $T_{spot} \geq 4500$ K are summarized in Table 6.1 for the different pulse durations. The best agreement with the experimental molten depth/volume (~1 µm/200-250 µm^3) is obtained for pulse duration t_0=0.1 µs. Longer times of interaction between the arc and the cathode surface such as for t_0=10 and 1 µs would lead to much larger molten zones and consequently deeper

craters, which are not observed experimentally. Therefore, we estimate the time of formation of the crater to be on the order of 0.1 µs, whereas the ion power density responsible for the strong heating of the surface must be higher than 2×10^{11} W/m^2.

Table 6.1 Molten depth z_m, volume V_m and ion power density P_i corresponding to the condition $T_{spot}\geq4500$ K for different pulse durations.

	t_0=10 µs	t_0=1 µs	t_0=0.1 µs
z_m [µm]	≥7	≥3.5	≥1
V_m [µm^3]	≥1500	≥600	≥200
P_i [W/m^2]	$\geq5\times10^{10}$	$\geq8\times10^{10}$	$\geq2\times10^{11}$

6.2.4.4 Comparison between Molten and Vaporized Volumes

Figure 6.14 shows the melting volume V_m and the volume of vaporized material V_{vap} as functions of ion power density, assuming a crater formation time of 0.1 µs. The experimental molten volume values (200-250 µm^3) are reached for P_i values on the order of 4×10^{11} W/m^2. As the ion power input density is further increased, the simulated molten pool volume does not rise due to the important electron emission cooling at the surface, which limits the melting depth. Larger melting volumes can therefore be obtained only if greater spot radii are considered (a>10 µm).

The vaporized volume is defined as the quantity of atoms emitted from the surface within the spot area S during the time t_0:

$$V_{vap} = \int_S \int_{t_0} \Gamma_n \cdot dS \cdot dt \tag{6.15}$$

This volume corresponds to the maximum vaporization rate when re-condensed ions and back-reflected atoms are not taken into account. The volume of vaporized material represents less than 0.5 % of the molten volume and must be on the order of 1 µm^3 for the craters observed. The net flux of atoms, contributing to the erosion, is about 80 % of the emitted flux in vacuum [101]. However, as the discharges are produced at pressures of several bars, the cathode spot plasma should be confined close to the surface and high atom back-reflection and ion re-condensation are expected. Consequently, the net volume of vaporized atoms is much smaller than the volume emitted from the surface. Therefore, under high ambient pressures as in our case, vaporization does not contribute to the net erosion of the

electrode, which is in accordance with the conclusion drawn from experimental investigations of the electrode wear under different atmospheres [100].

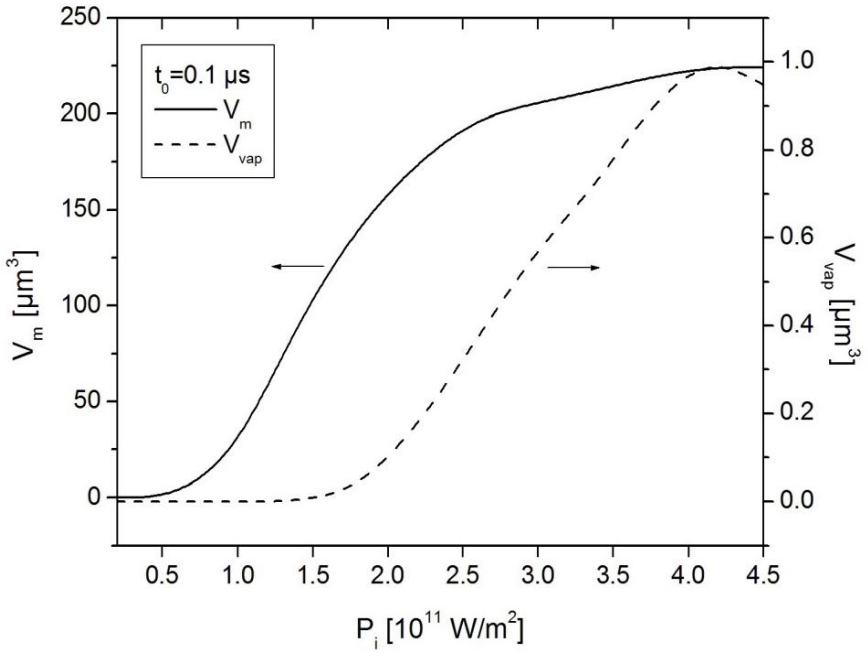

Figure 6.14 Melting volume V_m (left axis) and vaporized volume V_{vap} (right axis) as a function of the ion power density for t_0= 0.1 µs. The volume of vaporized material represents less than 0.5 % of the molten volume.

6.2.4.5 Total Current

The total current, defined as the sum of the electronic and ionic currents, is shown in Figure 6.15 as a function of the ion power density for various spot radii ranging between 5 and 10 µm, and for t_0=0.1 µs. These radii correspond to typical crater radii observed experimentally on bulk Pt or multilayered Pt/Ni electrodes. Two regions can be distinguished in this diagram. At low ion power densities (P_i<1.5×10^{11} W/m^2) the electron emission current is negligible due to the low spot temperature (<3500 K). In this range, the current is only carried by ions, which is unrealistic because the criterion $J_e \geq J_i$ is not fulfilled. At ion power densities higher than 2×10^{11} W/m^2, the electron emission current becomes significant ($J_e \sim J_i$) and the total current grows rapidly as ion power density and spot surface temperature increase. For the value of P_i previously estimated to be on the order of 4×10^{11} W/m^2, the total current varies in the range from 5 to 25 A, depending on the spot radius considered.

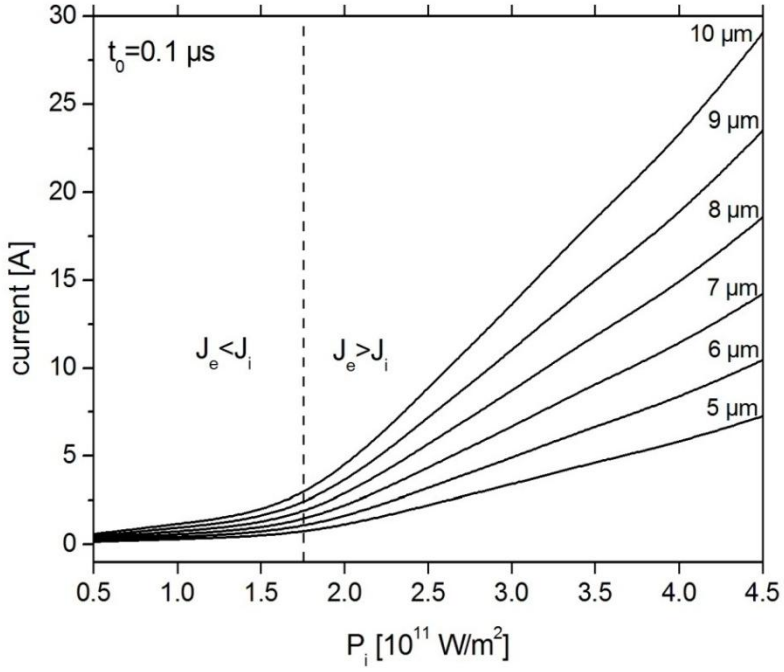

Figure 6.15 Total current as a function of the ion power density for spot radii varying between 5 and 10 µm.

6.2.4.6 Energy Loss Distribution

In this section, the contribution of the different cooling mechanisms is presented. Total heat losses by vaporization E_{vap} and by electron emission cooling E_e at the cathode surface are given by:

$$E_{vap} = \int_S \int_{t_0} \mathrm{P_{vap}} \cdot \mathrm{dS} \cdot \mathrm{dt} \tag{6.16}$$

$$E_e = \int_S \int_{t_0} \mathrm{P_e} \cdot \mathrm{dS} \cdot \mathrm{dt} \tag{6.17}$$

where P_{vap} and P_e are given by equations (2.23) and (2.22), respectively. The heat dissipated through melting E_m is determined by:

$$E_m = V_m \left(\int_{300\ K}^{T_m} \rho c_p \, dT + L_m \right) \tag{6.18}$$

where V_m is the volume of molten material calculated with equation (5.1) and the term in brackets corresponds to the energy required to heat up to the melting point and melt a unit of volume of material. The heat lost in conduction E_{cond} is defined as the difference between the heat input delivered by the ions E_{ion} and the sum of the other cooling contributions:

$$E_{cond} = E_{ion} - \left(E_{vap} + E_e + E_m\right) \tag{6.19}$$

The heat loss distribution is shown in Figure 6.16 as a function of the ion power density for pulses of 10 µs and 0.1 µs. The maximum values of ion power density in both diagrams correspond to a spot surface temperature of ~5000 K. Conduction into the bulk is the predominant cooling mechanism. It is the only heat loss mechanism at low power densities and its proportion decreases to ~40-50 % at high ion power densities, depending on the pulse duration. The proportion of heat dissipated in the melting phase transition is 5 % and 15 % of the total energy for t_0=10 and 0.1 µs, respectively. Although molten volumes V_m are larger for t_0=10 µs than for t_0=0.1 µs (Figure 6.12), melting shows a higher cooling contribution in the case of a short pulse because diffusion phenomena are less important and the loss through conduction is lower. The sum of the conduction and the melting contributions, corresponding to the heat lost in the cathode bulk, is the same for both pulse durations and represents ~55 % of the total energy at high ion power densities.

The emission of electrons is the second most important cooling mechanism after conduction. Because high surface temperatures are required to emit electrons, the associated Nottingham cooling becomes efficient only at P_i=3×10^{10} and 2×10^{11} W/m^2 for t_0=10 and 0.1 µs, respectively, and its contribution grows rapidly to reach ~40 % at high ion power densities. This is the reason why the spot temperature and the melting depth/volume cannot rise indefinitely but reach limit values when P_i is further increased (Figures 6.11 and 6.14). The important electron emission cooling is promoted by both the elevated temperatures and the high electric field strengths at the surface. Finally, the heat distribution diagrams show that vaporization plays a minor role compared to the other cooling mechanisms. It represents less than 4 % and 0.5 % of the total heat loss for t_0=10 and 0.1 µs, respectively. The negligible effect of vaporization on the energy balance is likely due to the high boiling point of Pt.

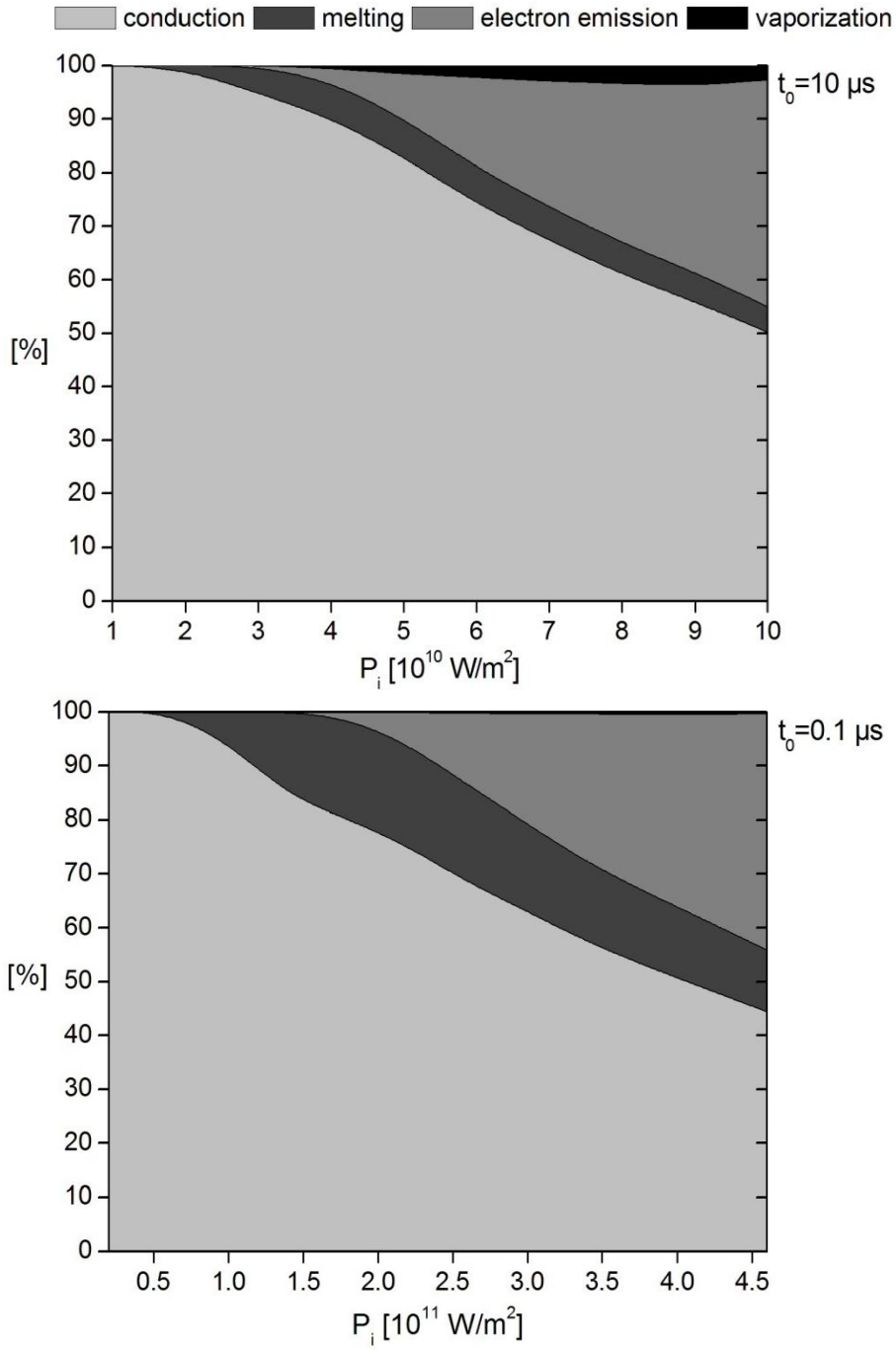

Figure 6.16 Distribution of the heat lost in conduction, melting, electron emission and vaporization as a function of the ion power density for times of interaction t_0=10 and 0.1 µs.

6.2.5 Results in Pt/Ni Multilayer

The experimental values of molten depth and molten volume presented in section 5.3 have been obtained from craters produced in multilayer systems made of a Pt/Ni multilayered surface on a Ag substrate. The simulation results presented in the previous section, however, have been obtained for a bulk Pt cathode. Both were compared in order to determine

characteristic information related to the crater formation. In this section, simulations are performed in a multilayered electrode in order to verify that the simulation results obtained in bulk Pt can be correctly compared to the experimental results.

6.2.5.1 Pt/Ni Multilayered Electrode Properties

The multilayered electrode is defined by two regions: the substrate with the properties of pure Ag and the multilayered surface. The properties of the surface, with respect to electron emission and vaporization, are assumed to be the same as those of the bulk Pt cathode because the surface of the Pt/Ni multilayer assembly consists of a pure Pt layer. The bulk properties of the multilayer such as the density, the specific heat capacity, the thermal conductivity and the latent heat of melting/mixing are determined. Because the density and the specific heat capacity are scalars, for a multilayer composite, $\rho^{Pt/Ni}$ and $c_p{}^{Pt/Ni}$ are given by the thickness-weighted average also called rule of mixture:

$$\rho^{Pt/Ni} = \frac{\rho^{Pt}\sum d^{Pt} + \rho^{Ni}\sum d^{Ni}}{\sum \mathrm{d^{Pt}} + \sum \mathrm{d^{Ni}}} \tag{6.20}$$

$$c_p^{Pt/Ni} = \frac{c_p^{Pt}\sum d^{Pt} + c_p^{Ni}\sum d^{Ni}}{\sum \mathrm{d^{Pt}} + \sum \mathrm{d^{Ni}}} \tag{6.21}$$

where Σd^{Pt} and Σd^{Ni} are the total thicknesses of the Pt and Ni layers equal to 800 and 700 nm, respectively.

For a multilayer, the conductivities parallel and normal to the layers are different. The conductivity parallel to the layers is given by summing the conductivities of each layer. As the effective thickness of the interfaces (~1 nm) is much smaller than the thickness of the layers (100 nm), their contribution can be neglected. Thus, the conductivity parallel to the layers $k_r{}^{Pt/Ni}$ can be described using the rule of mixture as follows [178]:

$$k_r^{Pt/Ni} = \frac{k^{Pt}\sum d^{Pt} + k^{Ni}\sum d^{Ni}}{\sum \mathrm{d^{Pt}} + \sum \mathrm{d^{Ni}}} \tag{6.22}$$

The conductivity normal to the layers $k_z{}^{Pt/Ni}$ is obtained by summing the thermal resistances of the layers and the interfaces as follows [178]:

$$\frac{\sum \mathrm{d^{Pt}} + \sum \mathrm{d^{Ni}}}{k_z^{Pt/Ni}} = \frac{\sum \mathrm{d^{Pt}}}{k^{Pt}} + \frac{\sum \mathrm{d^{Ni}}}{k^{Ni}} + n\rho_{int} \tag{6.23}$$

where n is the number of interfaces (n=15) and ρ_{int} is the thermal resistance of the interface. Interfacial thermal resistance values of metallic layers are all reported to range between 10^{-9} and 10^{-10} $m^2 \cdot K \cdot W^{-1}$ in the literature [178-180]. Thus, we take $\rho_{int}=5\times10^{-10}$ $m^2 \cdot K \cdot W^{-1}$ as a mean value. The density, specific heat capacity and conductivities of the multilayer are calculated as

a function of the temperature based on the temperature-dependent properties of each pure metal.

During mixing of two elements, a heat of mixing ΔH_{mix} is released corresponding to the enthalpy difference between the final mixed state and the initial unmixed state [181]. This heat of mixing can be calculated using the semi-empirical model of Miedema [182]. For an immiscible pair, ΔH_{mix} is positive (endothermic mixing), whereas for a miscible pair like Pt/Ni, ΔH_{mix} is negative (exothermic mixing). For Pt/Ni (50/50) we use the value ΔH_{mix}=-53.84 J/g reported in [183]. ΔH_{mix} is added to the positive latent heat of melting L_m in equation (6.10), thus reducing the heat consumed upon melting. As both metals have to be melted for mixing and because $T_m^{Pt}>T_m^{Ni}$, we assume T_m^{Pt} as the melting temperature for the multilayer.

6.2.5.2 Spot Temperature and Melting Depth

In Figure 6.17, the spot temperature and melting depth computed in the bulk Pt cathode and in the Pt/Ni multilayered cathode are displayed as functions of the ion power density for the pulse durations t_0=0.1 and 1 µs. For t_0=0.1 µs, the spot temperature in the multilayered cathode follows the spot temperature in the bulk cathode quite exactly. As a consequence, the parameters related to this temperature, such as the electron emission current and the vaporization rate, remain the same. However, the melting depth reached in the bulk cathode is slightly higher than that reached in the multilayered cathode. For t_0=1 µs, the spot temperature and the melting depth are much larger in the bulk cathode than in the multilayered cathode for a given ion power density. These large differences are due to the thermal properties, not of the multilayer assembly itself, but rather of the silver substrate. Since Pt and Ni have similar thermal conductivities of 71.6 and 90.7 W/m·K at 300 K, respectively, the conductivity of the multilayer does not differ strongly from that of pure platinum. The Ag substrate, however, presents a much higher thermal conductivity (429 W/m·K at 300 K). Therefore, the heat dissipated through conduction is more important, resulting in lower temperatures and shallower molten pools compared to the bulk Pt cathode. As shown in the results, the influence of the Ag substrate depends on the pulse duration. The thermal diffusion length $(2\alpha \cdot t_0)^{1/2}$ in Pt for t_0=1 µs is 7.1 µm whereas the multilayer thickness is 1.5 µm. Thus the substrate plays an important role in the heat conduction and the results differ strongly between bulk Pt and multilayered electrode. For t_0=0.1 µs, the thermal diffusion length is 2.2 µm, which corresponds approximately to the thickness of the multilayer assembly. Because the heat is mainly concentrated in the multilayer, the substrate has only a weak influence on the

thermal balance and the results in the bulk Pt cathode are comparable to those in the multilayered cathode.

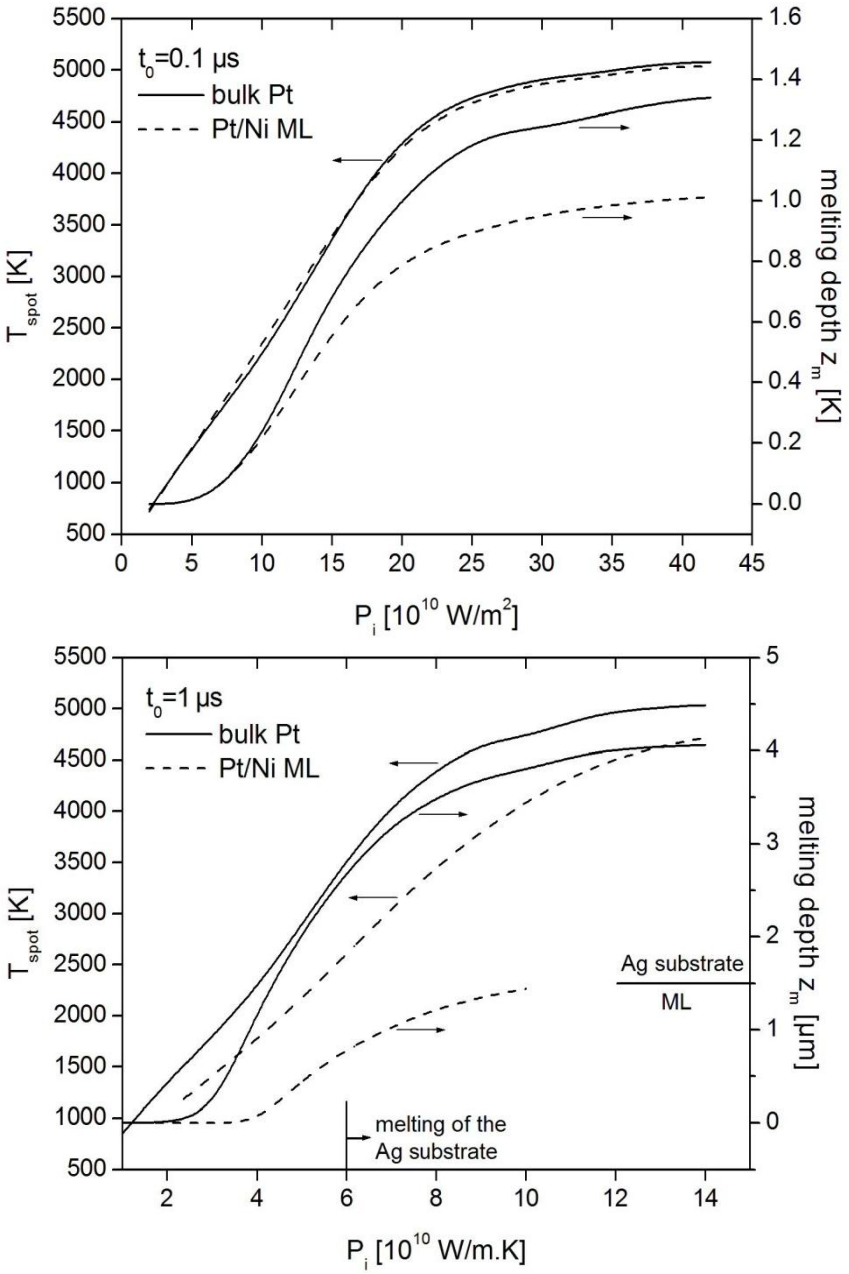

Figure 6.17 Comparison of the spot temperature and melting depth in bulk Pt cathode (full line) and in Pt/Ni multilayered cathode (broken line) for t_0=0.1 and 1 μs.

The simulation in the multilayered cathode provides useful information related to the time of formation of the crater. For t_0=1 μs, the Ag substrate, having a lower melting point than Pt and Ni, starts to melt at P_i=6×10^{10} W/m^2 whereas the molten depth in the multilayer is lower than 0.8 μm and the spot temperature is only 2600 K. The melting of the substrate is caused by the low temperature gradient below the surface due to the relatively long pulse

duration. For t_0=0.1 µs, the temperature gradient value is higher and no melting of the Ag substrate occurs. The influence of the pulse duration on the temperature gradient and the melting of the substrate is represented schematically in Figure 6.18. Grain refinement caused by the mechanical polishing of the Ag substrate prior to the multilayer deposition can still be observed below the craters (Figure 5.6). Upon melting and re-solidification, larger and elongated grains would be observed at the substrate surface [144]. This demonstrates that the Ag substrate does not melt during crater formation. Therefore, times of crater formation equal or in excess of 1 µs can be definitely excluded.

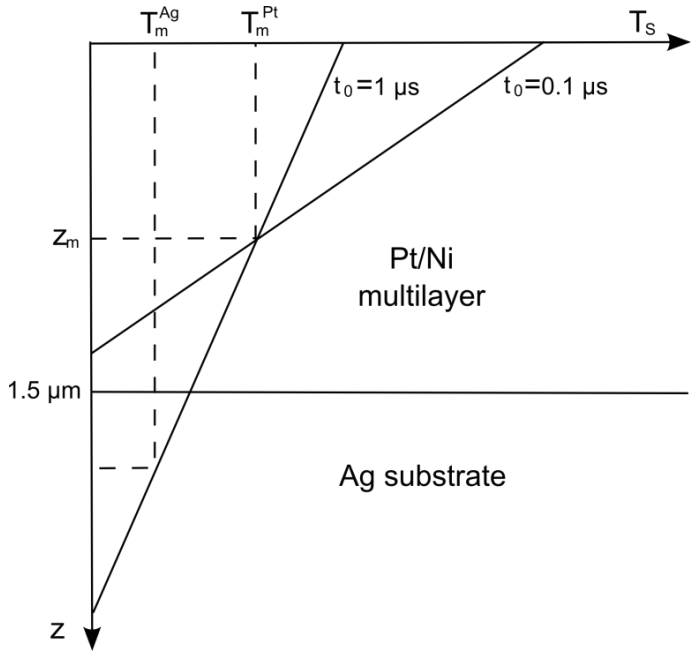

Figure 6.18 Schematic representation of the influence of t_0 on the temperature gradient below the surface (to simplify matters, temperature gradients are assumed to be constant). For t_0=0.1 µs and t_0=1 µs, the same melting depth z_m is reached in the multilayer. However, the smaller thermal gradient in the case of t_0=1 µs leads to melting of the Ag substrate.

6.3 Discussion

6.3.1 Comparison of the Results with Others Works

The FEM thermal simulation presented in the previous chapter permitted to estimate the time of formation of the craters and the surface power input density to be on the order of 0.1 µs and 4×10^{11} W/m^2, respectively. There are many papers dealing with these parameters for vacuum or atmospheric arcs. Here we make a comparison of our results with others works.

The spot lifetime constants reported in the literature can differ by several orders of magnitude. However, the differences are more due to the definition rather than the phenomena itself. Optical observation of spots on Mo and Cu showed luminosity fluctuations with intervals of 20-100 ns [184]. Another work based on the occurrence of discernable spot changes as a function of the time interval yielded a most probable value of 10-20 ns [72]. The method of division of the discharge duration by the number of craters left by the arc on W at room temperature resulted in an estimation of the spot lifetimes <70 ns [78]. Evaluation of the chaotic spot motion deduced for Cu arcs of 10-100 A lead to values of 5 to 40 ns [77]. Reduction of the discharge duration until only one crater is formed yielded to values of 3-5 ns for Cu and Mo [136]. Jüttner [185] reported that formation and rearrangement of spot fragments (<10 µm) take place in less than 20 ns. Finally, measured droplet velocities of several 100 m/s indicate that the liquid surface metal must be rapidly displaced [97, 98]. The liquid will cover a distance of 10 µm corresponding to a usual crater in less than 100 ns. In spite of the large scatter of the values reported in the literature and the different methods used to determine them, it can be deduced that the most probable spot residence time during which the crater is formed must lie between 10 and 100 ns. This value is well in accordance with the value that we proposed.

As in the case of spot lifetime, there are great differences in the values of the power surface density at the cathode reported in the literature. Rossignol *et al.* [86] proposed for a Cu cathode a surface power density on the order of 10^{12} W/m^2. Salihou *et al.* [186] experimentally determined the power surface density for low current arcs (<5 A) in Ag and Cu cathodes to be 3×10^{11} to 5×10^{11} W/m^2. Abbaoui *et al.* [173] studied the behavior of Cu, Ag and Ni cathodes subjected during 100 ns to power densities ranging between 1×10^{11} and 5×10^{12} W/m^2. Messaad *et al.* [175] estimated the ion power density heating a Cu cathode to lie between 2×10^{11} and 5×10^{11} W/m^2 for currents raging from 5 to 50 A. Coulombe and Meunier [60] deduced in the case of Cu values of heat input to the cathode spot surface in the range of 1×10^{10} to 6×10^{10} W/m^2. In a recent study, Testé *et al.* [187] estimated the surface power density for a Cu cathode to be 6×10^{9} to 7×10^{9} W/m^2. The difference of two or three orders of magnitude between these results may be explained by the different time and space scales used for the description of the arc-electrode interaction [188]. Indeed, in the case of an electric arc of several 100 A, there are a great number of successive spots. If one considers the heating caused by a single spot or fragment with a characteristic time <100 ns, the power density is very high (10^{11}-10^{12} W/m^2). However, the heating of a set of spots could be equivalent to a unique macroscopic heat source (diameter larger than 100 µm) lasting for

several 10 µs. In this case, the power surface density is much lower (10^9-10^{10} W/m^2). In our simulation, we consider the formation of a single crater and the value that we proposed of 4×10^{11} W/m^2 is well in the range of the values reported for single spot or fragment.

6.3.2 Comparison with Arc Craters in Electrical Contacts

The craters discussed in this thesis are exclusively caused by ignition discharges between two static electrodes. Similar craters can also be obtained when separating two contacts in an electrical circuit. Figure 6.19 shows a crater produced by a single break operation in an automotive relay with an arc current of 16 A and pure Pt as cathode material [189]. Contrary to ignition discharges, the voltage and current vs. time curves of such break operation discharges permit to clearly determine the arc lifetime, that is, the time during which craters are formed. In the case of pure Pt cathodes, the arc lifetime was ~20 µs. The craters are greater than those caused by ignition discharges with total diameters between 80 and 100 µm. Severe molten material ejection is also observed (Figure 6.19a). Similar to ignition discharge craters, electrical contact arc craters are actually composed of several overlapped depressions (Figure 6.19b). This indicates that the arc cathode root has a high mobility and that each single spot is probably formed within a time shorter than 1 µs. Although the discharges are not completely comparable, the large surface degradation caused by a 16 A arc within a time of ~20 µs suggests that the smaller ignition discharge craters discussed in this work must be produced within much shorter times. This comparison with arc craters in electrical contacts further supports the estimation of a crater formation time lower than 1 µs.

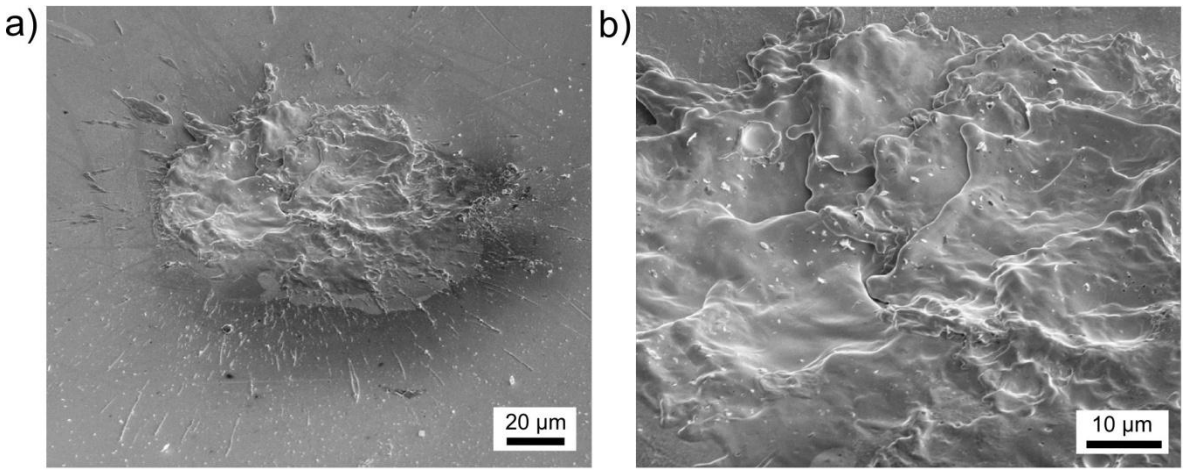

Figure 6.19 a) Large crater produced on a Pt cathode by a single break operation in a relay (16 A, 20 µs). b) Magnification of the crater center showing the superposition of numerous spots.

6.3.3 Current-Time Characteristic of the Ignition Discharge

While the voltage is mainly determined by the physical processes taking place at the cathode surface and in the plasma, the current is given by the components of the ignition system. The current-time characteristic can be described using an exponential decay function:

$$i(t) = i_0 \cdot e^{-\frac{t}{\tau}} \tag{6.24}$$

where i_0 is the initial current and τ is the time constant of the discharge. For a capacitor $\tau = R \cdot C$ and for a coil $\tau = L/R$. Figure 6.20 shows the current-time characteristic calculated for discharges produced at pressures of 10 and 1 bar with the corresponding breakdown voltages U_b=25 kV and U_b=5 kV. Each curve is obtained by adding the current-time characteristics of breakdown, capacitive and inductive discharges. Like in our experiments, the spark plug has no internal resistor (R_P=0) and the spark resistance also known as Toepler's resistance [13] is estimated to be ~100 Ω [1]. According to our measurements, the resistance of the high voltage cable and the plug connector is R_{PC}=1.5 kΩ (see equivalent circuit in Figure 3.2). The spark plug and coil capacities are C_P=12 pF and C_C=50 pF, respectively. The coil provides an initial current of 100 mA, whereas its inductance and resistance are L_2=20 H and R_2=10 kΩ, respectively.

The first phase of the ignition discharge, the breakdown, is very short (<10 ns). During this phase, the energy stored in the spark plug capacitance is discharged. The peak of current is determined by the ignition voltage U_b and the resistance of the spark. At p=1 bar, this peak is about 50 A, while at p=10 bar it rises to a value of 250 A. This phase is followed by a short capacitive discharge lasting for roughly 1 µs. During this time, the coil capacity discharges its energy through the resistance of the high voltage cable and the plug connector (also called radio interference damping resistor). At high pressure, the initial current for this phase is ~15 A and currents in excess of 1 A last for over 0.2 µs. At low pressure, the initial current is only ~3 A and it drops below 1 A within less than 0.1 µs. Finally, the coil discharges its energy and the current decreases from its initial value of ~100 mA to zero within a couple of milliseconds. Because of the low current values, the inductive discharge will mostly take the form of a glow discharge.

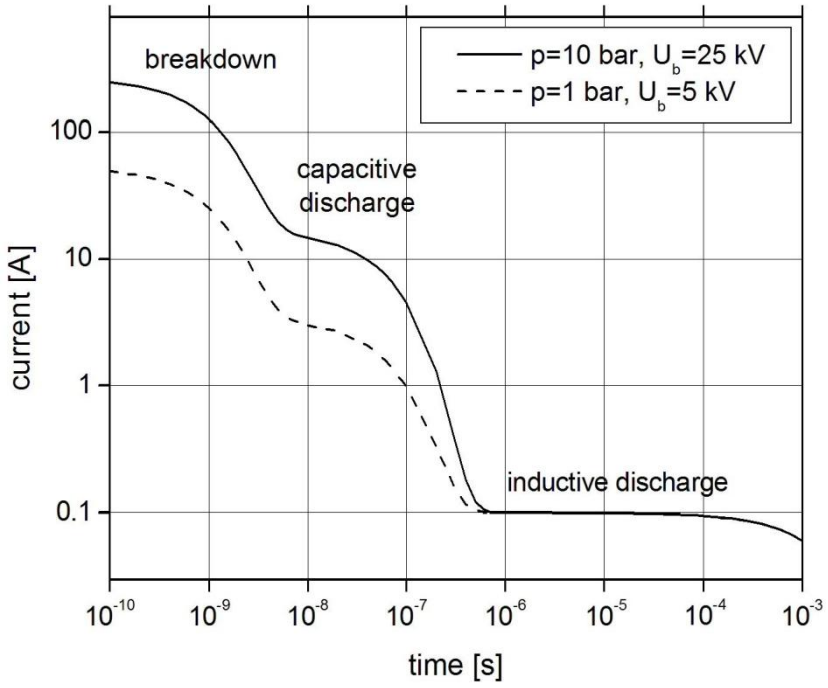

Figure 6.20 Comparison of the current-time characteristic between ignition discharges produced at p=10 bar (U_b=25 kV) and at p=1 bar (U_b=5 kV).

6.3.4 Correlation between the Discharge Characteristic and the Crater Formation

The results of the thermal simulation presented in section 6.2.4 indicate that single ignition craters are formed within a time of 0.1 µs associated with currents in the range from 5 to 25 A. According to the current-time characteristic presented in Figure 6.20, these time and current values correspond well with the capacitive arc discharge that immediately follows the breakdown. Therefore we believe that this phase, also referred to as instationary arc discharge, is responsible for the formation of the craters produced at high pressure on the surface of Pt (and also Pt/Ni multilayered) cathodes. At high pressures and assuming that the arc-to-glow transition occurs for currents between 1 and 0.1 A, the arc can last up to several 100 ns. This duration results in the formation of several successive spots that are visible as overlapping craters. As the current decreases with time, the radius of the spots decreases in order to maintain the required current density to sustain the arc and the smaller craters overlap the larger ones. This phenomenon is observed on bulk Pt as well as Pt/Ni multilayered cathodes (Figure 6.21).

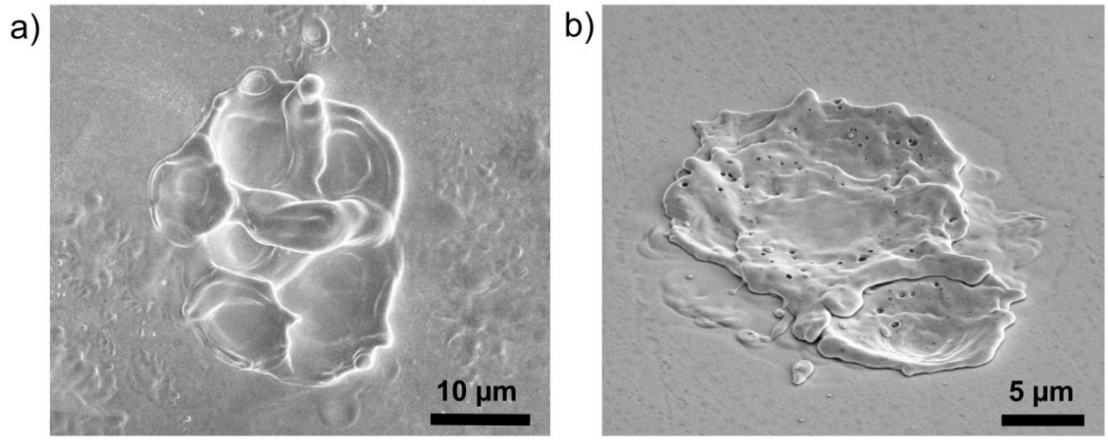

Figure 6.21 SEM images of craters produced at p=10 bar on a) bulk Pt and b) Pt/Ni multilayered cathode. Several craters are overlapped, indicating the existence of successive cathode spots.

When the discharges are produced at a low pressure (p=1 bar), the capacitive discharge begins with lower currents of ~3 A, which is, according to the results of our simulation, not sufficient to produce craters with a radius of 5-10 µm. In these conditions, only small depressions (~1-2 µm) can sometimes be observed as reported by Soldera *et al*. [96] in pure Pt and shown in Figure 5.8a in the case of the Pt/Ni multilayered cathode. Furthermore, low pressures promote the transition to the glow discharge by permitting the plasma to more easily extend compared to discharges produced at high pressures (section 4.2.3). Both the low initial capacitive current (≤3 A) and the higher arc-to-glow transition current make the existence of an arc more difficult. Therefore, it is expected that the breakdown will be immediately followed by the glow discharge at low pressure. The breakdown generates only a smooth melting of the surface resulting in the flat craters, also called "low pressure craters" in Chapter 5. At high pressure, the flat crater caused by the breakdown exists, but it is covered by the depressions produced by the following arc as can be seen in Figure 6.21b.

6.3.5 Effects of the Inductive Arc Discharge

The inductive discharge of the ignition coil is associated with currents lower than 100 mA. According to the voltage-current characteristic of discharges, the arc-to-glow transition occurs at currents ~1 A [8, 13, 17]. Therefore, the inductive discharge of the coil should theoretically always adopt a pure glow form. However, the discharge mode analysis presented in Chapter 4 has shown that, in the case of Pt, the arc fraction can reach ~5 % in air at high pressure, which corresponds to a mean arc time of several tens of microseconds. This

indicates that the inductive discharge, in spite of low current values <100 mA, can briefly take the form of an arc before changing into a glow, thus leaving marks on the surface.

The curves in Figure 6.22 show the evolution of the cathode spot radius *a* with time during the capacitive and inductive phases of the discharge. This radius is calculated as follows:

$$a = \sqrt{\frac{(1-s)\cdot i(t)\cdot U_i}{P_i \cdot \pi}} \tag{6.25}$$

where *s* is the electronic current fraction, *i*(*t*) is the discharge current, U_i is the mean heat delivered by each ion impinging on the cathode surface and is taken to be 28 V (Figure 6.10), and P_i is the ion power density required to reach a given electronic current fraction. For example, for *s*=0.5, the spot temperature must reach 4500 K and P_i must then be equal to 2×10^{11} W/m^2 (Table 6.1). As the electronic fraction increases, the total power delivered by ions to the cathode decreases (numerator of the square root term). In addition, higher spot temperatures must be reached (Figure 6.13) and the required ion power density P_i increases (Figure 6.11), resulting in the contraction of the spot. The curves in Figure 6.22 show that the capacitive (or instationary) arc discharge is able to produce craters having a radius of 8-11 µm, and that this radius decreases to 1-2 µm within the first microsecond. As discussed in section 6.2.4.3, the existence of an arc requires *s*≥0.5. For *s*=0.5, the inductive discharge can cause the formation of craters with a radius lower than 2 µm. If one assumes that 80 % of the current is carried by electrons, which is a more realistic value for an arc [8], the inductive arc crater radius becomes lower than 1 µm. Therefore, the arc phase taking place at the beginning of the inductive discharge cannot produce the large craters (5-10 µm) discussed in this chapter. However, it is likely that the inductive arc generates the numerous sub-µm craters observed on the cathode surface in the vicinity of the main large crater. These sub-µm craters are typically aligned along residual scratches produced during the polishing procedure (Figure 6.23). Soldera *et al*. [96] proposed that the severe plastic deformation in these scratches can decrease the work function of the material, promoting electron emission [190]. The topography of the scratches may also enhance the electric field strength at the surface, locally concentrating the lines of current.

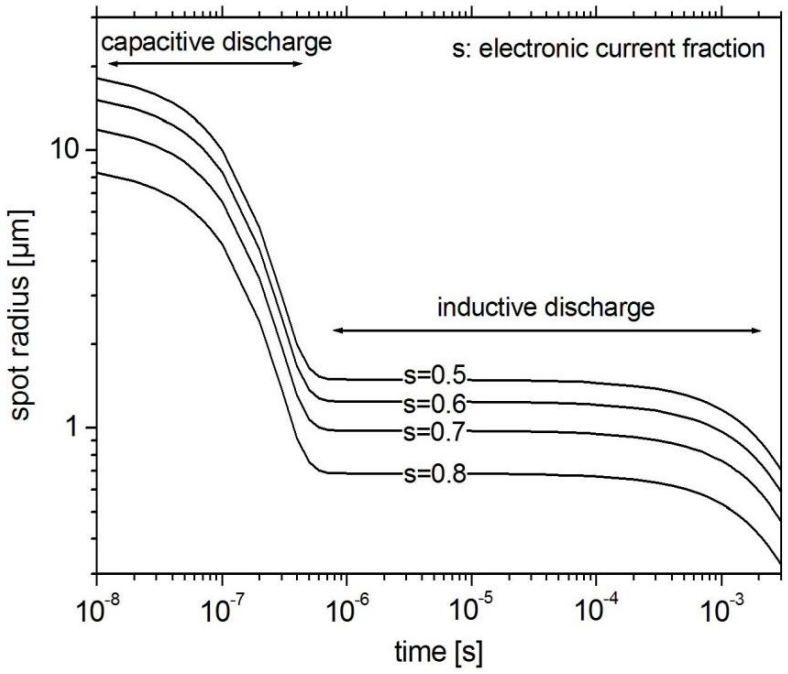

Figure 6.22 Evolution of the cathode spot radius with time during the capacitive and the inductive arc phases of the discharge for electronic current fractions between 0.5 and 0.8.

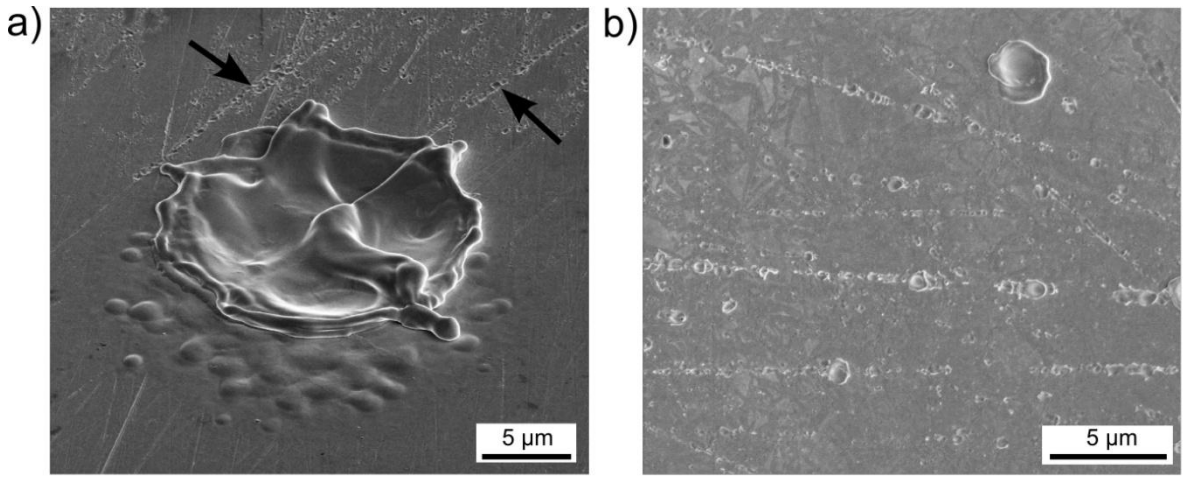

Figure 6.23 Sub-µm craters produced by the arc phase of the inductive discharge along residual polishing scratches.

6.3.6 Correlation with Cathode Wear

Figure 6.24 shows the experimental values of the wear of platinum cathodes as a function of the breakdown voltage determined in endurance tests at a constant pressure of 7 bar and reported by Rager [24]. The wear is found to be linear with the breakdown voltage U_b and is composed of an inductive part (independent of U_b) and a capacitive part (dependent on U_b). According to the model proposed by Rager, the erosion mechanism of platinum

cathodes relies on the local oxidation of Pt on the cathode spot surface (section 2.4.5). As a consequence, the erosion is directly related to the formation of craters on the surface. Although the capacitive or instationary arc discharge lasts for short times (~µs) compared to the inductive arc discharge (10-100 µs), its large contribution to cathode wear confirms that the large craters are formed during the capacitive arc discharge and not during the inductive discharge. The breakdown-voltage-independent erosion caused by the inductive discharge may result either from the formation of sub-µm craters, as discussed above, or from the sputtering of Pt atoms during the glow discharge (section 2.4.3).

On the right axis, the charge of the capacitive discharge Q is shown as a function of the breakdown voltage. It is given by:

$$Q = \int i(t) \cdot dt = U_b \cdot C_C \tag{6.26}$$

Like the wear, the charge of the capacitive discharge is linear with the breakdown voltage. Thus, the mean erosion rate of the capacitive discharge can be determined and is found to be E_c=92 µg·C^{-1}. This value is well in accordance with the experimental and theoretical arc erosion rates reported for various metals in the literature and which vary typically from 10 to 300 µg·C^{-1} ([80] and references therein). The arc erosion of materials such as Cu and Ag involves vaporization and ejection of liquid [102]. In the case of Pt, however, the erosion relies on the plasma-assisted oxidation on the spot surface, which implies that oxygen molecules, radicals or ions are present in the cathode surface region. The cathode spot model for non-refractory cathodes states that the internal structure of the spot is not disturbed by the surrounding ambient gas if the local metallic vapor pressure is higher than the external pressure [62]. The local metallic vapor pressure is related to the surface temperature via the equilibrium vapor pressure $p_v(T_s)$. At the required minimum spot temperature T_{spot}=4500 K, the metallic vapor pressure is ~3 bar whereas at T_{spot}=5000 K, it is ~12 bar. Therefore, in the case of ignition discharges produced at high pressures in air (6-10 bar), the metallic vapor pressure is more or less equal to the operating external pressure and oxygen of the ambient gas may be present in the cathode spot plasma. Although oxygen has a higher first ionization energy than Pt (E_i^O=13.62 eV, E_i^{Pt}=9.0 eV [191]), oxygen ions O^+ can form and react with the cathode spot surface, resulting in the formation of volatile PtO_2 and finally in the loss of material. The modeling of the oxidation induced erosion requires knowing the fraction of O^+ reaching the surface. For this purpose, phenomena taking place in the cathode sheath and in the ionization zone should be considered, which is beyond the scope of the present simulation.

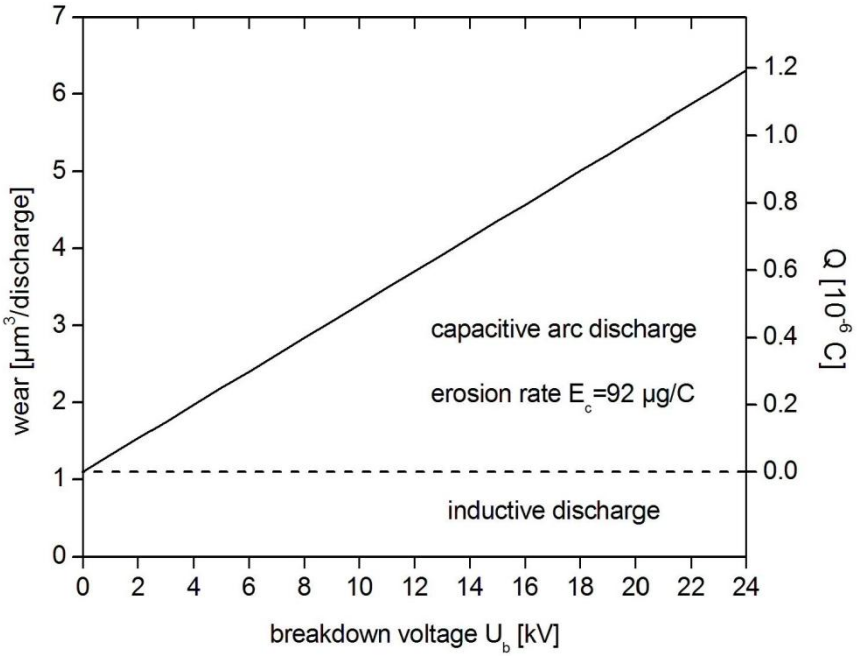

Figure 6.24 Wear of Pt cathodes (left axis) determined in endurance tests [24] and charge of the capacitive discharge *Q* (right axis) as a function of the breakdown voltage. The arc erosion rate is found to be 92 µg·C^{-1}.

6.4 Summary

The local thermal effect of the ignition discharge on the electrode surface is first analyzed using analytical models. The use of analytical models implies assuming that the material properties are constant and that no phase transitions occur (no boiling, no melting). The semi-continuous point and disk source models are employed to determine the temperature distribution in the electrode. The point source model is found to be unsuitable for our problem since it predicts a hemispherical molten pool, where molten depth and molten radius are equal. The disk source is believed to be more appropriate to represent the heat input of the spark/arc and it predicts a more realistic molten pool shape. This model is used to determine the power density required to reach the melting point of the surface as a function of the heat pulse duration. The analysis is performed with a disk radius of 10 µm (~crater radius) for different metals. The results show that the time of interaction between the heat source and the electrode has a large influence on the melting behavior of the surface and that shorter heat pulses result in higher melting power densities. Moreover, the results point out that the melting susceptibility of the electrode is mainly determined by its melting temperature for pulses shorter than 1 µs, and by its thermal conductivity for pulses longer than 10 µs.

For a better analysis of the temperature distribution and power density at Pt cathode craters, a FEM simulation is developed. The simulation is based on cathode spot models of vacuum and atmospheric arcs reported in the literature. It includes the most relevant phenomena such as ion bombardment (heating mechanism), heat conduction into the bulk, melting, vaporization, and electron emission (cooling mechanisms). In comparison with numerical models of other works, special attention is paid to the correct description of the cathode bulk with, for example, temperature dependent material properties. The surface of the cathode is subjected to different ion power densities ranging between 10^{10} and 10^{12} W/m^2 for durations equal to 0.1, 1 and 10 µs over a disk of 10 µm radius. By comparing the results of the simulation with experimental molten depth/volume values presented in Chapter 5, and by considering the theoretical criterion $J_e \geq J_i$ at the cathode spot surface, the following characteristic values of the crater formation process can be determined:

- spot temperature $T_{spot} \geq 4500$ K
- time of formation $t_0 \sim 0.1$ µs
- ion power density $P_i \sim 4 \times 10^{11}$ W/m^2
- current ~5-25 A (radius 5-10 µm)
- vaporized volume ~1 µm^3

For a better comparison with experimental results, simulations are also performed in a multilayered electrode. For a pulse duration of 0.1 µs, the results (temperature, melting depth) are comparable with those obtained in bulk Pt. For this short time, the thermal diffusion length is roughly equal to the multilayer thickness, and the highly conductive Ag substrate does not strongly influence the temperature distribution in the crater region compared to the bulk case. For a pulse duration of 1 µs, the thermal diffusion length is higher (~7 µm) and the results are strongly modified by the conductivity of the Ag substrate. Moreover, the smaller temperature gradient in the case of a pulse of 1 µs leads to the melting of the Ag substrate for relatively low surface temperatures. As the melting of the substrate is not observed experimentally, it confirms that the time of formation of the crater must be lower than 1 µs.

The time and power input density values determined with the help of the simulation are found to be in good agreement with values reported in other works dealing with the modeling of cathode spots. A comparison with larger Pt craters produced in another way in relays also suggests that each single crater must be formed within less than 1 µs. The results are compared with the current-time characteristic of an ignition discharge, permitting to identify the short capacitive arc discharge following the breakdown as the most probable phase

responsible for the production of the large craters (5-10 µm) observed in Pt. The sub-µm craters are caused by the arc sometimes taking place at the beginning of the inductive discharge. The hypothesis that the craters are caused by the capacitive arc discharge is supported by the correlation between cathode wear and breakdown voltage reported in a previous work. The corresponding calculated erosion rate of 92 $\mu g \cdot C^{-1}$ lies well in the range of the cathode erosion rate values reported in the literature.

CHAPTER 7

Conclusions and Outlook

The development of new high performance materials for electrode and electrical contact devices requires a better understanding of the complex degradation mechanisms caused by the electrical discharge plasma on the surface of materials. This can be in particular achieved through the precise characterization of the material microstructure and its local modification. In the present study, the interaction of high voltage ignition discharges with the surface of electrodes was experimentally and theoretically investigated. The most important features drawn from this work are summarized in this section. A more detailed summary of the results can be found at the end of Chapters 4, 5 and 6.

The ignition discharge, contrary to many other discharge types in technical applications, is composed of two distinct phases: the arc and glow modes. Each mode is associated with different plasma parameters and electron emission mechanisms from the cathode, and resulting in different effects on the surface. Chapter 4 aimed to present a quantitative analysis of the ignition discharge modes for different cathode materials, pressures, and atmospheres. Such analysis is important, since it permits to correlate the discharge mode behavior with the modifications observed on the surface, or the macroscopic wear of the electrode measured via other techniques.

- A method based on oscilloscopic measurements was developed in order to determine the arc and glow phase fractions of ignition discharges. Numerous discharges can be integrated and automatically analyzed, irrespective of the irregularities of the curves, thus providing highly reliable statistical values. This method is presently used in other works to investigate the evolution of the discharge mode with time in endurance tests.
- The arc fraction of ignition discharges was measured for pressures ranging between 1 and 10 bar, in air and nitrogen, and for Ag, Cu, Ni and Pt electrodes. The arc fraction increases as the pressure increases, irrespective of the cathode material or gas used. This is mainly due to the fact that the glow discharge is not stable at high pressure, which leads to transitions back to the arc mode.

- The arc fraction at high pressure is found to be higher in nitrogen than in air for all metals except Ag. This effect is likely due to higher cathode fall voltage of the glow discharge in air than in nitrogen, which increases the secondary electron emission coefficient and promotes the glow phase.
- Ag sparked in air presents a singular behavior because it forms a thick Ag_2O layer. The oxidation of the surface is caused by the highly reactive plasma of the glow discharge. The oxide layer is locally stripped off by the arc cathode root and ejected as molten particles. This mechanism has a stabilizing effect on the arc mode.
- The arc fraction at high pressure tends to be higher for low melting point cathodes (Ag, Cu) than for high melting point cathodes (Ni, Pt). The lower the melting (or boiling) point of the cathode, the more easily TF electron emission can be achieved, which promotes the arc phase.

The ignition discharge causes the formation of erosion craters on the cathode surface. Chapter 5 focused on the characterization of the local microstructural modifications in the crater region such as melting, material displacement and re-solidification.

- FIB/SEM dual beam techniques reveal to be ideally suited for the investigation of small features such as craters caused by electrical discharges. For the first time, FIB-nanotomography and cross section EBSD of such craters have been carried out, allowing a quantitative characterization of their microstructure. The novel techniques presented in this work permit to assess the microstructural nature of the material degradation not only of electro-erosion craters, but also of surface morphologies created in others ways.
- The investigation of craters produced in bulk metallic electrodes (Ag, Pt) does not permit to distinguish the molten region. This problem was successfully solved by producing craters on multilayered electrodes, where the molten region remains irreversibly modified after re-solidification. Craters produced in bulk and in multilayered electrodes were found to be similar in morphology and size.
- The immiscible Ag/Ni multilayer system permits to observe clearly the displacement of molten material but it is not appropriate for monitoring the extent of the molten pool. The miscible Ni/Cu and Pt/Ni multilayer systems permit to monitor the molten pool via the formation of a solid solution region. This last system was used to investigate the microstructure of craters produced at different pressures

- At low pressure (<4 bar), the discharge produces only a smooth melting of the surface with molten volumes in the range of 50 μm^3. The formation of these craters is attributed to the breakdown phase of the ignition discharge.
- At high pressure (>6 bar), the discharge produces a crater consisting of one or several depressions surrounded by a rim of molten material. The molten pool volume was determined by means of FIB cross sections and FIB-nanotomography to be around 200-250 μm^3. These arc craters are likely caused by the capacitive part of the discharge.
- EBSD analysis revealed that the cooling and re-solidification of the molten pool occurs under high temperature gradients (>10^9 K/m) directed normal to the surface.
- Between 20 and 40 % of the molten material is displaced from the crater center to the rim under the ion pressure acting on the surface.

Crater formation on the electrode surface results from the intense and local heating mainly caused by ion bombardment. In Chapter 6, the thermal behavior of a cathode subjected to heat fluxes of different durations was analyzed using analytical methods and FEM simulations.

- Local heating due to a spark or an arc can be treated as a heat conduction problem in a semi-infinite electrode submitted to a heat flux over a point, disk or Gaussian source. The semi-continuous disk source model is found to be the most realistic regarding the shape of the molten pool that it predicts.
- The critical melting power density is determined using this last model for different materials. The melting power density increases as the pulse becomes shorter and its values range between 10^{10} and 10^{12} W/m^2. The melting susceptibility of the material is mainly determined by its melting temperature for pulses shorter than 1 µs and by its thermal conductivity for pulses longer than 10 µs.
- A FEM simulation of the temperature distribution and power density at platinum cathode craters is developed based on the modeling of cathode spots in vacuum and high pressure arcs. The simulation includes phenomena such as ion bombardment, heat conduction into the bulk, melting, vaporization, and electron emission.
- By comparing the simulation results with experimental data, characteristic values of the crater formation process are determined. Among other parameters, the time of formation and the heating ion power density are estimated to be on the order of 0.1 µs and 4×10^{11} W/m^2, respectively.

- Heat conduction, electron emission, and melting are the more important cooling mechanisms while vaporization has a negligible effect.
- Simulations performed in multilayered electrodes similar to those used experimentally confirm that the time of formation of the craters must be shorter than 1 µs.
- The time and power density determined in this work are found to be well in accordance with data reported in the literature for arc cathode spots.
- Comparison with the current-time characteristic of the discharge suggests that the craters are created by the capacitive arc discharge following the breakdown. The inductive arc discharge is believed to produce sub-µm craters.
- The decisive role of the capacitive discharge in crater formation is supported by the breakdown-voltage-dependent wear of Pt electrodes reported in a previous study.

Outlook

This work aimed to provide a better understanding of plasma-cathode interaction and electrode surface modifications in the particular case of ignition discharges in spark plugs. In contrast to most studies in the field of material degradation caused by electrical discharges, this work tried to combine experimental data based on microstructural characterization of the electrode material with theoretical results obtained via the use of physical models and thermal simulations. It provides new insights into certain aspects of the interaction between ignition discharges and electrodes and, in particular, into the formation of erosion craters. However, further efforts are needed to relate material properties and characteristics of the electrical discharge to the effective wear of the electrode. In the following list, some experimental and theoretical developments are suggested for future studies:

- The size and lifetime of the spots formed on the electrode surface are important parameters for the development of new models. Direct observation of these spots with a high speed camera having both high temporal and high spatial resolutions should permit to better determine (or confirm) these features. However, a major difficulty here lies in the strong radiation of the plasma column which leads to an overestimation of the spot size even in vacuum arcs [73].
- Spectroscopic investigations of the discharge plasma hold the promise of assessing important parameters such as electron density or plasma temperatures, which can be very useful for further simulations. In particular, the time-resolved evolution of the cathode atom density in the plasma should permit to better identify which phase of the discharge

causes the most net erosion. However, this technique cannot be applied in all atmospheres due to the possible superposition of the intensity lines of electrode and gas atoms.

- The results of this work pointed out that the capacitive discharge (~µs) following the breakdown is relevant for crater formation and, as a consequence, for the electrode erosion. The oscilloscope set-up used in this work is well adapted for measuring the arc and glow phases of the inductive discharge. However, the low bandwidth of the voltage and current probes does not permit a reliable measurement of the capacitive part of the discharge. This could be improved by using, for example, a Pearson current monitor or an ammeter shunt for measuring the capacitive current. The galvanic isolation of the oscilloscope using an isolation transformer as well as potential measuring points closer to the electrode gap would also improve the reliability of the discharge voltage diagnostic.
- The simulation presented in this work considers a constant flux of ions toward the cathode surface. For a more realistic simulation of arc-cathode interaction, the ion flux should be related to the electron and atom emission from the surface. This would imply considering three regions: the cathode and its surface like in the present simulation, the cathode sheath (collisionless), and the pre-sheath (or ionization zone). Such models are usually treated with a stationary approach. However, the assumption that it is a stationary phenomenon on a smooth surface is contrary to the experimental facts (superposition of craters). Therefore, future simulations in this field should also attempt to take into account time dependent phenomena like formation/destruction of protrusions and explosive evaporation.

References

[1] R. Maly, *Spark Ignition: Its Physics and Effect on the Internal Combustion Engine*, in *Fuel Economy: Road vehicles powered by Spark Ignition Engines*, (Eds: J. C. Hilliard, G. S. Springer), Plenum Press, New York (1984).

[2] R. Maly, W. H. Bloss, W. Herden, B. Saggau and E. Wagner, *Entladungsvorgänge in Zündkerzen - Das Funkenplasma und seine Auswirkungen auf die Entflammung*, in *4. Statusseminar Kraftfahrzeuge und Straßenverkehr, Bundesministerium für Forschung und Technologie, Berlin, Sept. 1976*, (Ed: Bundesministerium für Foschung und Technologie), Verlag TÜV Rheinland, Köln (1977).

[3] R. Maly, W. Herden, B. Saggau, E. Wagner, M. Vogel, G. Bauer and W. H. Bloss, *Die drei Phasen einer elektrischen Zündung und ihre Auswirkungen auf die Entflammungseinleitung*, in *5. Statusseminar Kraftfahrzeuge und Straßenverkehr, Bundesministerium für Forschung und Technologie, Bad Alexanderbach, Sept. 1977*, (Ed: Bundesministerium für Forschung und Technologie), Verlag TÜV Rheinland, Köln (1978).

[4] W. Herden, R. Maly, B. Saggau and E. Wagner, *Neue Erkenntnisse über elektrische Zündfunken und ihre Eignung zur Entflammung brennbarer Gemische, 2. Teil*, Automobil-Industrie, **2/78** (1978) 15.

[5] H. Albrecht, W. H. Bloss, W. Herden, R. Maly, B. Saggau and E. Wagner, *New Aspects on Spark Ignition*, SAE Paper, **770853** (1977).

[6] H. Albrecht, R. Maly, B. Saggau and E. Wagner, *Neue Erkenntnisse über elektrische Zündfunken und ihre Eignung zur Entflammung brennbarer Gemische*, Automobil-Industrie, **4/77** (1977) 45.

[7] H. Bauer, *Ottomotor-Managment/Bosch*, 1. Auflage, Robert Bosch GmbH, Wieveg, Wiesbaden (1998).

[8] Y. P. Raizer, *Gas Discharge Physics*, Springer Verlag, Berlin (1997).

[9] L. N. Dobretsov and M. V. Gomoyunova, *Emission Electronics*, Nauka, Moscow (1966).

[10] J. S. Townsend, *Electricity in Gases*, Oxford University Press (1915).

[11] J. S. Townsend, *Electrons in Gases*, Hutchinson (1948).

[12] J. M. Meek and J. D. Craggs, *Electrical Breakdown of Gases*, Clarendon Press, Oxford (1953).

[13] A. Küchler, *Hochspannungstechnik: Grundlagen - Technologie - Anwendungen*, VDI-Verlag, Düsseldorf (1996).

[14] F. Paschen, *Über die zum Funkenübergang in Luft, Wasser und Kohlensäure bei verschiedenen Drücken erforderliche Potentialdifferenz*, Annalen der Physik, **37** (1889) 69.

[15] L. B. Loeb, *Basic Processes of Gaseous Electronics*, University of California Press, Berkeley (1960).

[16] H. Raether, *Electron Avalanches and Breakdown in Gases*, Butterworths, London (1964).

[17] P. G. Slade, *The Arc and Interruption*, in *Electrical Contacts: Principles and Applications*, (Ed: P.G. Slade), Marcel Dekker, New York (1999).

[18] M. M. Kekez, M. R. Barrault and J. D. Craggs, *Spectroscopic investigation of the spark channel*, J. Phys. D: Appl. Phys., **5** (1972) 253.

[19] I. D. Chalmers, *The transient glow discharge in nitrogen and dry air*, J. Phys. D: Appl. Phys., **4** (1971) 1147.

[20] T. Fujiwara, T. Sato, J. Sekikawa and H. Yamada, *Transient glow discharge in nitrogen after the breakdown*, J. Phys. D: Appl. Phys., **27** (1993) 826.

[21] I. D. Chalmers and H. Duffy, *Observations of the arc-forming stages of spark breakdown using an image intensifier and converter*, J. Phys. D: Appl. Phys., **4** (1971) 1302.

[22] E. Marode, *The mechanism of spark breakdown in air at atmospheric pressure between a positive point and a plane. I. Experimental: Nature of the streamer track*, J. Appl. Phys., **46** (1975) 2005.

[23] S. Achat, Y. Teisseyre and E. Marode, *The scaling of the streamer-to-arc transition in a positive point-to-plane gap with pressure*, J. Phys. D: Appl. Phys., **25** (1992) 661.

[24] J. Rager, *Funkenerosion an Zündkerzenelektroden*, PhD Thesis, Saarland University, Saarbrücken, Germany (2006)

[25] J. V. R. Heberlein, C. W. Kimblin and A. Lee, *Nature of the Electric Arc*, in *Circuit Interruption, Theory and Technique*, (Ed: T.E. Browne), Marcel Dekker, New York (1984).

[26] A. v. Engel, *Ionized Gases*, Clarendon Press, Oxford (1965).

[27] E. E. Kunhardt, *Generation of Large-Volume, Atmospheric-Pressure, Nonequilibrium Plasmas*, IEEE Transactions on Plasma Science, **28** (2000) 189.

[28] F. Llewellyn-Jones, *The Glow Discharge and an introduction to Plasma Physics*, Methuen, London (1966).

[29] E. E. Kunhardt and L. Luessen, *Electrical Breakdown and Discharges in Gases*, Plenum, New York (1981).

[30] C. E. R. Bruce, *Transition from glow-to-arc discharge*, Nature, **161** (1948) 521.

[31] H. Y. Fan, *The Transition from Glow Discharge to Arc*, Physical Review, **55** (1939) 769.

[32] W. S. Boyle and F. E. Haworth, *Glow-to-Arc Transition*, Physical Review, **101** (1956) 935.

[33] B. Rethfeld, J. Wendelstorf, T. Klein and G. Simon, *A self-consistent model for the cathode fall region of an electric arc*, J. Phys. D: Appl. Phys., **29** (1996) 121.

[34] M. S. Benilov and A. Marotta, *A model of the cathode region of atmospheric pressure arcs*, J. Phys. D: Appl. Phys., **28** (1995) 1869.

[35] X. Zhou and J. V. R. Heberlein, *Analysis of the arc-cathode interaction of free-burning arcs*, Plasma Sources Sci. Technol., **3** (1994) 564.

[36] H. Schmitz and K. U. Riemann, *Consistent analysis of the boundary layer of a Saha plasma*, J. Phys. D: Appl. Phys., **34** (2001) 1193.

[37] S. Coulombe, *A model of the electric arc attachment on non-refractory (cold) cathodes*, PhD Thesis, McGill University, Montréal, Canada (1997)

[38] F. Cayla, J. J. Gonzalez and P. Freton, *Arc-cathode interaction model*, Proceedings of the 28th International Conference on Phenomena in Ionized Gases, Prague, Czech Republic, **4P11-14** (2007) 1789.

[39] R. Gayet, C. Harel, T. Josso and H. Jouin, *A simple model for cathodic electronic emission enhanced by low-energy ions in high pressure arcs*, J. Phys. D: Appl. Phys., **29** (1996) 3063.

[40] W. Schottky, *Über den Austritt von Elektronen aus Glühdrähten bei verzögernden Potentialen* Annalen der Physik, **349** (1914) 1011.

[41] S. Coulombe and J. L. Meunier, *A comparison of the electron-emission equations used in arc-cathode interaction calculations*, J. Phys. D: Appl. Phys., **30** (1997) 2905.

[42] S. Coulombe and J. L. Meunier, *Thermo-field emission: a comparative study* J. Phys. D: Appl. Phys., **30** (1997) 776.

[43] R. H. Fowler and L. Nordheim, *Electron Emission in Intense Electric Fields*, Proceedings of the Royal Society of London, **A 119** (1928) 173.

[44] E. Hantzsche, *Mysteries of the Arc Cathode Spot: A Retrospective Glance*, IEEE Transactions on Plasma Science, **31** (2003) 799.

[45] T. H. Lee, *T-F theory of electron emission in high-current arcs*, J. Appl. Phys., **30** (1959) 166.

[46] E. L. Murphy and R. H. Good, *Thermionic, field emission and the transition region*, Physical Review, **102** (1956) 1464.

[47] E. Hantzsche, *Cathode Spots: Theories of Cathode Spots*, in *Handbook of Vacuum Arc Science and Technology: Fundamentals and Applications*, (Eds: R.L. Boxman, D.M. Sanders, P.J. Martin), Noyes Publications, New Jersey (1995), 151.

[48] J. Paulini, T. Klein and G. Simon, *Thermo-field emission and the Nottingham effect*, J. Phys. D: Appl. Phys., **26** (1993) 1310.

[49] A. E. Guile, *Arc-electrode phenomena*, Proceedings of the Institution of Electrical Engineers **118** (1971) 1131.

[50] M. S. Benilov, *Non-Linear heat structures and modes of current transfer to hot arc cathodes*, IEEE International Conference on Plasma Science, (1998) 273.

[51] M. S. Benilov, *Nonlinear surface heating of a plane sample and modes of current transfer to hot arc cathodes*, Physical Review E - Statistical Physics, Plasmas, Fluids, and Related Interdisciplinary Topics, **58** (1998) 6480.

[52] V. Nemchinsky, *Current density at the refractory cathode of a high-current high-pressure arc (two modes of cathode attachment)*, J. Phys. D: Appl. Phys., **36** (2003) 3007.

[53] S. S. Mackeown, *The cathode drop in an electric arc* Physical Review, **34** (1929) 611.

[54] P. D. Prewett and J. E. Allen, *The double sheath associated with a hot cathode*, Proceedings of the Royal Society of London, **A 348** (1976) 435.

[55] E. Hantzsche, *A new model of crater formation by arc spots*, Beiträge aus der Plasmaphysik, **17** (1977) 65.

[56] I. Beilis, *Analysis of the cathode spot in a vacuum arc*, Sov. Phys. tech. Phys., **19** (1974) 251.

[57] I. Beilis, *Cathode Spots: Theoretical Modeling of Cathode Spot Phenomena*, in *Handbook of Vacuum Arc Science and Technology: Fundamentals and Applications*, (Eds: R.L. Boxman, D.M. Sanders, P.J. Martin), Noyes Publications, New Jersey (1995), 208.

[58] I. Beilis, *Structure and dynamics of high-current arc cathode spots in vacuum*, J. Phys. D: Appl. Phys., **30** (1997) 119.

[59] B. Jüttner, *On the plasma density of metal vapour arcs*, J. Phys. D: Appl. Phys., **18** (1985) 2221.

[60] S. Coulombe and J. L. Meunier, *Importance of High Local Spot Pressure on the Attachment of Thermal Arcs on Cold Cathodes*, IEEE Transactions on Plasma Science, **25** (1997) 913.

[61] R. Deborah, C. Porto and C. W. Kimblin, *Experimental observations of cathode-spot surface phenomena in the transition from a vacuum metal-vapor arc to a nitrogen arc*, J. Appl. Phys., **53** (1982) 4740.

[62] C. W. Kimblin, *Cathode spot erosion and ionization phenomena in the transition from vacuum to atmospheric pressure arcs* J. Appl. Phys., **45** (1974) 5235.

[63] P. R. Emtage, *Interaction of the cathode spot with low pressures of ambient gas*, J. Appl. Phys., **46** (1975) 3809.

[64] B. Jüttner, *The dynamics of arc cathode spots in vacuum*, J. Phys. D: Appl. Phys., **28** (1995) 516.

[65] G. A. Mesyats, *Cathode Phenomena in a Vacuum Discharge: the Breakdown, the Spark and the Arc*, Nauka, Moscow, Russia (2000).

[66] G. A. Mesyats and D. I. Proskurovsky, *Pulsed Electrical Discharge in Vacuum*, ch. 5 and 8, Springer-Verlag, Berlin, Germany (1980).

[67] J. Mitterauer, *The surface dependence of different emission modes on mercury arc film cathodes*, J. Phys. D: Appl. Phys., **6** (1973) L91.

[68] J. Prock, *Solidification of hot craters on the cathode of vacuum arcs*, J. Phys. D: Appl. Phys., **19** (1986) 1917.

[69] J. Prock, *Time-Dependent Description of Cathode Crater Formation in Vacuum Arcs*, IEEE Transactions on Plasma Science, **PS-14** (1986) 482.

[70] B. Jüttner, *Formation time and heating mechanism of arc cathode craters in vacuum*, J. Phys. D: Appl. Phys., **14** (1981) 1265.

[71] S. Anders, A. Anders and B. Jüttner, *Brightness distribution and current density of vacuum arc cathode spots*, J. Phys. D: Appl. Phys., **25** (1992) 1591.

[72] A. Anders, S. Anders, B. Jüttner, W. Botticher, H. Luck and G. Schroder, *Pulsed dye laser diagostics of vacuum arc cathode spots*, IEEE Transactions on Plasma Science, **20** (1992) 466.

[73] E. Hantzsche, B. Jüttner and G. Ziegenhagen, *Why Vacuum Arc Cathode Spots Can Appear Larger Than They Are*, IEEE Transactions on Plasma Science, **23** (1995) 55.

[74] X. Zhou, B. Ding and J. V. R. Heberlein, *Temperature measurement and metallurgical study of cathodes in DC arcs*, IEEE Trans. Comp. Packag. Manufact. Technol. A, **19** (1996) 320.

[75] J. E. Daalder, *Cathode Erosion of Metal Vapor Arcs in Vacuum*, PhD Thesis, Tech. Univ., Eindhoven (1978).

[76] J. E. Daalder, *Diameter and current density of single and multiple cathode discharges in vacuum*, IEEE Trans Power Appar Syst, **PAS-93** (1974) 1747.

[77] B. Jüttner, *Erosion craters and arc cathode spots in vacuum*, Beiträge aus der Plasmaphysik, **19** (1979) 25.

[78] V. F. Puchkarev and A. M. Murzakayev, *Current density and the cathode spot lifetime in a vacuum arc at threshold currents*, J. Phys. D: Appl. Phys., **23** (1990) 26.

[79] V. F. Puchkarev, *Cathode Spots: Chapter Summary*, in *Handbook of Vacuum Arc Science and Technology: Fundamentals and Applications*, (Eds: Boxman R.L., D.M. Sanders, Martin P.J.), Noyes Publications, Park Ridge, New Jersey, USA (1995).

[80] B. Jüttner and V. F. Puchkarev, *Cathode Spots: Phenomenology*, in *Handbook of Vacuum Arc Science and Technology: Fundamentals and Applications*, (Eds: R.L. Boxman, D.M. Sanders, P.J. Martin), Noyes Publications, New Jersey (1995), 73.

[81] R. N. Szente, M. G. Drouet and R. Munz, *Current distribution of an electric arc at the surface of plasma torch electrodes*, J. Appl. Phys., **69** (1991) 1263.

[82] B. Saggau, *Kalorimetrie der drei Entladungsformen des elektrischen Zündfunkens*, Archiv für Elektrotechnik, **64** (1981) 9.

[83] R. E. Teets and J. A. Sell, *Calorimetry of Ignition Sparks*, SAE Paper, **880204** (1988).

[84] W. Herden, Bosch Entwicklungsbericht, (1994).

[85] T. Klein, J. Paulini and G. Simon, *Time-resolved description of cathode spot development in vacuum arcs*, J. Phys. D: Appl. Phys., **27** (1994) 1914.

[86] J. Rossignol, S. Clain and M. Abbaoui, *The modelling of the cathode sheath of an electrical arc in vacuum*, J. Phys. D: Appl. Phys., **36** (2003) 1495.

[87] J. E. Daalder, *A cathode spot model and its energy balance for metal vapour arcs*, J. Phys. D: Appl. Phys., **11** (1978) 1667.

[88] J. Mitterauer and P. Till, *Computer simulation of the dynamics of plasma surface interactions in vacuum arc cathode spots*, IEEE Transactions on Plasma Science, **PS-15** (1986) 488.

[89] P. Testé, *Contribution à l'étude de l'érosion des électrodes de torche à plasma - incidence de la structure métallurgique*, PhD Thesis, Université Paris 6, Paris, France (1994).

[90] L. W. Swanson, L. C. Crouser and F. M. Charbonnier, *Energy exchanges attending field electron emission*, Physical Review, **151** (1966) 327.

[91] K. S. Suraj and S. Mukherjee, *Power balance at cathode in glow discharge*, Physics of Plasmas, **12** (2005) 1.

[92] A. Marciniak, *Non-uniform heating effects during treatment in a glow discharge*, Thin Solid Films, **156** (1988) 337.

[93] R. S. Mason and R. M. Allott, *The theory of cathodic bombardment in a glow discharge by fast neutrals*, J. Phys. D: Appl. Phys., **27** (1994) 2372.

[94] E. W. Gray and J. R. Pharney, *Electrode erosion by particle ejection in low-current arcs*, J. Appl. Phys., **45** (1974) 667.

[95] B. J. Wang and N. Saka, *Spark erosion behavior of silver-based particulate composites*, Wear, **195** (1996) 133.

[96] F. Soldera, F. Mücklich, K. Hrastnik and T. Kaiser, *Description of the Discharge Process in Spark Plugs and its Correlation with the Electrode Erosion Patterns*, IEEE Transaction on Vehicular Technology, **53** (2004) 1257.

[97] S. Shalev, S. Goldsmith and R. L. Boxman, *In Situ Determination of Macroparticle Velocities in a Copper Vacuum Arc*, IEEE Transactions on Plasma Science, **PS-11** (1983) 146.

[98] S. Shalev, R. L. Boxman and S. Goldsmith, *Velocities and emission rates of cathode-produced molybdenum macroparticles in a vacuum arc*, J. Appl. Phys., **58** (1985) 2503.

[99] A. Lasagni, F. Soldera and F. Mücklich, *Quantitative investigation of material erosion caused by high pressure discharges in air and nitrogen*, Zeitschrift für Metallkunde, **95** (2004) 102.

[100] J. Rager, A. Flaig, G. Schneider, T. Kaiser, F. Soldera and F. Mücklich, *Oxidation Damage of Spark Plug Electrodes*, Advanced Engineering Materials, **7** (2005) 633.

[101] M. S. Benilov, S. Jacobsson, A. Kaddani and S. Zahrai, *Vaporization of a solid surface in an ambient gas*, J. Phys. D: Appl. Phys., **34** (2001) 1993.

[102] S. Coulombe and J. L. Meunier, *Theoretical prediction of non-thermionic arc cathode erosion rate including both vaporization and melting of the surface*, Plasma Sources Sci. Technol., **9** (2000) 239.

[103] R. N. Szente, R. Munz and M. G. Drouet, *Electrode erosion in plasma torches*, Plasma Chem. Plasma Process., **12** (1992) 327.

[104] F. Llewellyn-Jones, *Electrode Erosion by Spark Discharges*, British Journal of Applied Physics, **1** (1950) 60.

[105] R. S. Mason and M. Pichilingi, *Sputtering in a glow discharge ion source - pressure dependence: Theory and experiment*, J. Phys. D: Appl. Phys., **27** (1994) 2363.

[106] P. Sigmund, *Therory of Sputtering. I. Sputtering Yield of Amorphous and Polycristalline Targets*, Physical Review, **184** (1969) 383.

[107] H. Osamura and N. Abe, *Development of New Iridium Alloy for Spark Plug Electrodes*, SAE Paper, **1999-01-0796** (1999).

[108] T. Hori, M. Shibata, S. Okabe and K. Hashizume, *Super Ignition Spark Plug with Fine Center & Ground Electrodes*, SAE Paper, **2003-01-0404** (2003).

[109] K. Nishio, T. Oshima and H. Ogura, *A study on spark plug electrode shape*, Int. J. of Vehicle Design, **15** (1994) 119.

[110] J. A. Augis, F. J. Gibson and E. W. Gray, *Plasma and electrode interactions in short gap discharges in air: II. Electrode effects*, Int. J. Electronics, **30** (1971) 315.

[111] A. E. Guile and A. H. Hitchcock, *Oxide films on arc cathodes and their emission and erosion*, J. Phys. D: Appl. Phys., **8** (1975) 663.

[112] A. E. Guile, A. H. Hitchcock, K. Dimoff and A. K. Vijh, *Physical implications of an effective activation energy for an arc erosion on oxidised cathodes*, J. Phys. D: Appl. Phys., **15** (1982) 2341.

[113] A. H. Hitchcock and A. E. Guile, *A scanning electron microscope study of the role of copper oxide layers on arc cathode erosion rates*, Journal of Materials Science, **12** (1977) 1095.

[114] K. Dimoff, P. Antoine and A. K. Vijh, *Effects of enhanced heating by surface oxides on arc cathodes*, IEE Proceedings, **132** (1985) 301.

[115] F. A. Soldera and F. Mücklich, *On the Erosion of Material Surfaces caused by Electrical Plasma Discharging*, Mater. Res. Soc. Symp. Proc., **843** (2005) T5.4.1.

[116] F. A. Soldera, *Untersuchungen des Materialeinflusses auf Erosionsvorgänge durch elektrische Entladungen*, PhD Thesis, Saarland University, Saarbrücken, Germany (2005)

[117] W. A. Goering, *Spark Plug Electrode Materials and Erosion Mechanisms*, Ford Motor Company - Technical Report, **AR 68-15** (1968).

[118] G. C. Fryburg, *Enhanced Oxidation of Platinum in Activated Oxygen*, J. Chem. Phys., **24** (1956) 175.

[119] P. de Groot, *What is Frequency Domain Analysis?*, Zygo R&D Technical Bulletin, **9/23/93** (1993).

[120] *Zygo Coorporation Technical Report, http://www.zygo.com*.

[121] F. Soldera, M. Sierra Rota, N. Ilic and F. Mücklich, *Quantification of Localised Loss of Material*, Practical Metallography, **37** (2000) 477.

[122] L. A. Giannuzzi and F. A. Stevie, *Introduction to Focused Ion Beams - Instrumentation, Theory, Techniques and Practice*, L. A. Giannuzzi, F. A. Stevie, Springer, New York (2005).

[123] J. Orloff, M. Utlaut and L. W. Swanson, *High Resolution Focused Ion Beams: FIB and Its Applications*, Kluver Academic/Plenum Publishers, New York (2003).

[124] G. V. Samsonov, *The Oxide Handbook*, IFI/Plenum, New York (1973).

[125] N. N. Greenwood and A. Earnshaw, *Chemistry of the Elements, 2nd ed.*, Butterworth, London (1997).

[126] G. I. N. Waterhouse, G. A. Bowmaker and J. B. Metson, *Interaction of a ploycrystalline silver powder with ozone*, Surface and Interface Analysis, **33** (2002) 401.

[127] J. M. Knight, R. K. Wells and J. P. S. Badyal, *Plasma Oxidation of Copper-Silver Alloy Surfaces*, Chem. Mater., **4** (1992) 640.

[128] K. P. Jayadevan, N. V. Kumar, R. M. Mallya and K. T. Jacob, *Use of metastable, dissociated and charged gas species in synthesis: a low pressure analogue of the high pressure technique*, Journal of Materials Science, **35** (2000) 2429.

[129] G. Dearnaley, *A theory of the oxide-coated cathode*, Thin Solid Films, **3** (1969) 161.

[130] D. V. Morgan, M. J. Howes, R. D. Pollard and D. G. P. Waters, *Electroforming and dielectric breakdown in thin aluminium oxide films*, Thin Solid Films, **15** (1973) 123.

[131] J. F. Weaver and G. B. Hoflund, *Surface Characterization Study of the Thermal Decomposition of Ag_2O*, Chem. Mater., **6** (1994) 1693.

[132] A. E. Guile and A. H. Hitchcock, *Time variation in copper cathode erosion rate for long-duration arcs*, J. Phys. D: Appl. Phys., **8** (1975) 427.

[133] A. v. Engel and M. Steenbeck, *Elektrische Gasentladungen. Ihre Physik und Technik, Vol. II*, Springer, Berlin (1934).

[134] S. C. Brown, *Basic Data of Plasma Physics*, MIT Press, Cambridge MA (1959).

[135] J. E. Daalder, *Erosion structures on cathodes arced in vacuum*, J. Phys. D: Appl. Phys., **12** (1979) 1769.

[136] E. Hantzsche, B. Jüttner, V. F. Puchkarev, W. Rohrbeck and H. Wolff, *Erosion of metal cathodes by arcs and breakdowns in vacuum*, J. Phys. D: Appl. Phys., **9** (1976) 1771.

[137] B. J. Wang, N. Saka and E. Rabinowicz, *Static-gap, single spark erosion of Ag-CdO and pure metal electrodes*, Wear, **157** (1992) 31.

[138] S. Y. Chang, C. J. Hsu, C. H. Hsu and S. J. Lin, *Investigation on the arc erosion behavior of new silver matrix composites: Part I. Reinforced by particles*, Journal of Materials Research, **18** (2003) 804.

[139] C. J. Hsu, S. Y. Chang, L. Y. Chou and S. J. Lin, *Investigation on the arc erosion behavior of new silver matrix composites: part II. Reinforced by short fibers*, Journal of Materials Research, **18** (2003) 817.

[140] J. E. Greene and J. L. Guerrero-Alvarez, *Electro-Erosion of Metal Surfaces*, Metallurgical Transactions, **5** (1974) 695.

[141] N. Jeanvoine and F. Mücklich, *Electrode Erosion Behaviour of Silver-Nickel Multiphase Materials*, WDS'04 Proceedings of Contributed Papers, Part III, ISBN 80-86732-32-0, (2004) 486.

[142] N. Jeanvoine, *Untersuchung des Funkenerosionsverhaltens in Komposit-Kontaktwerkstoffen auf Silberbasis*, Diplomarbeit Universität des Saarlandes, (2004).

[143] J. Rager, A. Nagel, M. Schwenger, A. Flaig, G. Schneider and F. Mücklich, *Platinum Ceramic Composites as new Electrode Materials: Fabrication, Sintering, Microstructures and Properties*, Advanced Engineering Materials, **8** (2006) 81.

[144] F. Soldera, N. Ilic and F. Mücklich, *TEM-Investigations of Erosion Craters Caused by Electrical Discharge*, Practical Metallography, **42** (2005) 546.

[145] D. E. Newbury, D. C. Joy, P. Echlin, C. E. Fiori and J. I. Goldstein, *Electron Channeling Contrast in the SEM*, in *Advanced Scanning Electron Microscopy and X-Ray Microanalysis*, Springer, (1986).

[146] B. J. Inkson, T. Steer, G. Moebus and T. Wagber, *Subsurface nanoindentation deformation of Cu-Al multilayers mapped in 3D by focused ion beam microscopy*, Journal of Microscopy, **201** (2000) 256.

[147] T. Y. Tsui, J. Vlassak and W. D. Nix, *Indentation plastic displacement field: Part I. The case of soft films on hard substrates*, Journal of Materials Research, **14** (1999) 2196.

[148] M. Hansen and K. Anderko, *Consititution of Binary Alloys*, McGraw-Hill Book Company (1958).

[149] M. Bückins, R. Harscheidt, M. Keil and W. P. Rehbach, *REM-EDX Analysen mit hoher Ortauflösung unter der Verwendung von FIB-Schnitten*, Practical Metallography, **36** (2004) 417.

[150] W. D. Callister, *Fundamentals of Materials Science and Engineering*, John Wiley & Sons, New York (2001).

[151] F. Soldera, A. Lasagni, F. Mücklich, T. Kaiser and K. Hrastnik, *Determination of the cathode erosion and temperature for the phases of high voltage discharges using FEM simulations*, Computational Materials Science, **32** (2005) 123.

[152] H. Bergsaker, L. Ilynsky and G. Portnoff, *Ion beam analysis of sputter-deposited gold films for quartz resonators*, Surface and Interface Analysis, **30** (2000) 620.

[153] C. Holzapfel, F. Soldera, E. A. Faundez and F. Mücklich, *Site-specific structural investigations of oxidized nickel samples modified by plasma erosion processes*, Journal of Microscopy, **227** (2007) 42.

[154] J. Konrad, S. Zaefferer and D. Raabe, *Investigation of orientation gradients around a hard Laves particle in a warm-rolled Fe3Al-based alloy using a 3D EBSD-FIB technique*, Acta Materialia, **54** (2006) 13690.

[155] R. F. Mehl, *Solidification of metals and alloys*, AIME, New York (1951).

[156] D. Y. Li and J. A. Szpunar, *A possible role for surface packing density in the formation of {111} texture in solidified FCC metals*, Journal of Materials Science Letters, **13** (1994) 1521.

[157] R. Trivedi and W. Kurz, *Casting*, in *Metals Handbook 9th edition* ASM International, Metals Park, Ohio (1988).

[158] W. M. Steen, *Laser Material Processing, 2nd Edition*, Springer, London (1998).

[159] S. Kou and Y. H. Wang, *Computer Simulation of Convection in Moving Arc Weld Pools*, Metallurgical Transactions A, **17A** (1986) 2271.

[160] S. Kou and D. K. Sun, *Fluid Flow and Weld Penetration in Stationary Arc Welds*, Metallurgical Transactions A, **16A** (1985) 203.

[161] S. Kou, *Welding Metallurgy*, John Wiley & Sons (2003).

[162] G. M. Oreper, T. W. Eagar and J. Szekely, *Convection in Arc Weld Pools*, Welding Journal, **62** (1983) 307.

[163] C. R. Heiple and P. Burgardt, *Effects of SO_2 Shielding Gas Additions on GTA Weld Shape*, Welding Journal, **64** (1985) 159.

[164] F. Wang, W. K. Hou, S. J. Hu, E. Kannatey-Asibu, W. W. Schultz and P. C. Wang, *Modelling and analysis of metal transfer in gas metal arc welding*, J. Phys. D: Appl. Phys., **36** (2003) 1143.

[165] I. Egry, *The Surface Tension of Binary Alloys: Simple Models for Complex Phenomena*, International Journal of Thermophysics, **26** (2005) 931.

[166] K. C. Mills and Y. C. Su, *Review of surface tension data for metallic elements and alloys: Part 1 - Pure metals*, International Materials Reviews, **51** (2006) 329.

[167] B. J. Wang and N. Saka, *Thermal Analysis of Electrode Heating and Melting Due to a Spark*, IEEE Transactions on Components, Hybrids and Manufacturing Technology, **16** (1993) 456.

[168] H. C. Carslaw and J. C. Jaeger, *Conduction of Heat in Solids*, Oxford University Press, New York (1959).

[169] D. Bäuerle, *Laser Processing and Chemistry*, Springer, Berlin (1996).

[170] M. Storti, *Numerical modeling of ablation phenomena as two-phase Stefan problems*, International Journal of Heat and Mass Transfer, **38** (1995) 2843.

[171] L. W. Hunter and J. R. Kuttler, *Enthalpy method for heat conduction problems with moving boundaries*, Journal of Heat Transfer, **111** (1989) 239.

[172] J. Rossignol, M. Abbaoui and S. Clain, *Numerical modelling of thermal ablation phenomena due to a cathodic spot*, J. Phys. D: Appl. Phys., **33** (2000) 2079.

[173] M. Abbaoui, A. Lefort, S. Clain and J. Rossignol, *A comparative study of the behaviour of silver, copper and nickel submitted to a constant high power flux density* Eur. Phys. J. Appl. Phys., **31** (2005) 45.

[174] Z. J. He and R. Haug, *Cathode spot initiation in different external conditions*, J. Phys. D: Appl. Phys., **30** (1997) 603.

[175] M. Messaad, A. W. Belarbi, M. Abbaoui and A. Lefort, *Numerical Model on the Interaction of a Vacuum Arc with a Copper Cathode*, ISIJ International, **46** (2006) 1618.

[176] *Smithells Metals Reference Book, 7th Edition*, E.A. Brandes, G.B. Brook, Butterworth-Heinemann (1997).

[177] R. S. Freund, R. C. Wetzel, R. J. Shul and T. R. Hayes, *Cross-section measurements for electron-impact ionization of atoms*, Physical Review A, **41** (1990) 3575.

[178] E. J. Gonzalez, J. E. Bonevich, G. R. Stafford, G. White and D. Josell, *Thermal transport through thin films: Mirage technique measurements on aluminum/titanium multilayers*, J. Mater. Res., **15** (2000) 764.

[179] D. Josell, A. Cezairliyan and J. E. Bonevich, *Thermal Diffusion Through Multilayer Coatings: Theory and Experiment*, International Journal of Thermophysics, **19** (1998) 525.

[180] B. M. Clemens, G. L. Eesley and C. A. Paddock, *Time-resolved thermal transport in compositionally modulated metal films*, Physical Review B, **37** (1988) 1085.

[181] F. Bordeaux and A. R. Yavari, *Utra rapid heating by spontaneous mixing reactions in metal-metal multilayer composites*, J. Mater. Res., **5** (1990) 1656.

[182] A. R. Miedema, P. F. de Châtel and F. R. de Boer, *Cohesion in alloys - fundamentals of a semi-empirical model*, Physica B+C, **100** (1980) 1.

[183] F. Lantelme and A. Salmi, *Activity Measurements in Nickel-Platinum Alloys*, J. Phys. Chem., **100** (1996) 1159.

[184] A. Anders, S. Anders, B. Jüttner, H. Pursch, W. Bötticher, H. Lück and G. Schröder, *Vacuum arc cathode spot parameters from high-resolution luminosity measurements*, J. Appl. Phys., **71** (1992) 4763.

[185] B. Jüttner, *Cathode spots of electric arcs*, J. Phys. D: Appl. Phys., **34** (2001) R103.

[186] H. Salihou, M. Abbaoui, A. Lefort and R. Auby, *Determination of the power lost by conduction into the cathode at low current arc*, J. Phys. D: Appl. Phys., **28** (1995) 1883.

[187] P. Testé, T. Leblanc, J. Rossignol and R. Andlauer, *Contribution to the assessment of the power balance at the electrodes of an electric arc in air*, Plasma Sources Sci. Technol., **17** (2008) 1.

[188] P. Testé and J. Rossignol, *A first attempt to connect a microscopic vision of the cathode fragment and micro spot to a macroscopic approach of the cathode arc root: A multi-scale problem*, High Temperature Material Processes, **12** (2008) 39.

[189] L. Yedra Cardona, *Arc erosion behaviour of platinum based and silver based composites*, Diploma Thesis, Saarland University, Saarbrücken, Germany (2009).

[190] W. Li and D. Y. Li, *Effects of dislocation on electron work function of metal surface*, Materials Science and Technology, **18** (2002) 1057.

[191] *CRC Handbook of Chemistry and Physics* David R. Lide, 74th Edition, CRC Press Inc, Bota Raton, Florida (1994).

[192] K. C. Mills, B. J. Monaghan and B. J. Keene, *Thermal conductivities of molten metals: Part 1 Pure metals*, International Materials Reviews, **41** (1996) 209.

A. Refractory and Non-Refractory Cathodes

The distinction between refractory and non-refractory cathodes can be made by calculating the ratio of the flux of vaporized atoms Γ_n (Langmuir equation (2.12)) to the flux of thermionically emitted electrons J_T/e (Richardson-Dushman equation (2.8)) [37]. The lower the ratio $e\Gamma_n/J_T$ is, the higher is the ability of the cathode to operate in the thermionic range. Figure A shows this ratio as a function of the cathode surface temperature for Cu (typical non-refractory), W (typical refractory) and Pt. According to this figure, Pt can be classified as a non-refractory material. Hence, Pt cathodes are expected to operate in the thermo-field range and the electron emission must be evaluated by the Murphy and Good equation (2.10).

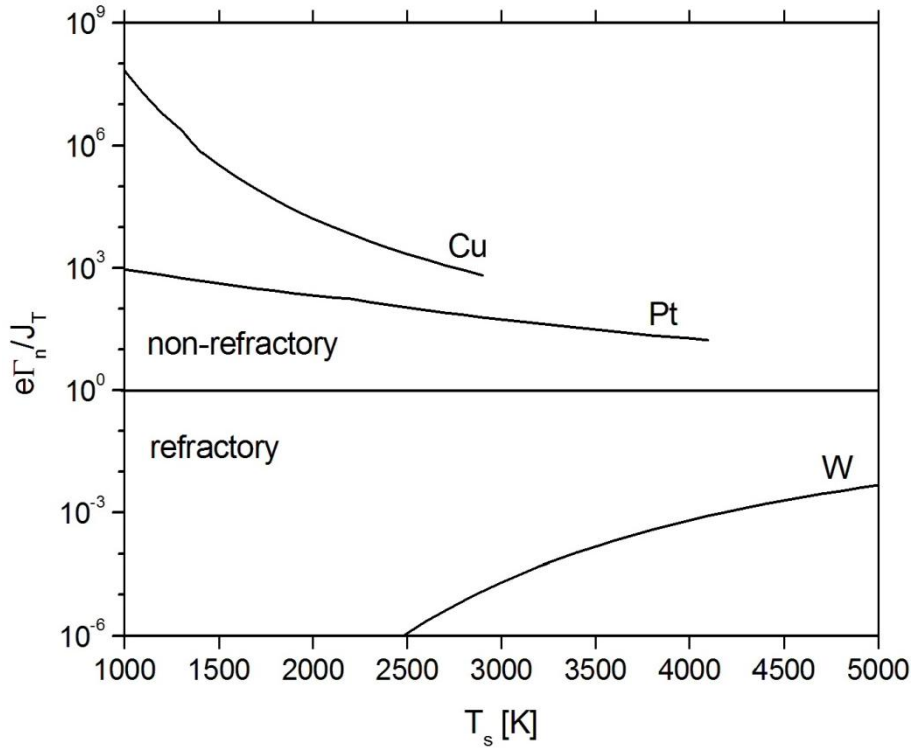

Figure A Ratio of the flux of vaporized atoms Γ_n to the flux of thermionically emitted electrons J_T/e as a function of the surface temperature for Cu, Pt and W, representing the ability of a cathode material to operate in the thermionic range.

B. Fitting of the Electron Emission Current Density

Figure B shows the constants A_0, B_1, B_2, and B_3 of the polynomial functions used to fit the logarithm of the electron emission current density J_e calculated with the help of the Murphy and Good equation (2.10). These constants were determined for integer values of the surface electric field strengths E_s ranging between 1×10^9 and 10×10^9 V/m (square symbols). For non-integer values of E_s, the constants were determined via linear interpolation (straight lines).

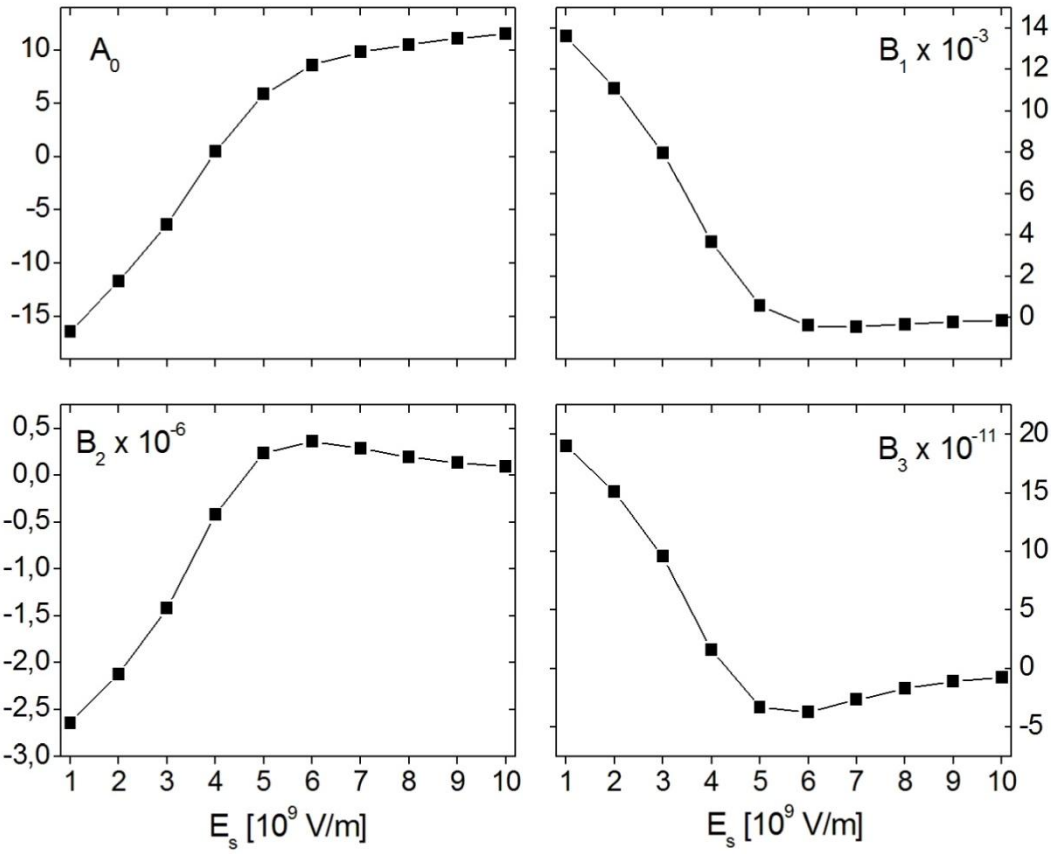

Figure B Constants A_0, B_1, B_2, and B_3 as a function of the surface electric field E_s. For non-integer values of E_s, the constants are determined via linear interpolation.

C. Influence of the Simulated Region Size

Figure C shows the temperature T_{max} at the position (0,0) as a function of the length of the simulated region L in an electrode subjected to an ion power density P_i=4×10^{10} W/m^2 during the time t_0=10 µs. For L<30 µm, the temperature T_{max} is strongly affected by the size of the region. This is due to the boundary condition T=300 K which is close to the region of interest and "forces" the temperature to remain low. For L>50 µm, the boundary condition no longer affects the temperature which converges to a constant value. T_{max} is shown here as an example, and all the results derived from the temperature distribution (melting depth, electron emission current, vaporization rate, etc) show the same behavior. For the simulation, we take L=100 µm. Another possibility will consist in assuming adiabatic boundaries. In this case, however, one can expect that overly small regions will lead to overestimated temperatures by preventing heat dissipation.

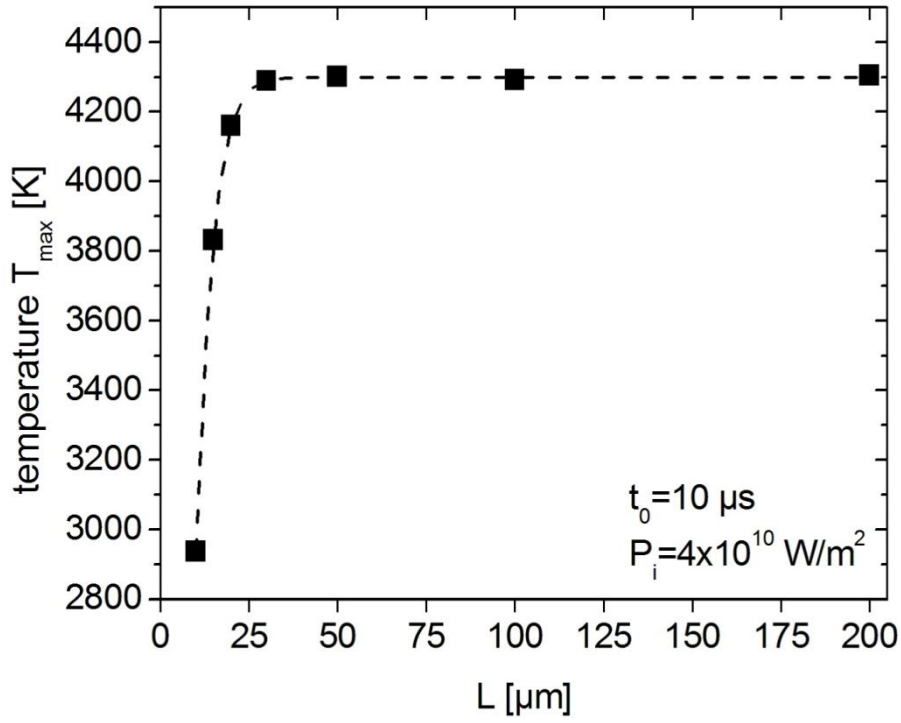

Figure C Temperature T_{max} at position (0,0) as a function of the length of the simulated region L for an ion power density P_i=4×10^{10} W/m^2 and a pulse duration t_0=10 µs.

D. Determination of U_i and E_s

The mean ion energy U_i and the surface electric field strength E_s are coupled via the Mackeown equation (6.12) and equation (6.11). Therefore, both equations have to be solved simultaneously. In Figure D, the functions E_s=f(U_i) and U_i=g(E_s) are plotted on the same diagram for P_i=10^{10} W/m^2. The single solution corresponds to the intersection of these two curves. An iterative process is used to find the solution. An arbitrary value of U_i is chosen, for example 29 eV, and the corresponding value of E_s is calculated using the equation E_s=f(U_i). Using the equation U_i=g(E_s), the new value of U_i is determined. The process is repeated until the correct solution is obtained. Since the curves are almost perpendicular the results converge very rapidly. Only three iteration steps are required to obtain the solution with a precision of three digits.

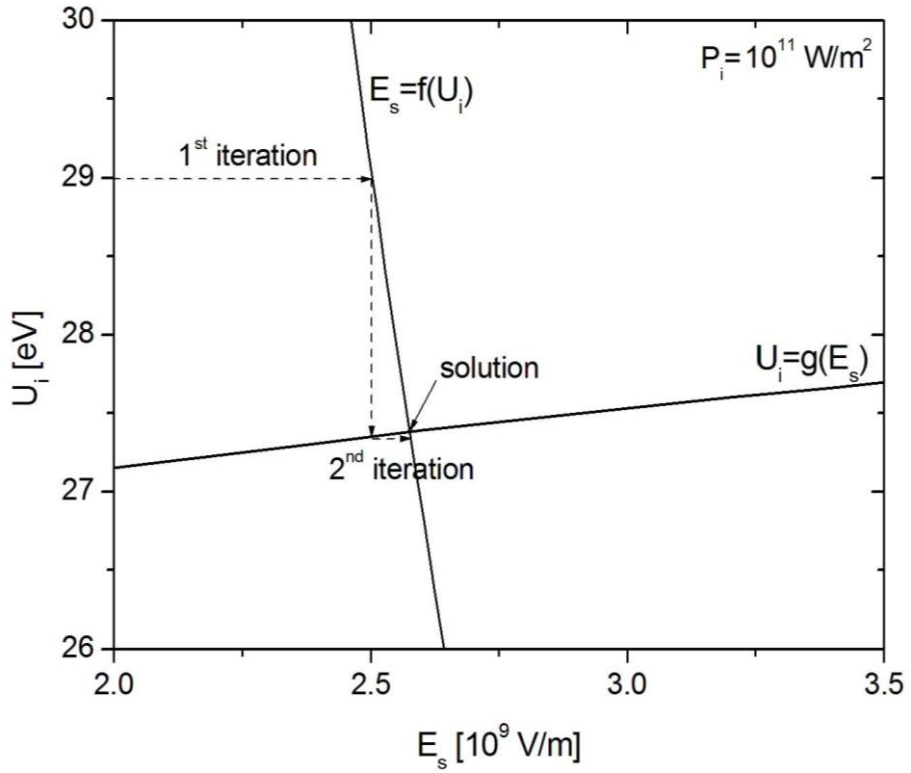

Figure D Determination of U_i and E_s. The functions E_s=f(U_i) (Mackeown equation (6.12)) and U_i=g(E_s) (equation (6.11)) are plotted together for P_i=10^{10} W/m^2. The solution, i.e., the intersection of both curves, is found using an iterative process.

E. Properties of Platinum Cathodes

Table E Physical and thermodynamical properties of Pt used in the simulation

Properties		Values	Ref
Melting temperature	T_m [K]	2041	[191]
Boiling temperature	T_b [K]	4098	[191]
Latent heat of melting	L_m [J/g]	113.65	[191]
Latent heat of vaporization	W_{ev} [J/g]	2405	[191]
Thermal conductivity (solid)	k_s [W/m.K]	$74.099 - 0.01519\times T + 2.58997\cdot10^{-5}\times T^2 - 5.9674\cdot10^{-9}\times T^3$	[191]
Thermal conductivity (liquid)	k_l [W/m.K]	53	[192]
Specific heat capacity (solid)	c_{ps} [J/g.K]	$0.02146\times(5.8 + 0.00128\times T)$	[191]
Specific heat capacity (liquid)	c_{pl} [J/g.K]	0.178	[176]
Density (solid)	ρ_s [g/m^3]	21.5×10^5	[191]
Density (liquid)	ρ_l [g/m^3]	$[19 - 0.0029\times(T-T_m)]\times10^6$	[191]
Vapor pressure (solid)	log p_{vs} [mmHg]	$-29200/T + 13.24 - 0.855\times\log(T)$	[176]
Vapor pressure (liquid)	log p_{vl} [mmHg]	$-28500/T + 14.30 - 1.26\times\log(T)$	[176]
Atomic mass	m_n [kg]	3.23938×10^{-25}	[191]
Cathode drop voltage	U_c [V]	16	[80]
Work function	ϕ [eV]	5.65	[191]
First ionization potential	E_i [eV]	9	[191]

The temperature T is given in K